Precision Calculations and their Application to LHC Data

Zur Erlangung des akademischen Grades eines

DOKTORS DER NATURWISSENSCHAFTEN
(Dr. rer. nat.)

von der KIT-Fakultät für Physik des
Karlsruher Instituts für Technologie (KIT)
genehmigte

DISSERTATION

von

M.Sc. Lucas Kunz

aus Rastatt

Tag der mündlichen Prüfung: 19. Juli 2024

Referentin: Prof. Dr. Gudrun Heinrich
Korreferent: Priv.-Doz. Dr. Klaus Rabbertz

Karlsruher Institut für Technologie
Fakultät für Physik
Wolfgang-Gaede-Str. 1
76131 Karlsruhe

Ich versichere wahrheitsgemäß, diese Arbeit selbstständig verfasst, alle benutzten Hilfsmittel vollständig und genau angegeben und alles kenntlich gemacht zu haben, was aus Arbeiten anderer unverändert oder mit Abänderungen entnommen wurde, sowie die Satzung des KIT zur Sicherung guter wissenschaftlicher Praxis in der jeweils gültigen Fassung beachtet zu haben.

Karlsruhe, 12.06.2024

. . . .
(Lucas Kunz)

Abstract

The Large Hadron Collider (LHC) at CERN near Geneva is the largest and most energetic particle accelerator existing. It collides protons, which are composite objects made of quarks and gluons, bound together by the strong force. Their interactions are governed by quantum chromodynamics (QCD). The relation between the incoming proton as a bound state and its single constituents is empirically described by parton distribution functions (PDFs), which therefore appear in every calculation of theoretical predictions for LHC processes. The extraction of these PDFs from measured data involves computing time expensive iterative procedures. Hence, to produce results in reasonable time, a very efficient and flexible setup is needed. The `APPLfast` project fulfills these requirements by using grid interpolation, thereby allowing for an a posteriori choice of a set of PDFs or value of the strong coupling. This thesis explains the general logic of the project and uses the code for calculations of dijet production at next-to-next-to-leading order in QCD, including the full color structure. Based on these calculations the value of the strong coupling is determined from experimental data taken at the LHC, yielding $\alpha_s(m_Z) = 0.1176 \pm 0.0014$.

Other than that, the LHC is the place where the Higgs boson was discovered in 2012. Since then, the properties of this particle are studied with great eagerness, trying to test whether it behaves like predicted by the Standard Model (SM) of particle physics. Deviations from the SM can be described with Effective Field Theory (EFT), which is used in this thesis to examine possible non-SM effects in Higgs plus one jet production. Calculations at next-to-leading order in QCD including the full top mass dependence are made both within and beyond the SM, in the framework of non-linear EFT, showing that sizable and possibly measurable deviations from the SM can arise for high values of the Higgs boson transverse momentum.

Zusammenfassung

Der Large Hadron Collider (LHC) am CERN in der Nähe von Genf ist der größte und energiereichste existierende Teilchenbeschleuniger. Er kollidiert Protonen miteinander, welche aus Quarks und Gluonen bestehen und durch die starke Kraft gebunden werden. Ihre Wechselwirkungen werden durch die Quantenchromodynamik (QCD) bestimmt. Die Beziehung zwischen dem einlaufenden Proton als gebundenem Zustand und seinen einzelnen Bestandteilen wird empirisch durch Partonverteilungsfunktionen (PDFs) beschrieben, die daher in jeder Berechnung theoretischer Vorhersagen für LHC-Prozesse auftauchen. Die Extraktion dieser PDFs aus gemessenen Daten erfordert rechenzeitintensive iterative Verfahren. Um Ergebnisse in angemessener Zeit zu erhalten, ist daher ein sehr effizienter und flexibler Algorithmus erforderlich. Das `APPLfast` Projekt erfüllt diese Anforderungen, indem es Interpolation einsetzt und damit eine a posteriori Wahl der PDFs und des Wertes der starken Kopplung ermöglicht. In dieser Arbeit wird die allgemeine Logik des Projekts erläutert und der Code für Berechnungen von Dijet-Produktion in übernächst-führender Ordnung in QCD verwendet, wobei die volle Farbstruktur inkludiert ist. Basierend auf diesen Berechnungen wird der Wert der starken Kopplung aus am LHC gemessenen Experimentaldaten bestimmt, es ergibt sich $\alpha_s(m_Z) = 0.1176 \pm 0.0014$.

Darüber hinaus ist der LHC der Ort, an dem 2012 das Higgs-Boson entdeckt wurde. Seitdem werden die Eigenschaften dieses Teilchens mit großem Eifer untersucht, um zu testen, ob es sich so verhält, wie es das Standardmodell (SM) der Teilchenphysik vorhersagt. Abweichungen vom SM können mit Hilfe von Effektiver Feldtheorie (EFT) beschrieben werden, die in dieser Arbeit verwendet wird, um mögliche Nicht-SM-Effekte bei der Produktion eines Higgs-Bosons in Verbindung mit einem Jet zu untersuchen. Im Rahmen der nichtlinearen EFT werden Berechnungen in nächst-führender Ordnung in QCD und unter Einbeziehung der kompletten Top-Massen-Abhängigkeit sowohl innerhalb des SM als auch darüber hinaus durchgeführt, welche zeigen, dass erhebliche und möglicherweise messbare Abweichungen vom SM für hohe Werte des Transversalimpulses des Higgs-Bosons auftreten können.

Contents

1. Introduction

Around 1900, Lord Kelvin famously said: "There is nothing new to be discovered in physics now. All that remains is more and more precise measurement." The last century has proven this statement immensely wrong, since it came with many great discoveries and allowed us to construct and extensively test both Quantum Mechanics and Quantum Field Theory. Both of these concepts have greatly enriched mankind's capability to understand and describe nature. Many scientist's ingenuity allowed for technological advances that always made better experiments possible, led to the formulation of more complete theories and the development of more versatile and efficient tools. This journey, which began with the discovery of quantum effects more than a hundred years ago, is far from over today.

A major outcome of these past decades of discoveries is a general model describing the fundamental particles matter is made of and their interactions, called the Standard Model (SM) of particle physics. The SM answers many questions modern physics asks and has been intensively tested experimentally. Since the discovery of the Higgs boson in 2012, it is considered complete. However, many phenomena are not described within this model, which makes extensions of it or a completely new theory necessary. Since the SM is immensely successful in very precisely predicting the phenomena it can describe, one is inclined not to overthrow it altogether. Given that we know of the existence of observations beyond the reach of the SM, this has two consequences: First, it has to be determined where exactly this reach of the SM ends. Second, possible effects stemming from physics beyond the SM have to be parametrized and calculated, such that a targeted experimental search can be conducted. This thesis tries to tackle both of these ends.

This document is structured as follows: In chapter 2 we introduce the Standard Model, its particle content, the interactions described by it and how they arise from symmetry requirements with respect to quantum numbers called charge, isospin and color. As mentioned in the previous paragraph, this model is the basis of modern particle physics. In chapter 3 we outline the techniques used to calculate and predict observables for collider experiments and the subtleties that come with them, including perturbation theory, factorisation, renormalisation and confinement. In chapter 4 we motivate and explain the concept of Effective Field Theories (EFTs) and clarify the differences between the linear and non-linear types. Now that the introduction is done, we describe how observations at hadron colliders depend on parton distribution functions (PDFs) and the precise determination thereof and present a solution of how to mitigate the effect of this bottleneck in chapter 5. Here we also discuss the structure of the strong interaction and quantum chromodynamics (QCD) and present calculations for the production of two QCD final states (so-called jets) at the ATLAS and CMS experiments. Together with data from said experiments, we determine the value of the strong coupling at next-to-next-to-leading order in perturbation theory, taking into account all color configurations. In chapter 6 we go beyond the SM and study the production of a Higgs boson and jet within non-linear EFT at next-to-leading perturbative order, taking into account the top mass with its actual value instead of approximating it to be infinitely large (so-called heavy top limit). Finally, chapter 7 concludes the thesis and gives a perspective for future research to be done.

All throughout this work natural units are used, i.e. $\hbar = c = \epsilon_0 = \mu_0 = k_{\mathrm{B}} = 1$.
Unless explicitly stated otherwise, an index appearing twice is summed over.
All other notations shall be explained at the moment they are used for the first time.

2. The Standard Model of Particle Physics

The laws of physics are - at least to our current understanding - governed by four fundamental forces: Electromagnetism and gravitation are present in our everyday lives, such that a more precise introduction can be omitted at this point. The other two, the so-called strong and weak forces, control how nuclei are built and decay. On the distance and energy scales of particle physics, gravitation plays a very negligible role. Particle masses being very tiny compared to those of planets, stars and other astronomical objects, the effects of gravity are most often ignored when discussing particle interactions. For the other three forces there exists a very general and immensely successful model, the Standard Model (SM) of particle physics. It organizes matter constituents and interactions in the sense of a gauge theory [1–4].

2.1. Particle content of the Standard Model

The Standard Model is populated by matter particles (fermions, spin $\frac{1}{2}$) interacting via force carriers (gauge bosons, spin 1) and the Higgs field (also a boson, spin 0). A pictorial representation of this arrangement can be found in figure 2.1, explanations of its content follow in the subsequent sections.

2.1.1. Fermions

In total there are 12 fermions, half of which are quarks and the other half are leptons. Both of these types exist in three so-called generations, differing from each other only by their masses. In every generation, there is a positively ($+\frac{2}{3}$) and negatively ($-\frac{1}{3}$) charged quark (up/down, charm/strange, top/bottom), a negatively (-1) charged lepton (electron, muon, tau) and a chargeless neutrino. Other than the electromagnetic charges, all left-handed chiral versions of these particles carry weak isospin, and all quarks have yet another quantum number called color, which can have three different values.

2.1.2. The gauge group of the Standard Model

With respect to the aforementioned properties (charge, isospin and color) the fermions obey symmetries, which are described mathematically by Lie groups. Quarks form triplets under the group $SU(3)_\mathrm{C}$, including all three values of the color quantum number. They never show up alone, but always as bound states that add up to "white". Left-handed fermions of any kind (both quarks and leptons) form doublets under $SU(2)_\mathrm{L}$ and their weak isospin is conserved. Finally, all fermions have a weak hypercharge that is conserved under $U(1)_\mathrm{Y}$, such that the SM in total has the gauge group $SU(3)_\mathrm{C} \times SU(2)_\mathrm{L} \times U(1)_\mathrm{Y}$.

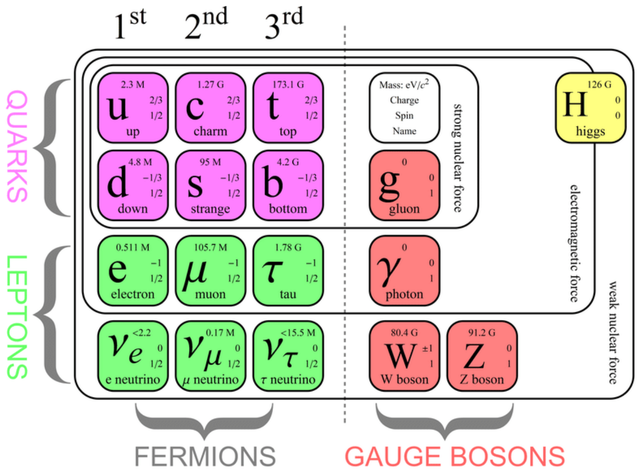

Figure 2.1.: Pictorial representation of the particle content of the Standard Model. Quarks are shown in purple, leptons in green, gauge bosons in red and the Higgs boson in yellow. [5]

The latter two symmetries are spontaneously broken to the electromagnetic $U(1)_\text{Q}$ when the Higgs field acquires a non-vanishing vacuum expectation value (VEV); further details on this will be discussed later in section 2.3. The relation between their group generators and quantum numbers is given by the Gell-Mann–Nishijima formula,

$$Q = T_3 + \frac{Y}{2}, \tag{2.1}$$

where T_3 is the z-component of the weak isospin, Y is the weak hypercharge and Q the electromagnetic charge. Sometimes a different normalisation for Y is used where the factor $\frac{1}{2}$ is absent. Throughout this thesis we will stick to the notation including this factor, such that the Standard Model Higgs field has $Y = 1$.

2.1.3. Bosons

In order to keep the symmetries intact at every spacetime point (local gauge theory), one has to introduce gauge bosons. These live in the adjoint representation of the group the belong to, meaning that there are eight for $SU(3)_\text{C}$, three for $SU(2)_\text{L}$ and one for $U(1)_\text{Y}$. The first eight remain unchanged and appear as the eight massless gluons. The latter four mix under the effect of electroweak symmetry breaking (see section 2.3) and result in the $W^\pm$, Z and photon γ, only the last of which remains massless.

In addition to the gauge bosons, all of which have spin 1 due to group theoretical properties, there is one more boson with spin 0. The Higgs boson, named after Peter Higgs who was one of the theorists postulating it [6–9], was originally introduced in order to solve unitarity problems in longitudinal vector boson (i.e. spin 1 boson) scattering. Via the mechanism of spontaneous symmetry breaking it is also responsible for the existence of particle masses.

2.2. Lagrange densities

The dynamics of particles is usually encoded in a Lagrange density (in the following mostly called "Lagrangian"), which in the case of the Standard Model can be written and decomposed as follows:

$$\begin{aligned}
\mathcal{L}_{\text{SM}} &= \mathcal{L}_{\text{Boson}} + \mathcal{L}_{\text{Fermion}} + \mathcal{L}_{\text{Higgs}} + \mathcal{L}_{\text{Yukawa}} + \mathcal{L}_{\text{Gauge}} && (2.2)\\
\mathcal{L}_{\text{Boson}} &= -\frac{1}{4}B_{\mu\nu}B^{\mu\nu} - \frac{1}{4}W^a_{\mu\nu}W^{a,\mu\nu} - \frac{1}{4}G^b_{\mu\nu}G^{b,\mu\nu} && (2.3)\\
\mathcal{L}_{\text{Fermion}} &= i\,\overline{\Psi}_i\,\gamma^\mu D_\mu \Psi_i && (2.4)\\
\mathcal{L}_{\text{Higgs}} &= \frac{1}{2}\left(\tilde{D}_\mu\Phi\right)^\dagger\left(\tilde{D}^\mu\Phi\right) - \frac{\mu^2}{2}\Phi^2 - \frac{\lambda}{4}\Phi^4 && (2.5)\\
\mathcal{L}_{\text{Yukawa}} &= -Y_{ij}\,\overline{\Psi}_{i,L}\,\Phi\,\Psi_{j,R} - \tilde{Y}_{ij}\,\overline{\Psi}_{i,L}\,\tilde{\Phi}\,\Psi_{j,R} + \text{h.c.}\,, && (2.6)
\end{aligned}$$

where

$$\begin{aligned}
D_\mu &= \partial_\mu - ig'YB_\mu - ig\tau^a W^a_\mu P_{\text{L}} - ig_s T^b G^b_\mu && (2.7)\\
\tilde{D}_\mu &= \partial_\mu - ig'B_\mu - ig\tau^a W^a_\mu && (2.8)
\end{aligned}$$

is the covariant derivative in its most general form. In this definition, P_{L} is the left-handed projector, $\tau^a = \frac{1}{2}\sigma^a$ are the generators of $SU(2)$ with σ^a being the Pauli matrices, $T^b = \frac{1}{2}\lambda^b$ are the generators of $SU(3)$ consisting of the Gell-Mann matrices λ^b and Y is the weak hypercharge, where we already plugged in $Y = 1$ for the Higgs field in (2.8).

The objects in (2.3) are the field strength tensors which can be calculated from commutators of covariant derivatives and read

$$\begin{aligned}
B_{\mu\nu} &= \partial_\mu B_\nu - \partial_\nu B_\mu && (2.9)\\
W^a_{\mu\nu} &= \partial_\mu W^a_\nu - \partial_\nu W^a_\mu + g\,\epsilon^{abc}\,W^b_\mu W^c_\nu && (2.10)\\
G^a_{\mu\nu} &= \partial_\mu G^a_\nu - \partial_\nu G^a_\mu + g_s\,f^{abc}\,G^b_\mu G^c_\nu\,. && (2.11)
\end{aligned}$$

B_μ, W^a_μ and G^a_μ are the gauge bosons of $U(1)_{\text{Y}}$, $SU(2)_{\text{L}}$ and $SU(3)_{\text{C}}$, respectively, and ϵ^{abc} and f^{abc} are the structure constants. $\overline{\Psi}_i$ and Ψ_j are (anti-)fermions of flavour i or j, Φ is the Higgs doublet and $\tilde{\Phi}$ is the charge conjugated Higgs doublet $\tilde{\Phi} = i\sigma^2\,\Phi^*$. Y_{ij} and $\tilde{Y}_{ij}$ are the Yukawa matrices, which will be explained in greater detail in section 2.4. The explicit form of the gauge fixing and ghost interaction terms in $\mathcal{L}_{\text{Gauge}}$ is not of major importance for the discussion in the following chapters of this thesis and will thus not be given.

2.3. Electroweak symmetry breaking

From (2.5) one can read off the Higgs potential:

$$V(\Phi) = \frac{\mu^2}{2}\Phi^2 + \frac{\lambda}{4}\Phi^4. \tag{2.12}$$

If $\mu^2 < 0$, the minimum of this potential is not reached for $||\Phi|| = 0$, but rather for $||\Phi|| = \frac{v}{\sqrt{2}} = \sqrt{\frac{-\mu^2}{\lambda}}$. This so-called vacuum expectation value (VEV) is $v \approx 246\,\mathrm{GeV}$. As this new ground state is not invariant under $SU(2)_\mathrm{L}$ transformations the symmetry is spontaneously broken. This breaking is responsible for the $W^\pm$ and Z bosons to acquire masses while on the other hand the electromagnetic symmetry $U(1)_\mathrm{Q}$ is unbroken and the corresponding gauge boson - the photon - remains massless. The boson mass generation can be described more rigorously by the Goldstone theorem [10–16]: For every generator of a group that is spontaneously broken, one massless boson arises. In the case at hand, the number of broken generators is three.

Before symmetry breaking, the Higgs field has four degrees of freedom as it is a complex doublet. It can be written as

$$\Phi = \begin{pmatrix} \frac{1}{\sqrt{2}}\left(G_1 + iG_2\right) \\ \frac{1}{\sqrt{2}}\left(v + h + iH\right) \end{pmatrix}. \tag{2.13}$$

By a suitable gauge transformation (unitary gauge) three of the components of this doublet can be set to zero:

$$\Phi_\mathrm{UnitaryGauge} = \begin{pmatrix} 0 \\ \frac{1}{\sqrt{2}}\left(v + h\right) \end{pmatrix}. \tag{2.14}$$

As the $SU(2)_\mathrm{L}$ symmetry is local, we can find such a suitable transformation at every spacetime point. After symmetry breaking this is not the case anymore and the three degrees of freedom that corresponded to the transformation of gauging away the Goldstone modes G_1, G_2 and H are absorbed into the gauge fields, which means they get massive. The exact value of these masses can easily be calculated by inserting (2.14) into (2.5):

$$m_W = \frac{v\,g}{2} \quad \text{and} \quad m_Z = \frac{v\,\sqrt{g^2 + g'^2}}{2}. \tag{2.15}$$

The formula for the Z mass already shows that the Z boson is a linear combination of a $SU(2)_\mathrm{L}$ and a $U(1)_\mathrm{Y}$ gauge boson. The relation between electroweak bosons before and after symmetry breaking is as follows:

$$W^\pm = \frac{1}{\sqrt{2}}\left(W_1 \mp iW_2\right) \quad \text{and} \quad \begin{pmatrix} A \\ Z \end{pmatrix} = \begin{pmatrix} \cos\theta_W & \sin\theta_W \\ -\sin\theta_W & \cos\theta_W \end{pmatrix} \begin{pmatrix} B \\ W_3 \end{pmatrix}. \tag{2.16}$$

The photon γ, denoted by the electromagnetic four-potential A, is a superposition of the same $SU(2)_\mathrm{L}$ and $U(1)_\mathrm{Y}$ gauge fields the Z consists of, but its coefficients are such that it remains massless after symmetry breaking, $m_\gamma = 0$.

2.4. Yukawa Lagrangian and quark mixing

The Yukawa Lagrangian was already introduced in (2.6), now we rewrite it using a different notation: L labels the doublet of left-handed leptons, Q is the doublet of left-handed quarks,

$$L := \begin{pmatrix} \nu_L \\ E_L \end{pmatrix} \quad \text{and} \quad Q := \begin{pmatrix} U_L \\ D_L \end{pmatrix}. \tag{2.17}$$

The symbols ν_L, E_L, U_L and D_L stand for left-handed neutrinos, charged leptons, up-type and down-type quarks, respectively. Analogously, right-handed up-type quarks will be called U_R, right-handed down type quarks are written as D_R. Right-handed charged leptons are labeled as E_R, whereas right-handed neutrinos are not present in the SM. With this labeling the Yukawa Lagrangian reads

$$\mathcal{L}_{\text{Yukawa}} = -Y^{(l)}_{ij}\overline{L}_i\,\Phi\,E_{R,j} - Y^{(d)}_{ij}\overline{Q}_i\,\Phi\,D_{R,j} - Y^{(u)}_{ij}\overline{Q}_i\,\tilde{\Phi}\,U_{R,j} + \text{h.c.}\ . \tag{2.18}$$

In the Higgs vacuum,

$$\langle\Phi\rangle = \begin{pmatrix} 0 \\ \frac{v}{\sqrt{2}} \end{pmatrix} \quad \text{and} \quad \langle\tilde{\Phi}\rangle = i\sigma^2\,\langle\Phi^*\rangle = \begin{pmatrix} \frac{v}{\sqrt{2}} \\ 0 \end{pmatrix}\ , \tag{2.19}$$

(2.18) simplifies to

$$\mathcal{L}_{\text{Yukawa}} = -\frac{v}{\sqrt{2}}\left(Y^{(l)}_{ij}\,\overline{E}_{L,i}\,E_{R,j} + Y^{(d)}_{ij}\,\overline{D}_{L,i}\,D_{R,j} + Y^{(u)}_{ij}\,\overline{U}_{L,i}\,U_{R,j}\right) + \text{h.c.}\ . \tag{2.20}$$

When the Yukawa coupling matrices Y_{ij} are diagonalised we find that (2.20) generates fermion mass terms. Let $\hat{Y}_{ij}$ denote the diagonal Yukawa matrices being related to the non-diagonal ones via

$$Y^{(\alpha)} = \Omega^{(\alpha)\,\dagger}\,\hat{Y}^{(\alpha)}\,K^{(\alpha)}, \tag{2.21}$$

wherein $\Omega^{(\alpha)}$ and $K^{(\alpha)}$ are unitary matrices and $\alpha \in \{l, d, u\}$. Absorbing these matrices into redefinitions of the fermionic fields,

$$E_L \longrightarrow E'_L = \Omega^{(l)}\,E_L\ \ ,\ \ D_L \longrightarrow D'_L = \Omega^{(d)}\,D_L\ \ ,\ \ U_L \longrightarrow U'_L = \Omega^{(u)}\,U_L\ \ , \tag{2.22}$$

$$E_R \longrightarrow E'_R = K^{(l)}\,E_R\ \ ,\ \ D_R \longrightarrow D'_R = K^{(d)}\,D_R\ \ ,\ \ U_R \longrightarrow U'_R = K^{(u)}\,U_R\ \ , \tag{2.23}$$

yields the mass Lagrangian for charged leptons and quarks:

$$\mathcal{L}_{\text{Yukawa}} = -\frac{v}{\sqrt{2}}\left(\hat{Y}^{(l)}_{ij}\,\overline{E'}_{L,i}\,E'_{R,j} + \hat{Y}^{(d)}_{ij}\,\overline{D'}_{L,i}\,D'_{R,j} + \hat{Y}^{(u)}_{ij}\,\overline{U'}_{L,i}\,U'_{R,j}\right) + \text{h.c.}\ . \tag{2.24}$$

This redefinition of fields has consequences for interaction terms with $W^\pm$ bosons. The corresponding Lagrangian can be extracted from (2.4) by applying the rules of spontaneous symmetry breaking (2.16):

$$\mathcal{L}_W = -\frac{g}{\sqrt{2}}\,W^+_\mu\,\overline{U}_{L,i}\,\gamma^\mu\,D_{L,i} - \frac{g}{\sqrt{2}}\,W^-_\mu\,\overline{D}_{L,i}\,\gamma^\mu\,U_{L,i}\ . \tag{2.25}$$

When the same redefinition of fermions (2.22) and (2.23) is inserted into this interaction Lagrangian it yields

$$\begin{aligned} \mathcal{L}'_W &= -\frac{g}{\sqrt{2}}\,W^+_\mu\,\overline{U'}_{L,i}\,\gamma^\mu\,D'_{L,j}\,\left(\Omega^{(u)}\,\Omega^{(d)\,\dagger}\right)_{ij} - \frac{g}{\sqrt{2}}\,W^-_\mu\,\overline{D'}_{L,i}\,\gamma^\mu\,U'_{L,j}\,\left(\Omega^{(d)}\,\Omega^{(u)\,\dagger}\right)_{ij} \\ &= -\frac{g}{\sqrt{2}}\,W^+_\mu\,\overline{U'}_{L,i}\,\gamma^\mu\,D'_{L,j}\,(V_{\text{CKM}})_{ij} - \frac{g}{\sqrt{2}}\,W^-_\mu\,\overline{D'}_{L,i}\,\gamma^\mu\,U'_{L,j}\,\left(V^\dagger_{\text{CKM}}\right)_{ij} \end{aligned} \tag{2.26}$$

with the Cabibbo-Kobayashi-Maskawa matrix $V_{\text{CKM}} := \Omega^{(u)}\,\Omega^{(d)\,\dagger}$.

An important property of this matrix is that the off-diagonal elements, which induce mixing among quarks of different generations, are very tiny and such interactions therefore strongly suppressed. Moreover, the fact that it has a non-vanishing complex phase is responsible for the existence of CP-violation in the weak sector of the SM.

3. Perturbation Theory and Higher Orders

The Standard Model described in the previous chapter is of course not only a theoretical concept, but has been validated extensively by all sorts of experiments. Among those, colliders are most frequently used. In order to investigate the properties of fundamental particles and interactions and compare them to the predictions of the SM, observables have to be defined, calculated theoretically and measured experimentally. The tool most often used for such calculations is perturbation theory, i.e. expanding the amplitude of a process in powers of the coupling constant or, equivalently, the number of interaction vertices. This approach, however, is not applicable to the whole chain of reactions happening at a hadron collider like the LHC, because perturbativity breaks down in scenarios with a large coupling, as is the case for the binding energy of the proton.

3.1. Factorisation theorem

In order to calculate any observable quantity - like total or differential scattering cross sections or decay widths - for the LHC, one has to circumvent the fact that the binding of the proton cannot be understood analytically. The interactions of its constituents, i.e. quarks and gluons, on the other hand can be treated in such a way by the means of a perturbative expansion. Therefore, one separates the perturbative so-called hard scattering of those fundamental particles inside the proton from the binding itself, using

$$\sigma_{pp\to X} = \sum_{a,b} \int_0^1 \mathrm{d}x_a \int_0^1 \mathrm{d}x_b \; f_a(x_a, \mu_F)\, f_b(x_b, \mu_F) \cdot \sigma_{ab\to X}(x_a, x_b, \mu_R, \mu_F) \;. \tag{3.1}$$

This formula is known as the factorisation theorem and connects the cross section of two protons producing an arbitrary final state X, $\sigma_{pp\to X}$, with the cross section of two partons a and b resulting in the same final state, $\sigma_{ab\to X}$. In order to get the full result, i.e. the left side of (3.1), one has to sum over all possible types of partons, i.e. gluons and all six types of quarks, and integrate over their momentum with reasonable weighting functions. x_a and x_b refer to the momentum fraction carried by the relevant parton, meaning that its momentum is $p_a = x_a\, P$ with P being the momentum of the proton it comes from, and equivalently $p_b = x_b\, P$. The factorisation scale μ_F can be understood as the energy at which the proton breaks apart into its constituent partons, whereas the renormalisation scale μ_R is an artifact coming from higher order effects to be discussed in section 3.3.

$f_a(x_a, \mu_F)$ and $f_b(x_b, \mu_F)$ are the parton distribution functions (PDFs) which give the probabilities that at an energy scale μ_F a parton of type a (or b) is found with a momentum fraction x_a (or x_b) of the proton. Unlike the hard scattering cross section $\sigma_{ab\to X}$, the PDFs cannot be calculated from first principles, but must be fitted from comparison to experimental data. They are universal, i.e. independent of the process, and their evolution with respect to the scale μ_F can be computed perturbatively following the Dokshitzer-Gribov-Lipatov-Altarelli-Parisi (DGLAP) equations [17–19].

3.2. Perturbative expansion

Observables like cross sections and decay widths are calculated from (squared) transition amplitudes, the latter of which can be depicted in a diagrammatic way. In this section we will use this intuitive pictorial approach to explain the mathematical foundations beneath it. For the sake of simplicity we discuss a (non-realistic) toy model with the following Lagrangian:

$$\mathcal{L} = \mathcal{L}_0 + \mathcal{L}_{\text{int}} \quad \text{with} \quad \mathcal{L}_0 = \frac{1}{2}(\partial_\mu \phi)(\partial^\mu \phi) - \frac{m^2}{2}\phi^2 \quad \text{and} \quad \mathcal{L}_{\text{int}} = -\frac{\lambda\,\mu_\lambda}{3!}\phi^3 \,. \tag{3.2}$$

The two terms in $\mathcal{L}_0$ give the field ϕ a propagator and mass, whereas $\mathcal{L}_{\text{int}}$ introduces interactions of 3 particles of the same type, i.e. a vertex. In order to calculate the probability amplitude for a certain scattering process to happen, we have to calculate the matrix element of a time-ordered exponential of this interaction Lagrangian between the initial and final state:

$$S_{if} = \langle f|\, T \exp\left(i \int \mathrm{d}^4x\, \mathcal{L}_{\text{int}}(x)\right) |i\rangle \,. \tag{3.3}$$

Since the exponential can be expanded in a Taylor series as $\exp(t) = 1 + t + \frac{t^2}{2} + \mathcal{O}\left(t^3\right)$ this can be rewritten into

$$\begin{aligned} S_{if} &= \langle f|i\rangle + \mathcal{M}_{if} \quad \text{with} \\ \mathcal{M}_{if} &= \langle f|\, T\left(i \int \mathrm{d}^4x\, \mathcal{L}_{\text{int}}(x)\right) |i\rangle \qquad (3.4) \\ &\quad -\frac{1}{2}\langle f|\, T\left(\int \mathrm{d}^4x \int \mathrm{d}^4y\, \mathcal{L}_{\text{int}}(x)\, \mathcal{L}_{\text{int}}(y)\right) |i\rangle + \mathcal{O}\left(\lambda^3\right) \,. \qquad (3.5) \end{aligned}$$

In order for a two-by-two scattering process to happen we need at least two vertices, i.e. two insertions of $\mathcal{L}_{\text{int}}$. For such a process (3.4) does not give a contribution, the resulting matrix element is simply zero, whereas (3.5) leads to diagrams like the one in figure 3.1. This is, however, not the only contribution: Any even power of $\mathcal{L}_{\text{int}}$ will lead to non-vanishing results, some of which for order 4 are shown in figure 3.2.

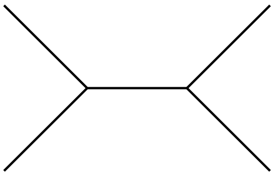

Figure 3.1.: Example diagram for a two-by-two particle scattering process at tree level.

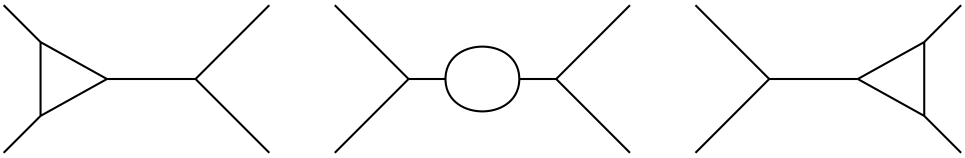

Figure 3.2.: Example diagrams for two-by-two particle scattering processes at one-loop level. The loop can either show up as a correction to a vertex (1 and 3) or to the internal propagator (2). Self energy corrections (i.e. loops in the external legs) are omitted for simplicity and not relevant for the argument at hand.

It is obvious that this expansion does, in general, never end, but has to be truncated in order to calculate a finite result. Taylor's theorem guarantees that the remainder neglected with such a truncation after the n-th term is only of the order λ^{n+1}, which is sufficiently small for any for $\lambda \ll 1$. For the process at hand we can write

$$\mathcal{M}_{2\to 2} = \lambda^2 \mathcal{M}^{(\mathrm{LO})} + \lambda^4 \mathcal{M}^{(\mathrm{NLO})} + \mathcal{O}\left(\lambda^6\right) , \tag{3.6}$$

where $\mathcal{M}^{(\mathrm{LO})}$ includes all diagrams without loops, also called tree level, and $\mathcal{M}^{(\mathrm{NLO})}$ includes all one-loop graphs. The abbreviations stand for leading order (LO) and next-to-leading order (NLO) and can analogously be expanded to any higher order, e.g. NNLO as next-to-next-to-leading order, N3LO as next-to-next-to-next-to-leading order and so forth. Since observables like the cross section σ depend on the absolute square of this probability amplitude,

$$\sigma \sim \int \mathrm{d}\Phi \, |\mathcal{M}|^2 \ , \mathrm{d}\Phi \text{ being the final state phase space,} \tag{3.7}$$

it is convenient to define $\alpha_\lambda := \frac{\lambda^2}{4\pi}$ and write

$$\sigma = \alpha_\lambda \left(\sigma^{(\mathrm{LO})} + \alpha_\lambda \sigma^{(\mathrm{NLO})} + \alpha_\lambda^2 \sigma^{(\mathrm{NNLO})} + \mathcal{O}\left(\alpha_\lambda^3\right) \right) . \tag{3.8}$$

(3.8) is a very general formula, not only applicable to this toy model used for illustration, but also to actual SM processes. For the strong interaction, also known as quantum chromodynamics (QCD), only the naming is different: the coupling is not called λ but g_s and the expansion of observables is done with respect to $\alpha_s := \frac{g_s^2}{4\pi}$.

3.3. Renormalisation

Only in very few cases the LO theoretical prediction is precise enough to keep up with experimental accuracy; for many processes of QCD, NLO and NNLO calculations are needed. As shown in figure 3.2, the Feynman diagrams associated with such calculations contain loops, the internal momenta of which are fixed by neither boundary conditions nor momentum conservation constraints. To account for all possibilities one has to integrate over the whole phase space. A simple bubble as shown in figure 3.3 leads to an integral of the following sort:

$$B_0 = \int \frac{\mathrm{d}^4 k}{(2\pi)^4} \frac{1}{\left[k^2 - m^2 + i\epsilon\right] \left[(k+p)^2 - m^2 + i\epsilon\right]} . \tag{3.9}$$

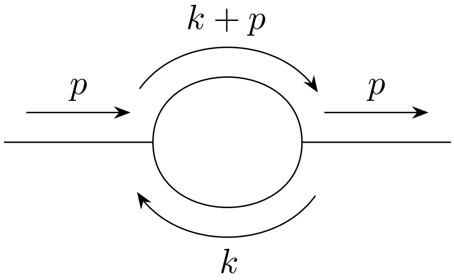

Figure 3.3.: The bubble integral diagram with external momentum p and loop momentum k. For simplicity all propagators are scalar and of the same mass m.

The problem with this integral is that it does not converge at the upper limit $|k| \longrightarrow \infty$. This phenomenon is known as ultraviolet (UV) divergence, since large momenta correspond to short wavelengths. Counting the powers of $|k|$ yields

$$B_0 \sim \int^{\infty} \frac{\mathrm{d}|k|\,|k|^3}{|k|^4} = \int^{\infty} \frac{\mathrm{d}|k|}{|k|} \sim \log(\infty) \ , \tag{3.10}$$

a so-called logarithmic divergence. The standard approach to circumvent this problem is dimensional regularisation (DR) [20], which means to perform the integral not in 4 spacetime dimensions, but in $D = 4 - 2\varepsilon$ ones, then take the limit $\varepsilon \longrightarrow 0$ later. There exist multiple other possible schemes, but only DR leaves both the Lorentz and gauge invariance of the integrals intact, thus allowing to still make use of Ward identities. Before taking the limit, the structure of the integral is

$$B_0 = \int \frac{\mathrm{d}^D k}{(2\pi)^D} \frac{1}{[k^2 - m^2 + i\epsilon]\,[(k+p)^2 - m^2 + i\epsilon]} = \frac{1}{\varepsilon} B_{\text{divergent}} + B_{\text{finite}} + \mathcal{O}(\varepsilon) \ . \tag{3.11}$$

It is important to keep in mind that the two epsilons appearing in (3.11) are strictly different objects: ϵ assures the causality of the propagators, whereas ε is the dimensional regulator. The result of the above integral has been calculated in [21], but is not important for the discussion at this point. Even without knowing the precise form it is obvious that in order to get a finite result one has to get rid of the first term, which is divergent in the limit $\varepsilon \longrightarrow 0$. This can be achieved by the introduction of counter terms, as outlined in the following subsection 3.3.1.

Shifting the dimensionality of the integral or, in general, the physical phase space brings some subtleties into the calculation. In natural units the action is per definition dimensionless. From this follows that in D spacetime dimensions any Lagrangian has to have mass dimension D. Normally, bosonic fields (both scalar and vectorial ones) as well as derivatives have dimension one, $[\phi, A^\mu, \partial^\mu] = 1$, fermionic fields have dimension $\frac{3}{2}$, $[\Psi] = \frac{3}{2}$, and couplings of any sort (Yukawa, gauge, scalar potential) are dimensionless, $[Y, g, \lambda] = 0$. Needless to say, masses have mass dimension one, $[m] = 1$, thus the name. If now $D = 4 - 2\varepsilon \neq 4$, all of this shifts according to table 3.1. Most importantly, couplings are not dimensionless any more. One can, however, still define a dimensionless quantity $\tilde{\lambda}$ using $\lambda = \mu_R^{\varepsilon}\,\tilde{\lambda}$, where μ_R is the renormalisation scale.

Object	4 dimensions	D dimensions
scalar field ϕ	1	$1-\varepsilon$
vector field A^μ	1	$1-\varepsilon$
derivative ∂^μ	1	1
spinor field Ψ	$\frac{3}{2}$	$\frac{3}{2}-\varepsilon$
coupling Y, g, λ	0	ε
mass m	1	1

Table 3.1.: Mass dimensions of different objects compared in 4 and in $D = 4 - 2\varepsilon$ spacetime dimensions. The λ here is the trilinear coupling in the interaction term of (3.2), not the quartic coupling in (2.5). The latter one is also dimensionless in $D = 4$, but has dimension 2ε in $D = 4 - 2\varepsilon$.

3.3.1. Counterterms

For the sake of clarity and simplicity we go back to a toy model similar to the one defined in (3.2):

$$\mathcal{L} = \frac{1}{2}(\partial_\mu\phi)(\partial^\mu\phi) - \frac{m^2}{2}\phi^2 - \frac{\lambda}{4!}\phi^4 \ . \tag{3.12}$$

This time, however, we include a quartic coupling instead of a trilinear one in the interaction term, similar to (2.5), since it is the more realistic scenario. In this case, as written below table 3.1, the coupling has mass dimension 2ε in $D = 4 - 2\varepsilon$.

The following calculation relies on the simple basic assumption that divergent quantities can be expressed as a product of a divergent prefactor and a finite renormalised version of said quantity. Following the discussion in [1] we define

$$m_0^2 = Z_m\, m^2 = (1+\delta_m)\, m^2 \quad , \quad \lambda_0 = Z_\lambda\, \mu_R^{2\varepsilon}\, \lambda = (1+\delta_\lambda)\, \mu_R^{2\varepsilon}\, \lambda \ \text{ and } \ \phi_0 = \sqrt{Z_\phi}\, \phi \quad . \tag{3.13}$$

Everything with index 0 is called a bare quantity; the bare Lagrangian then looks like

$$\mathcal{L}_0 = \frac{1}{2}(\partial_\mu\phi_0)(\partial^\mu\phi_0) - \frac{m_0^2}{2}\phi_0^2 - \frac{\lambda_0}{4!}\phi_0^4 \tag{3.14}$$

$$= \frac{1}{2}Z_\phi(\partial_\mu\phi)(\partial^\mu\phi) - Z_\phi(1+\delta_m)\,\frac{m^2}{2}\phi^2 - Z_\phi^2(1+\delta_\lambda)\,\mu_R^{2\varepsilon}\,\frac{\lambda}{4!}\phi^4 \quad . \tag{3.15}$$

Ultraviolet divergent terms, e.g. the $\frac{1}{\varepsilon}$ pole of integrals like (3.11), can be absorbed into the constants δ_X with $X = m, \lambda$ or Z_ϕ, such that the masses, couplings and fields themselves remain finite. There are multiple ways of defining this absorbtion, i.e. different renormalisation schemes, the most common of which are minimal subtraction (MS), modified minimal subtraction ($\overline{\text{MS}}$) and the on-shell scheme (OS). The exact form of δ_m and δ_λ at one-loop level in the first two of these schemes can be found in [1].

3.3.2. Infrared divergences

Non-convergent integrals for large loop momenta are not the only source of divergences. Not only the upper edge, $|k| \longrightarrow \infty$, can lead to problems, but also the lower edge, $|k| \longrightarrow 0$,

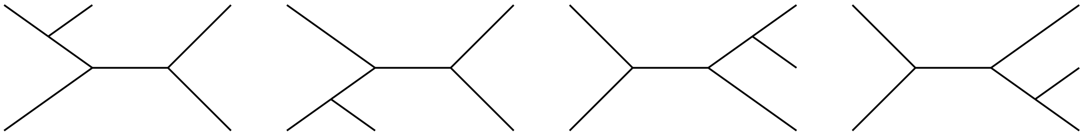

Figure 3.4.: Example diagrams for two-by-two particle scattering processes with additional radiation from either initial (1 and 2) or final state legs (3 and 4).

can do so. Other than these purely mathematical subtleties, also experimental aspects influence the result. It might happen that an additional particle is radiated off one of the external legs of the process observed, but is not resolved because it is either collinear to the other particle it came from (collinear divergence) or has very close to zero energy (soft divergence). In a two-by-two scattering process, there are four legs from which such radiation can arise, as shown in figure 3.4. The origin of the divergence can be easily explained. If a particle with momentum p radiates off another particle with momentum k, the Feynman diagram contains one more internal propagator:

$$\text{propagator} \sim \frac{1}{p^2 - m^2} = \frac{1}{(p' + k)^2 - m^2} \overset{\text{massless}}{=} \frac{1}{2\,p' \cdot k} = \frac{1}{2\,E_{p'} E_k (1 - \cos\theta)} \quad , \tag{3.16}$$

which is clearly divergent in the limit $\theta \to 0$ (collinear) or $E_k \to 0$ (soft). Fortunately, the KLN theorem [22, 23] helps to clean up most of these divergent parts. It states that soft and collinear poles from unresolved additional radiation (so-called real contribution) cancel with infrared poles from loop integrals (so-called virtual component). However, a few singularities from radiation collinear to one of the initial state partons of the process (so-called initial state radiation, ISR) remain even after summing up the real and virtual parts; these can be removed by absorbing them into the definition of the PDFs.

3.4. Running couplings

As mentioned in section 3.3, coupling constants are not dimensionless any more when using dimensional renormalisation. A redefinition like in (3.13) allows to still end up with a dimensionless quantity, but comes with the price of a dependence on the renormalisation scale μ_R [24, 25]. The evolution of the coupling with respect to this scale is described by the renormalisation group equation

$$\mu_R \frac{\mathrm{d}\alpha_s}{\mathrm{d}\mu_R} = \beta(\alpha_s) \tag{3.17}$$

with the β-function on the right hand side. At one-loop level the QCD β-function reads

$$\beta(\alpha_s) = -\beta_0 \frac{\alpha_s^2}{2\pi} + O\,(\text{higher orders}) \quad \text{with } \beta_0 = 11 - \frac{2}{3} n_f \tag{3.18}$$

and n_f being the number of active colored quark flavors. Plugging (3.18) into (3.17) yields the solution

$$\alpha_s(\mu_R) = \frac{\alpha_s(Q)}{1 + \frac{\alpha_s(Q)}{2\pi}\,\beta_0\,\log\left(\frac{\mu_R}{Q}\right)} \quad . \tag{3.19}$$

Knowing the value of α_s at one scale, e.g. $\alpha_s(m_Z)$, thus allows to calculate its value at any other energy via a simple formula. At high energies this relation can be approximated as

$$\alpha_s(\mu_R) = \frac{4\pi}{\beta_0 \log\left(\frac{\mu_R^2}{\Lambda_{\mathrm{QCD}}^2}\right)} \tag{3.20}$$

with $\Lambda_{\mathrm{QCD}} \approx 210\,\mathrm{MeV}$ for $n_f = 5$ (valid at energies above the bottom mass, but below the top mass) in the $\overline{\mathrm{MS}}$ renormalisation scheme [26, 27]. The dependence on μ_R is not physical, but merely a remnant of the perturbative series being truncated. The more higher order corrections are included in the calculation, the less it gets. Since one can, however, never include all orders and has to truncate somewhere, a suitable scale has to be chosen for every process. For decay processes, for example, a natural choice is to set the scale equal to the mass of the decaying particle.

3.4.1. Confinement and bound states

The running of the coupling constant has severe consequences for the physical processes mediated by the strong force. Since (3.20) shows α_s to be rapidly decreasing for large μ, the interactions between quarks and gluons become very weak at high energies. This feature is called *asymptotic freedom* and allows for highly precise perturbative calculations at high energies, i.e. short distances. On the other end of the spectrum, at low energies, i.e. long distances, the force becomes very strong, thus enabling bound states to form. Here, quarks and gluons can never be observed as free particles, but always group up such that the resulting bound state is color neutral. This effect is known as *color confinement* and is a common feature of non-abelian gauge theories.

When mesons (bound states of a quark and an antiquark) or baryons (bound states of three quarks) are tore apart, it is energetically disfavored for the quarks to stay unbound. Instead, particle-antiparticle pairs are created from the vacuum until there are only colorless bound states again. Experimentally this can be observed when quarks or gluons are produced: The final state will not consist of them individually, but results in a stream of color neutral hadronic particles, a so-called jet.

4. Effective Field Theory

Effective Field Theory (EFT) is a tool to describe phenomena at low energies in a way agnostic of the details of their origin. It allows for the mathematical description of interactions which might stem from heavier particles. A classical example for an EFT within the SM is Fermi Theory, which can be used in the calculation of the muon's decay width. There is only one channel this decay can happen through, $\mu^- \longrightarrow e^- \nu_\mu \overline{\nu}_e$, the Feynman graph of which is depicted in the left half of figure 4.1. Given that the energy scale of the process - basically the muon mass - is far below the mass of the W boson mediating the decay one can integrate out the latter, resulting in an effective four-fermion-vertex as can be seen in the right half of the same figure 4.1. In terms of the amplitude this means neglecting the momentum q flowing through the W propagator,

$$\overline{\Psi}_{\nu_\mu} \left(\tfrac{ig}{\sqrt{2}} \gamma_\mu \tfrac{1-\gamma_5}{2} \right) \Psi_\mu \left(\tfrac{-ig^{\mu\nu}}{q^2 - m_W^2} \right) \overline{\Psi}_e \left(\tfrac{ig}{\sqrt{2}} \gamma_\nu \tfrac{1-\gamma_5}{2} \right) \Psi_{\overline{\nu}_e} \tag{4.1}$$

$$\overset{q^2 \ll m_W^2}{\Longrightarrow} \quad -i \, \tfrac{G_\mathrm{F}}{\sqrt{2}} \, \overline{\Psi}_{\nu_\mu} \, \gamma^\mu (1 - \gamma_5) \, \Psi_\mu \, \overline{\Psi}_e \, \gamma_\mu (1 - \gamma_5) \, \Psi_{\overline{\nu}_e} \; , \tag{4.2}$$

with the Fermi constant $\frac{G_\mathrm{F}}{\sqrt{2}} = \frac{g^2}{8\, m_W^2}$. Counting the mass dimensions (in four spacetime dimensions) in (4.2) shows a typical feature of an EFT: The operator itself (i.e. the interacting fields, spinor and Lorentz structure) has dimension six, the prefactor dimension minus two. It is usual that EFT operators have mass dimension larger than four, which is why the coefficient needs negative mass dimension to end up with a total of four in the end, leading to the desired dimensionless action. From this structure it follows that the effects of the operator are suppressed by the scale in the denominator of the prefactor, in the case at hand the W mass. Far below that scale it is save to do calculations within the EFT. However, once the energy of a process approaches or even surpasses this scale, the approximations made by the effective theory - i.e. integrating out internal particles - become inaccurate and the underlying full theory has to be used.

In cases where physics beyond the Standard Model is studied, the full theory is not known. The impact of effective operators being added to the SM Lagrangian is then often interpreted as remnants of heavy particles yet to be discovered. According to the structure and rules such operators must comply with, a distinction can be made between two different types of EFTs: The linear one, which orders operators with respect to canonical mass dimension, will be described in section 4.1; the non-linear one, using the more abstract concept of *chiral dimensions* for accounting, is introduced in section 4.2. The work presented in chapter 6 of this thesis happens in the realm of non-linear EFT and heavily relies on the logic thereof.

4.1. Standard Model Effective Field Theory

The Standard Model has two types of symmetries: On the one hand it is invariant under Lorentz (or rather Poincaré) transformations of the spacetime coordinates; on the other hand, it contains the gauge group $SU(3)_\mathrm{C} \times SU(2)_\mathrm{L} \times U(1)_\mathrm{Y}$. It is precisely the union of all operators with mass dimension four that respect these symmetries and are constructed only from SM fields as described in section 2.1. If one relaxes the requirement to reach dimension four in the sense previously described, i.e. allowing dimensions larger than four combined with prefactors of negative dimension, many more possible operators can be constructed. Standard Model Effective Field Theory (SMEFT) [28, 29] takes these new operators and orders them with respect to their mass dimension, hence there are operators of dimension five, six, seven, eight and so on with coefficients of dimension minus one, minus two, minus three, minus four and so forth. In a very generic way one can write

$$\mathcal{L} = \mathcal{L}_\mathrm{SM} + \sum_i \frac{c_i^{(5)}}{\Lambda} O_i^{(5)} + \sum_i \frac{c_i^{(6)}}{\Lambda^2} O_i^{(6)} + \sum_i \frac{c_i^{(7)}}{\Lambda^3} O_i^{(7)} + \sum_i \frac{c_i^{(8)}}{\Lambda^4} O_i^{(8)} + \mathcal{O}\left(\frac{1}{\Lambda^5}\right) . \tag{4.3}$$

The scale Λ does not need to be the same for all of these operators but can differ from case to case. This dependence is here absorbed into the Wilson coefficients $c_i^{(d)}$, the operators themselves are labeled $O_i^{(d)}$. At dimension five there exist only a few operators, all of which violate lepton number conservation. Among them is the Weinberg operator [30], giving rise to neutrino Majorana masses. In general all odd-dimensional operators violate B-L [31], which according to current experimental knowledge seems to be an accidental symmetry of the SM, so they must be strongly suppressed. Therefore, most studies focus on contributions from even-dimensional operators. At dimension six there exist 59 allowed structures, leading to a total of nearly 2500 possible operators [32].

4.2. Electroweak Chiral Lagrangian

When interested specifically in effects from beyond the Standard Model (BSM) in the Higgs sector, SMEFT only offers a limited spectrum of possible models and operators. A more general approach is to incorporate the Higgs not as a $SU(2)_\mathrm{L}$ doublet, as it is done in the SM, but the h field itself as a singlet and the corresponding Goldstone bosons in

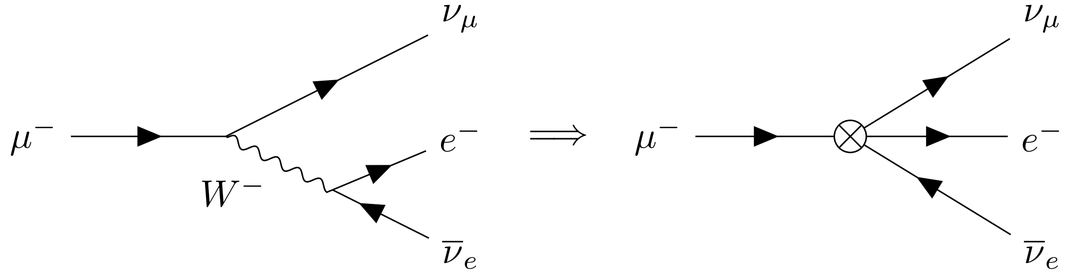

Figure 4.1.: Muon decay in the full SM and after integrating out the W boson, i.e. in Fermi Theory.

a non-linear way by means of an exponential function. The description in this section follows [33]. The leading order Lagrangian of such a theory, often called Electroweak Chiral Lagrangian (EWChL) [34–37], reads

$$\begin{aligned}
\mathcal{L}_2 = & -\frac{1}{4}B_{\mu\nu}B^{\mu\nu} - \frac{1}{4}W^a_{\mu\nu}W^{a,\mu\nu} - \frac{1}{4}G^b_{\mu\nu}G^{b,\mu\nu} + \sum_{\Psi=Q_\mathrm{L},L_\mathrm{L},U_\mathrm{R},D_\mathrm{R},E_\mathrm{R}} \overline{\Psi}\, i\not{D}\, \Psi && (4.4)\\
& + \frac{v^2}{4}\mathrm{Tr}\left[\left(D_\mu\Omega\right)^\dagger D^\mu\Omega\right](1+F_\Omega(h)) + \frac{1}{2}(\partial_\mu h)(\partial^\mu h) - V(h) && (4.5)\\
& - v\left[\overline{Q}_\mathrm{L}\left(Y_u + \sum_{n=1}^{\infty} Y_u^{(n)}\left(\frac{h}{v}\right)^n\right)\Omega\, P_+\, Q_\mathrm{R} + \overline{Q}_\mathrm{L}\left(Y_d + \sum_{n=1}^{\infty} Y_d^{(n)}\left(\frac{h}{v}\right)^n\right)\Omega\, P_-\, Q_\mathrm{R}\right.\\
& \qquad \left. + \overline{L}_\mathrm{L}\left(Y_e + \sum_{n=1}^{\infty} Y_e^{(n)}\left(\frac{h}{v}\right)^n\right)\Omega\, P_-\, L_\mathrm{R} + h.c.\right] . && (4.6)
\end{aligned}$$

In this Lagrangian, $Q_\mathrm{L}, L_\mathrm{L}$ are the usual left-handed quark and lepton doublets, $U_\mathrm{R}, D_\mathrm{R}, E_\mathrm{R}$ the corresponding right-handed singlets and $\Omega = \exp\left(2i\,\frac{\phi^a\sigma_a}{v}\right)$ is an exponential representation of the Goldstone modes ϕ^a, on which the covariant derivative acts like

$$D_\mu\Omega = \partial_\mu\Omega + igW^a_\mu\sigma_a\,\Omega - ig'B_\mu\sigma_3\,\Omega\ .$$

For the sake of a more compact notation, we introduce

$$Q_\mathrm{R} = \begin{pmatrix} U_\mathrm{R} \\ D_\mathrm{R} \end{pmatrix}\ ,\quad L_\mathrm{R} = \begin{pmatrix} 0 \\ E_\mathrm{R} \end{pmatrix}\quad \text{with}\quad P_+ = \begin{pmatrix} 1 & 0 \\ 0 & 0 \end{pmatrix}\ ,\quad P_- = \begin{pmatrix} 0 & 0 \\ 0 & 1 \end{pmatrix}$$

as an alternative way of writing of the right-handed fermionic degrees of freedom. The Higgs potential functions are

$$F_\Omega(h) = \sum_{n=1}^{\infty} f_{\Omega,n}\left(\frac{h}{v}\right)^n \quad \text{and} \quad V(h) = v^4\sum_{n=2}^{\infty} f_{V,n}\left(\frac{h}{v}\right)^n\ . \tag{4.7}$$

The Lagrangian $\mathcal{L}_2$ consists of three main parts: The first line (4.4) corresponds to the SM gauge boson and fermion kinetic terms as introduced in (2.3) and (2.4) without any modifications. The second and third lines, (4.5) and (4.6), describe the Higgs potential and Yukawa interactions. Choosing

$$f_{\Omega,1} = 2\ ,\quad f_{\Omega,2} = 1\ ,\quad f_{V,2} = f_{V,3} = \frac{m_h^2}{2\,v^2}\ ,\quad f_{V,4} = \frac{m_h^2}{8\,v^2}\ ,\quad Y_f^{(1)} = Y_f$$

and all other coefficients in the sums in (4.6) and (4.7) to be zero leads back to the Standard Model and reproduces (2.5) and (2.6). From this form of $\mathcal{L}_2$ it becomes apparent that the main purpose of the EWChL is to study the Higgs sector [38–40].

Since (4.5) and (4.6) contain arbitrary powers of the Goldstone and Higgs fields, the counting and ordering via conanical mass dimension as practised in SMEFT cannot be applied. Instead, in analogy to chiral perturbation theory used for the description of pions, kaons and other mesons, one defines *chiral dimensions* as follows [41]:

$$d_\chi(A^\mu, \phi, h, v, f_{\Omega,n}) = 0\ ,\quad d_\chi(\partial^\mu, \overline{\Psi}\Psi, g, Y) = 1 \quad \text{and} \quad d_\chi(f_{V,n}) = 2\ . \tag{4.8}$$

This logic results in a simple relation between the chiral dimension d_χ and loop order L of an interaction, $d_\chi = 2L+2$. With this counting, $\mathcal{L}_2$ in (4.4) ff. is the most general Lagrangian of chiral dimension two that can be constructed from SM field content. Next-to-leading order (NLO) effects at $d_\chi = 4$ then come from a mixture of one-loop diagrams with vertices from $\mathcal{L}_2$ and tree level diagrams from the next higher order Lagrangian $\mathcal{L}_4$. The latter is too long to be given here, but all parts of it relevant for this thesis will be listed and explained later in chapter 6. More detailed discussions can be found in [35, 36, 40].

5. Interpolation Grids for Dijet Production at NNLO QCD

The discovery and increasingly precise description of the SM as outlined in chapter 2 was made possible by a plethora of different experiments, many of which were operated at colliders. The concept of accelerating particles with magnets, colliding them with each other and observing the outcome has proven to be very insightful for the study of the fundamental building blocks and concepts of nature. Various technical concepts have been developed and implemented, allowing for collisions of different types of particles. Today, in the year 2024, three large collider facilities are operative: The Relativistic Heavy Ion Collider (RHIC) [42], part of the Brookhaven National Laboratory, hosts the PHENIX [43] and STAR [44] experiments, trying to better understand the quark-gluon-plasma and related phenomena [45]. Another one, SuperKEKB at the KEK research center in Japan, hosts the Belle II experiment [46, 47], investigating the physics of B mesons at the high precision and high intensity frontier, using an electron-positron-collider. The third and by far largest one, at CERN along the border between France and Switzerland near Geneva, is the Large Hadron Collider (LHC) [48]. As the title already suggests, this thesis focuses on the latter one, which probes particle physics at the high energy frontier. Being situated in the 27 km long circular tunnel previously used by LEP [49], the LHC is currently the highest energetic accelerator worldwide, reaching center of mass energies of up to 14 TeV. It has been operative since 2009 when it started with proton-proton collisions at $\sqrt{s} = 7$ TeV, which was later increased first to 8 TeV, then 13 TeV and lately 13.6 TeV. The tunnel has four interaction points which host the experiments ALICE [50], ATLAS [51], CMS [52] and LHCb [53]. The largest two of them are ATLAS and CMS, both serving as multi-purpose-detectors. This setup allows for two independent observations of the same physics via different measurement methodologies, thus not only delivering experimental results but also offering a cross-check thereof. A very prominent finding of the LHC was the discovery of the Higgs boson in 2012 [54, 55]. In future stages, both the center of mass energy and luminosity are expected to grow further, leading to the so-called High-Luminosity LHC (HL-LHC). This phase will allow for an even more precise examination of the SM or any deviations from it, possibly leading to the next big discovery.

5.1. The need for fast and precise QCD calculations

The LHC is - in clear distinction to the previously mentioned SuperKEKB - colliding two beams of protons. On the positive side, this allows to reach higher energies, since protons only produce a very tiny fraction of the synchrotron radiation electrons emit. On the negative side, however, hadronic initial states induce a far more complicated background

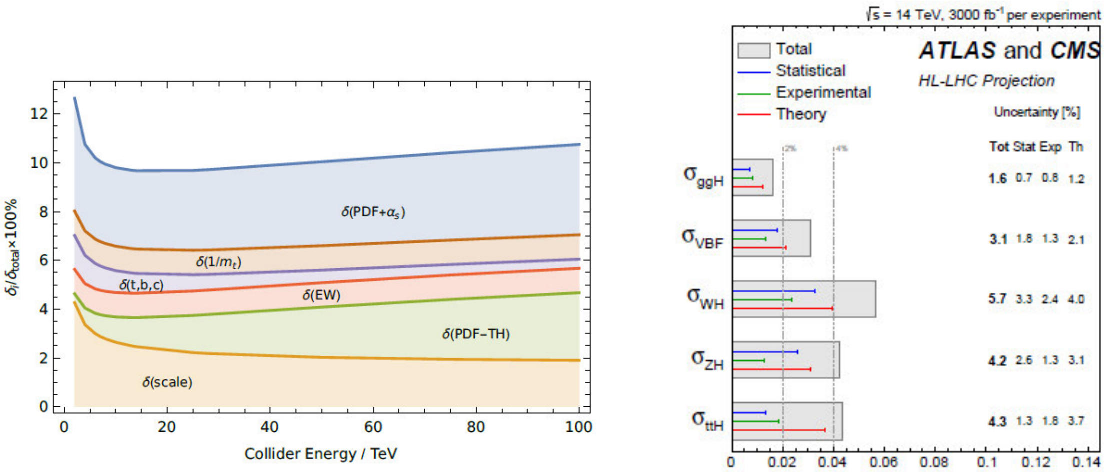

(a) Relative uncertainty budget of Higgs production calculations for hadron colliders. The top mass uncertainties shown by the brown band have already been solved and removed [56]. All other contributions still remain, the PDF and α_s part being the largest one independent of the collider energy. The figure is taken from [57].

(b) Uncertainty estimations for ATLAS and CMS at the upcoming HL-LHC. The predicted theory uncertainty for ttH is twice as large as the statistical and experimental ones, it needs to get smaller. The figure is taken from [58].

Figure 5.1.: Charts underlining the necessity of more precise PDF and α_s estimations.

and many non-perturbative effects. Since protons are bound states, the factorisation theorem - as outlined in section 3.1 - has to be applied for any calculation of observables. Therefore, every theoretical result can only be as precise as the empirical knowledge about the parton distribution functions (PDFs). Figure 5.1 (a) illustrates why this is a problem: For Higgs production, PDF and α_s uncertainties are the most significant contribution to the overall error budget. Throughout the high luminosity phase of the LHC (HL-LHC), experimental and statistical uncertainties are expected to shrink further. In order to avoid problematic situations like shown in figure 5.1 (b), the theory side has to keep up with both more exact perturbative calculations as well as more reliable fits and uncertainty estimations for said PDFs. These fits rely on computing time expensive iterative procedures, requiring a lot of CPU power to achieve even marginal gains in precision. Advances at the high precision frontier thus heavily rely on tricks to circumvent this bottleneck.

5.2. The APPLfast project

One way to make PDF and α_s fits more efficient is to process and sort the theoretical results in a different way than usual. The idea of writing them in the form of grids was simultaneously developed by the `APPLgrid` [59] and `fastNLO` [60, 61] collaborations, which combined efforts to create the `APPLfast` interface. After the first application of the program on deep inelastic scattering data from HERA led to promising results [62], it was also used for fits to ATLAS and CMS measurements [63]. The results outlined in section 5.4 are a continuation of the work presented in this last-mentioned paper, however they use a newer version of `APPLfast` and more precise input on both the theoretical and experimental sides.

5.2.1. Monte Carlo event generation

Since perturbation theory is the best analytical tool available for collider calculations, it is applied nearly whenever it is mathematically possible. For QCD, the expansion of the perturbative series is done with respect to $\alpha_s := \frac{g_s^2}{4\pi}$. Analogous to what was written in (3.8) for the scalar toy model, an observable then takes the form

$$\sigma_{ab\to X}(x, \alpha_s, \mu) = \sum_k \left(\frac{\alpha_s(\mu_R)}{2\pi}\right)^{k+r} \sigma^{(k)}_{ab\to X}(x, \mu) \,, \tag{5.1}$$

where r is the power of α_s of the leading order. x denotes the momentum fraction of partons and μ indicates any scale dependence. On the right hand side of the equation the latter shows up multiple times: As introduced in section 3.4, the coupling itself is dependent on the renormalisation scale μ_R; moreover, the observable can contain factors of both μ_R and μ_F, either from factorisation or logarithms in the virtual component.

Since the calculation of an observable at higher orders often involves very complicated functions and integrals, the evaluation of which is either impossible or at least very hard and time-expensive to perform analytically with standard computing tools, numerical approaches are an advantageous option to use. Monte Carlo (MC) event generators provide the input for such an endeavor: They generate kinematic points and configurations, i.e. energy-momentum four-vectors of particles in the initial and final states of scattering processes. The distribution of these points across the whole accessible phase space happens with respect to physically motivated probability density and weighting functions. In case the initial state is hadronic, the event generator also chooses numerical values for the corresponding momentum fractions x and includes a discretised version of the factorization theorem (3.1). For proton-proton collisions this yields

$$\begin{aligned}\sigma_{pp\to X}(x, \alpha_s, \mu) = \sum_{a,b} \sum_k \sum_{m=1}^{N_{\mathrm{MC}}} \left(\frac{\alpha_s(\mu_{R,m})}{2\pi}\right)^{k+r} \quad &\times \quad \sigma^{(k)}_{ab\to X,\, m}\, w^{(k)}_{ab\to X,\, m} \\ &\times \quad f_a(x_{a,m}, \mu_{F,m})\, f_b(x_{b,m}, \mu_{F,m}) \,,\end{aligned} \tag{5.2}$$

where N_{MC} is the number of points generated, $\sigma^{(k)}_{ab\to X,\, m}$ is the cross section (or general observable) result for point m with incoming partons a, b at perturbative order k and $w^{(k)}_{ab\to X,\, m}$ is the weight associated with it. Since the scales are often chosen dynamically, i.e. proportional to a kinematic quantity of the process, like the momentum transfer, they depend on the selected phase space point and also carry the index m. The higher N_{MC}, the better the whole phase space is sampled and the more precise is the result.

What is missing in (5.2) are corrections stemming from non-perturbative contributions to the process. Some event generators like `PYTHIA` [64] or `Herwig` [65, 66] allow for the inclusion of such effects like e.g. multi-parton interactions, hadronization or parton showers. Within the `APPLfast` workflow, however, we do the calculation only at the parton level, using the partonic event generator `NNLOJET` [67, 68]. Therefore, the final states of `APPLfast` QCD calculations are jets rather than mesons or baryons.

5.2.2. Interpolation workflow

`APPLfast` is based on the idea of interpolating results and saving them in the format of grids. This logic can be easily explained on a simple function defined over a real interval. Let $I = [a, b]$ with $a, b \in \mathbb{R}$, $a < b$ and $f : I \longrightarrow \mathbb{R}$ continuous. We can split the interval into $N + 1$ nodes, with the first and last nodes being defined as the edges, $a = x^{[0]}$, $b = x^{[N]}$. Now we can further define a set of functions $E_i : I \longrightarrow \mathbb{R}$, $i \in \{0, \dots, N\}$, obeying the conditions $1 = \sum_{i=0}^{N} E_i(x) \;\; \forall x \in I$ and $E_i\left(x^{[i]}\right) = 1 \;\; \forall i \in \{0, \dots, N\}$. This simple definition allows to approximate f as

$$f(x) \simeq \sum_{i=0}^{N} f^{[i]} E_i(x) \text{ with } f^{[i]} = f(x^{[i]}) \; . \tag{5.3}$$

Figure 5.2 shows such interpolations for the case $a = -2$, $b = 2$, equidistant spacing of the nodes and $E_i(x) \sim \frac{1}{2}\left(\cos^2(x) + 1\right)$. As expected intuitively, the approximation gets better the larger N is. Other dimensions to tune are the distribution of nodes along the interval and the precise functional form of the basis elements E_i. The latter does, however, become less important the larger N is, since the peaks get more narrow and resemble a hat function or - in extreme cases - a smeared delta peak. If there is a second continuous function $g : I \longrightarrow \mathbb{R}$ such that the product $f \cdot g$ is integrable over I, we can also approximate their convolution integral as

$$\int_a^b f(x) g(x)\, \mathrm{d}x \simeq \sum_{i=0}^{N} f^{[i]} g_{[i]} \text{ with } g_{[i]} := \int_a^b E_i(x) g(x)\, \mathrm{d}x \; . \tag{5.4}$$

This relation is very useful when it comes to computing the right hand side of (3.1). Since such evaluations have to be performed repeatedly for every PDF fit, the interpolation and approximation can save sizable amounts of computing time.

For hadronic collisions there exist four variables to be interpolated, namely x_a, x_b, μ_R, and μ_F. Therefore, we also need four sets of functions $E_i(x_a)$, $E_j(x_b)$, $E_v(\mu_R)$, $E_w(\mu_F)$. With these, (5.2) can be rewritten as

$$\sigma_{pp\to X}(x, \alpha_s, \mu) = \sum_{i,j,v,w=0}^{N} \sum_{a,b} \sum_{k} \left(\frac{\alpha_s^{[v]}}{2\pi} \right)^{k+r} f_a^{[i,w]} f_b^{[j,w]} \times \sigma^{(k)}_{ab\to X\;[i,j,v,w]} \; , \tag{5.5}$$

where the last object is defined as

$$\sigma^{(k)}_{ab\to X\;[i,j,v,w]} := \sum_{m=1}^{N_{\mathrm{MC}}} E_i(x_{a,m})\, E_j(x_{b,m})\, E_v(\mu_{R,m})\, E_w(\mu_{F,m}) \times \sigma^{(k)}_{ab\to X,\,m}\, w^{(k)}_{ab\to X,\,m} \; . \tag{5.6}$$

These formulae very nicely showcase the heart of the `APPLfast` logic: The time consuming part in the calculation of observables is the evaluation of phase space points, i.e. the computation of $\sigma^{(k)}_{ab\to X,\,m}\, w^{(k)}_{ab\to X,\,m}$. Once this part is done and the sum over MC points and interpolation functions is executed, the results of (5.6) are saved in grids. Finally, the rest of (5.5) is fast and easy to evaluate. Most importantly, this allows for an a posteriori

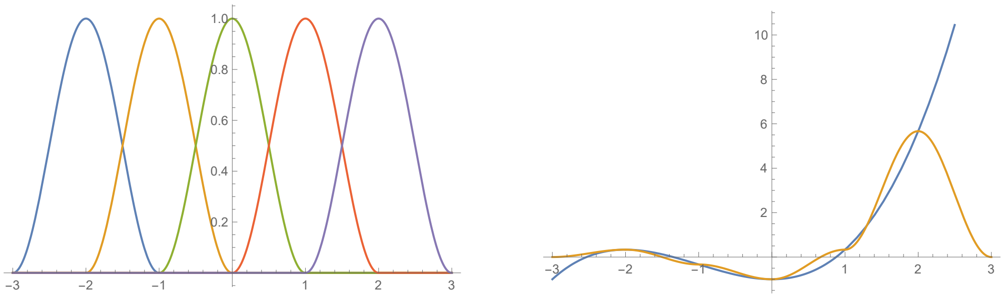

(a) Plot of interpolation functions for $N = 5$.

(b) Comparison of a polynomial (blue) and the approximation to it (orange).

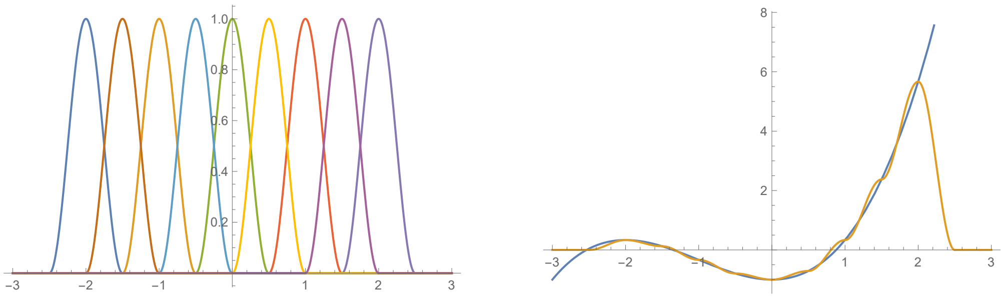

(c) Plot of interpolation functions for $N = 9$.

(d) Comparison of a polynomial (blue) and the approximation to it (orange).

Figure 5.2.: Different interpolations and their effect on the accuracy of the approximation. The higher number of nodes leads to a more accurate description of f.

change of the input value of the strong coupling constant $\alpha_s^{[v]}$ or of the PDFs $f_a^{[i,w]}$ and $f_b^{[j,w]}$. Conversely, this also means that these values, α_s and PDFs, can be varied, fitted and extracted without the necessity to rerun the event generator, i.e. without the repeated investment of large computing resources.

On the `fastNLO` side, the actual grid entries usually are not the values $\sigma^{(k)}_{ab\to X\,[i,j,v,w]}$, but the factors of a further decomposition with respect to the logarithmic scale factors they contain:

$$\sigma^{(k)}_{ab\to X,\,m} = \sum_{\alpha+\beta\leq k} \sigma^{(k|\alpha,\beta)}_{ab\to X,\,m} \, \log^{\alpha}\left(\frac{\mu^2_{R,m}}{\mu_0^2}\right) \log^{\beta}\left(\frac{\mu^2_{F,m}}{\mu_0^2}\right) . \tag{5.7}$$

μ_0 is a constant reference scale to render the entry of the logarithm dimensionless. Often the mass of a particle present in the process of interest or the momentum transfer is chosen as its value. Defining

$$L_{R/F} := \log\left(\frac{\left(\mu_{R/F}\right)^2}{\mu_0^2}\right) \text{ and } L_R^{[v]} := \log\left(\frac{\left(\mu_R^{[v]}\right)^2}{\mu_0^2}\right) \text{ and } L_F^{[w]} := \log\left(\frac{\left(\mu_F^{[w]}\right)^2}{\mu_0^2}\right) \tag{5.8}$$

allows to rewrite (5.5) and (5.6) in a different form:

$$\sigma_{pp\to X}(x,\alpha_s,\mu) = \sum_{i,j,v,w=0}^{N} \sum_{a,b} \sum_{k} \sum_{\alpha+\beta\leq k} \left(\frac{\alpha_s^{[v]}}{2\pi}\right)^{k+r} \times f_a^{[i,w]} f_b^{[j,w]} \times \left(L_R^{[v]}\right)^{\alpha} \left(L_F^{[w]}\right)^{\beta} \times \sigma^{(k|\alpha,\beta)}_{ab\to X\ [i,j,v,w]} \tag{5.9}$$

with the actual grid entries

$$\sigma^{(k|\alpha,\beta)}_{ab\to X\ [i,j,v,w]} := \sum_{m=1}^{N_{\mathrm{MC}}} E_i(x_{a,m})\, E_j(x_{b,m})\, E_v(\mu_{R,m})\, E_w(\mu_{F,m}) \times \sigma^{(k|\alpha,\beta)}_{ab\to X,\,m}\, w^{(k)}_{ab\to X,\,m}\,. \tag{5.10}$$

For simplicity, all four interpolations are written with the same N as the upper end of the sum, which in general does not have to be the case. There could be four different N_i, N_j, N_v and N_W. The calculations described in these equations are not separated between the event generator on one side and the grid interface and libraries on the other, but all of it is intertwined and executed at runtime. This way, the phase space sampling done in the warmup phase of `NNLOJET` and the interpolation grid spacing and node choice of `APPLgrid` or `fastNLO` can be adapted to each other most efficiently.

5.3. Jet production at colliders

As outlined in section 3.4.1, quarks and gluons do never show up individually but always prefer to be bound into color neutral objects. They hadronize, i.e. form baryons and mesons, clustered together in a collimated stream, and are finally measured as energy deposition in calorimeters. The reaction chain and outcome starting from one final state particle of the actual hard scattering process is called a jet.

5.3.1. Jet algorithms

For a rigorous definition of jet final states we need a prescription of how to recognize what part of often rather diffuse detector signatures belongs to a jet. Figure 5.3 shows a simple case in which the deposited energy of two neighboring jets is well-separated, such that a clear definition can be made even by the naked eye. In a realistic scenario, millions of such interactions occur simultaneously, producing large amounts of data every second, so an easy and fast algorithm for jet clustering is indispensable.

Another very important aspect is infrared safety: Not only on the theory side soft and collinear radiation leads to subtleties (see section 3.3.2), but also when it comes to jets it can make a difference. Since per definition, real radiation is of such a form that it cannot be resolved experimentally, i.e. does not influence the measurement, it should also not change the jet definition. Expressed mathematically, this means that any jet observable O_m that depends on the m four-momenta of final state partons must obey

$$O_m(p_1,\ldots,\lambda p_i,\ldots,p_j=(1-\lambda)p_i,\ldots,p_m) = O_m(p_1,\ldots,p_i,\ldots,p_{j-1},p_{j+1},\ldots,p_m) \tag{5.11}$$

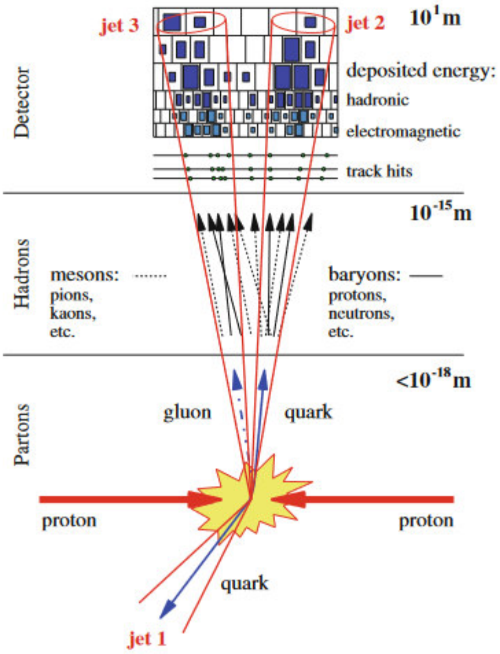

Figure 5.3.: Example picture of a multi-jet event, showing how detector results are grouped together. The figure is taken from [69].

and

$$\lim_{\lambda\to 0} O_m(p_1,\ldots,\lambda p_i,\ldots,p_m) = O_m(p_1,\ldots,p_{i-1},p_{i+1},\ldots,p_m)\ . \tag{5.12}$$

In other words: the collinear splitting of momentum p_i into p_i and p_j as in (5.11) or the addition of a soft particle with very small momentum λp_i as in (5.12) must not change the outcome. Examples of situations in which this is not the case are shown in figure 5.4.

The most-used type of infrared safe jet algorithms nowadays are so-called sequential recombination algorithms, prominent examples for which are the Durham k_T algorithm [71], the Cambridge/Aachen algorithm [72, 73] and the anti-k_T algorithm [74]. All of them apply the same basic logic: Initially there exist N four-momenta which were measured and should be grouped into $K \leq N$ jets. Now all distances d_{ij} between pairs of momenta and d_{iB} between momenta and the beam axis are calculated according to

$$d_{ij} = \min\left(p_{T,i}^{2k},\, p_{T,j}^{2k}\right)\frac{\Delta R_{ij}^2}{R^2} \tag{5.13}$$

$$d_{iB} = p_{T,i}^{2k} \tag{5.14}$$

with

$$\Delta R_{ij}^2 = (y_i - y_j)^2 + (\phi_i - \phi_j)^2\ . \tag{5.15}$$

ϕ is the azimuthal angle of the momentum vector and y is the rapidity, defined as

$$y = \frac{1}{2}\ln\left(\frac{E+p_z}{E-p_z}\right)\ . \tag{5.16}$$

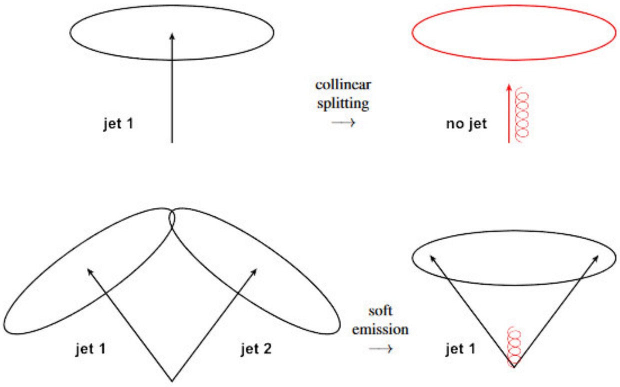

Figure 5.4.: Examples of collinear and soft unsafe behavior: In the upper row, the collinear emission of an additional gluon reduces the momentum of the quark below some threshold, such that no jet is recognized. In the lower row, the additional soft gluon leads to a state which was previously characterized as two jets to suddenly be interpreted as only one jet. Both of these scenarios conflict with the defining property of real radiation to produce a final state degenerate to the leading order one. The figure is taken from [70].

The *jet size* R is a constant number to be freely chosen between 0 and 1. It determines how large the resulting jets are in phase-space. Smaller R means more narrow jets, resulting in a larger number of them. After all the differences are calculated, the minimum is determined. If the minimal distance is one of those to the beam axis, the object the momentum belongs to is declared to be a jet. If, on the other hand, the minimum is a pair of momenta, the two are added and their sum is put back into the original set instead. In both cases, the number of momenta to still be clustered is reduced by one. This logic is now applied repeatedly, N times in total, until all momenta are grouped or defined as a jet. A flowchart of this procedure is shown in figure 5.5. The difference between k_T, Cambridge/Aachen and anti-k_T is only the value chosen for the exponent k of the transverse momenta when calculating the distances. For k_T it is $k = 1$, anti-k_T uses $k = -1$ and Cambridge/Aachen chooses $k = 0$. Both the CMS and ATLAS experiments use the anti-k_T algorithm, which is why the phenomenological calculations and fits presented in section 5.4 also do that.

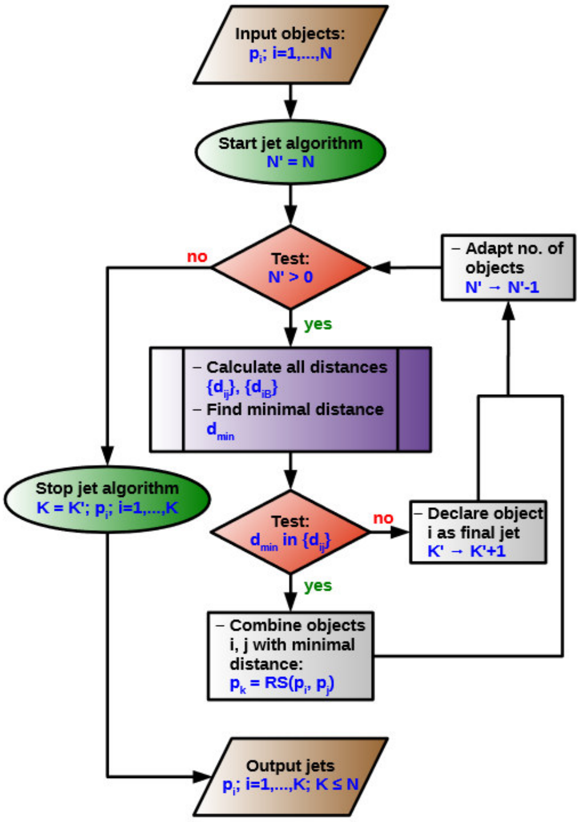

Figure 5.5.: Flowchart explaining the structure of a sequential recombination algorithm: N input momenta p_i are iteratively clustered, i.e. they are either declared a jet or two of them are combined until none of them is left. The output is again a list of momenta describing K jets, $K \leq N$. The figure is taken from [70].

5.3.2. Dijet kinematics

If at least two jets are found after the application of a jet algorithm, an event is considered a dijet event. The jets are ordered with respect to their transverse momentum p_T, the one with the highest being called "leading jet", the second highest second-leading jet and so on. The typical observables used for the description of dijet events are

$$\begin{aligned}\langle p_T \rangle &= \frac{1}{2}\left(p_{T,1} + p_{T,2}\right) && (5.17)\\ y^* &= \frac{1}{2}\left|y_1 - y_2\right| && (5.18)\\ y_b &= \frac{1}{2}\left|y_1 + y_2\right| \text{ and} && (5.19)\\ m_{12} &= \sqrt{\left(p_1 + p_2\right)^2}\,, && (5.20)\end{aligned}$$

where p_1 is the momentum of the leading and p_2 that of the second-leading jet, and equivalently for the rapidities y_1 and y_2. y^* can be understood as a measure for how much

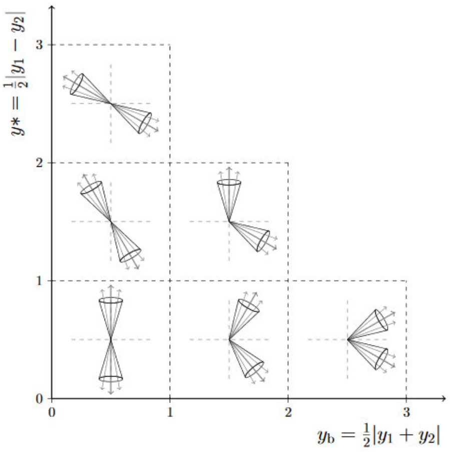

Figure 5.6.: Graphic illustration of the shapes of dijet events with different values for rapidity observables y^* and y_b. Low y_b means the two jets are nearly back-to-back, whereas high y_b indicates that both of them are headed in similar directions in the same hemisphere of the detector. y^* on the other hand describes how tilted the symmetry axis between the two jet cones is. The figure is from [75].

the jets are tilted towards the beam direction. y_b on the other hand quantifies the angle between the two jets, i.e. how much both are directed towards the same region of the detector. The meaning of these theoretical definitions is illustrated pictorially in figure 5.6.

5.4. Dijet production at full color at the LHC

As mentioned at the beginning of section 5.2, the `APPLfast` algorithm was already used with CMS and ATLAS data in the past [63]. Back then, calculations for both inclusive jet and dijet processes were made, but only the latter was used for α_s and PDF fits. Four different data sets, two from each experiment, were taken into account:

- CMS at $\sqrt{s} = 7$ TeV, anti-k_T with R=0.7, double differential in $m_{12} \in [197, 5058]$ GeV and $|y_{\text{max}}| \in [0.0, 2.5]$, dynamical scale $\langle p_T \rangle$ [76]
- CMS at $\sqrt{s} = 8$ TeV, anti-k_T with R=0.7, triple differential in $\langle p_T \rangle \in [133, 1784]$ GeV, $y^* \in [0.0, 3.0]$ and $y_b \in [0.0, 3.0]$ [77]
- ATLAS at $\sqrt{s} = 7$ TeV, anti-$k_T$with R=0.6, double differential in $m_{12} \in [260, 5040]$ GeV and $y^* \in [0.0, 3.0]$ [78]
- ATLAS at $\sqrt{s} = 13$ TeV, anti-k_T with R=0.4, double differential in $m_{12} \in [260, 9066]$ GeV and $y^* \in [0.0, 3.0]$ [79]

All of these sets except for the first one use the leading jet's transverse momentum rescaled by an exponential of the absolute rapidity difference, $p_{T,1} \cdot \exp(0.3\, y^*)$, as dynamical scale for both μ_R and μ_F. This at first glance odd choice is based on the studies in [80].

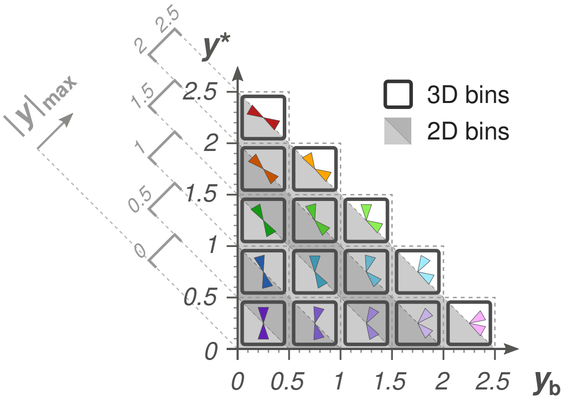

Figure 5.7.: Rapidity slicing in the CMS publication [81] describing 13 TeV dijet data. Both a triple differential option differentiating between y^* and y_b and a double differential variant only using $|y|_{\text{max}}$ are given.

Since the publication of [63] in 2022, CMS performed new dijet measurements at a center-of-mass energy of $\sqrt{s} = 13$ TeV, both double and triple differential [81]. The exact histogram definitions are as follows:

- CMS at $\sqrt{s} = 13$ TeV, anti-k_T with R=0.8, double differential in $m_{12} \in [249, 10050]$ GeV and $|y|_{\text{max}} \in [0.0, 2.5]$
- CMS at $\sqrt{s} = 13$ TeV, anti-k_T with R=0.8, triple differential in $m_{12} \in [306, 6094]$ GeV, $y^* \in [0.0, 2.5]$ and $y_b \in [0.0, 2.5]$

In these data sets the scale is chosen to be the dijet mass, m_{12}, for both μ_R and μ_F. Other than the 8 TeV triple differential data, which has rapidity bins of length 1.0 as shown in figure 5.6, the 13 TeV set uses a finer binning of only 0.5. This makes the comparison with double differential results, which always use the 0.5 rapidity binning, easier, as can be seen in figure 5.7.

This new experimental input is only one of the differences in the content of this thesis compared to [63]. The other, maybe even more important one is the development of a new version of `NNLOJET`, followed by advancements also on the `APPLfast` side and the interface connecting them. In addition to performance boosts and workflow optimizations, also the code necessary for the calculation of the full color structure for dijet production at NNLO has been implemented. Previously, only the leading color amplitude was available.

5.4.1. Expansion in color factors

To explain this difference between 'full' (FC) and 'leading' (LC) color, a recap of the structure of QCD is necessary. In Lagrange densities and effective operators, Gluons always show up in either a covariant derivative (2.7) or a field strength tensor (2.11). They are associated with either a $SU(3)$ generator T^a or structure constant f^{abc}. When calculating observables, the amplitudes containing these objects are squared and summed over polarisations, spins and color indices. At this point, general $SU(N)$ relations can be applied to simplify the result:

$$\mathrm{Tr}(T^a T^b) = T_R\, \delta^{ab} \quad \text{and} \quad \sum_{a,j} T^a_{ij} T^a_{jk} = C_F\, \delta_{ik} \quad \text{and} \quad \sum_{a,b} f^{abc} f^{abd} = C_A\, \delta^{cd} \tag{5.21}$$

with C_F and C_A being the eigenvalues of the lowest-dimensional Casimir operators in the fundamental and adjoint representations, respectively:

$$C_F = T_R\, \frac{N_c^2 - 1}{N_c} \quad \text{and} \quad C_A = 2\, T_R\, N_c\ . \tag{5.22}$$

All color indices have to be contracted until every generator and structure constant is removed:

$$\sum_a T^a_{ij} T^a_{kl} = T_R \left(\delta_{il}\delta_{kj} - \frac{1}{N_c} \delta_{ij}\delta_{kl} \right)\ , \tag{5.23}$$

such that in the end only two objects remain, namely $T_R = \frac{1}{2}$ and $N_c = 3$ for $SU(3)$. Since T_R is common to all of these equations, it can be factored out. The rest of the amplitude then appears as a series in N_c. (5.23) introduces a hierarchy between two ways of contracting indices, the second one being suppressed by a factor of $\frac{1}{N_c}$ with respect to the first one. For complicated processes, this happens more often, and in the end there are multiple fermionic strings with different color prefactors. For the sake of simplicity, sometimes the most suppressed ones are left out. The resulting so-called 'leading color' amplitude is then only correct in good approximation, whereas 'full color' indicates that all terms are being included, thus the result is exact (with respect to the color structure).

Multiple studies for jet production [82–85] were performed with `NNLOJET` within the leading color approximation and it was proven [86] that the sub-leading contributions are indeed negligible for single jet inclusive cross sections. However, based on recent developments for colorful antenna subtraction at NNLO QCD for jet observables [87, 88], it has been shown that for dijet production it can make a sizable difference whether FC or LC amplitudes are used [89]. The effects are non-uniformly distributed across the kinematic range, i.e. they do not only lead to a constant enhancement factor but change the slope of the histograms. The size of sub-leading color corrections can reach up to the order of 5% for triple differential dijet cross sections. Therefore, in the present day era of highly accurate experimental measurements, full color results are strictly necessary.

5.4.2. Code Validation

Since the introduction of full color dijet calculations was part of new versions of all involved programs, proper validation was necessary. A very good way of testing the reliability of the `APPLfast` algorithms is to look at the so-called closure plots: As the interpolation logic described in section 5.2.2 is only an approximation, one must test how well it reproduces the pure event generator results. Figures 5.8 and 5.9 show the ratio $\frac{\texttt{APPLfast}}{\texttt{NNLOJET}}$ and the asymmetry $\frac{\texttt{APPLfast-NNLOJET}}{\texttt{APPLfast+NNLOJET}}$ values differential in m_{12} for the innermost rapidity bins ($y^* \in [0.0, 0.5]$) of the ATLAS 7 TeV and 13 TeV data sets, respectively. In order to plot both nicely in the same diagram, the asymmetry is shifted upwards by a constant of one. In both cases, results are shown for each channel - leading order (LO), virtual (V), real (R), double virtual (VV), real virtual (RV), double real a (RRa) and double real b (RRb) - separately and for the total NNLO combined. The distinction between RRa and RRb regions is a technical detail of the implementation in `NNLOJET` that has no further bearing on the results presented. Overall a very nice agreement at the sub-per-mille level can be seen, proving that the interpolation works as intended.

Other than that, the general viability of the outcome has to be investigated. The closure plots only tell how good the `APPLfast` and `NNLOJET` results match, but make no statement about whether the latter actually delivers sensible numbers. To this end, fits to experimental data have to be performed. Since one goal of the project is to provide a precise value of the strong coupling α_s, each data set is checked for the compatibility of such a fit result with the PDG world average of $\alpha_s(m_Z) = 0.1180 \pm 0.0009$ [90, 91]. The fits are performed using a standard χ^2 minimization logic, their outcome for both ATLAS and CMS 7 TeV data can be found in figures 5.10 and 5.11. Seven different PDF sets are used for comparison, all leading to agreeable results with χ^2 per degree of freedom (χ^2/ndf) only little larger than one and α_s close to the given world average value. The error bars include fit, data and PDF uncertainties, but no scale variations to asses the effect of missing higher orders.

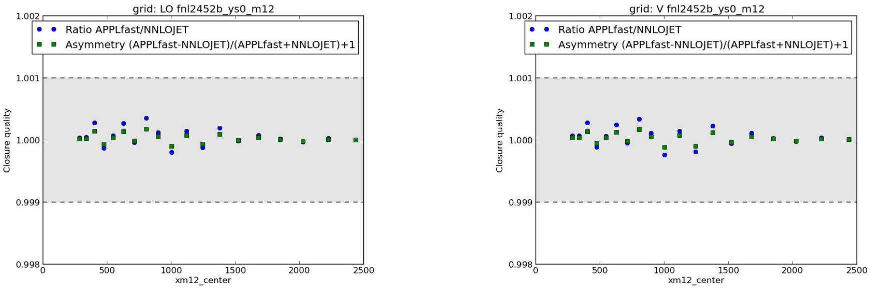

(a) Closure plot for leading order.

(b) Closure plot for the virtual channel.

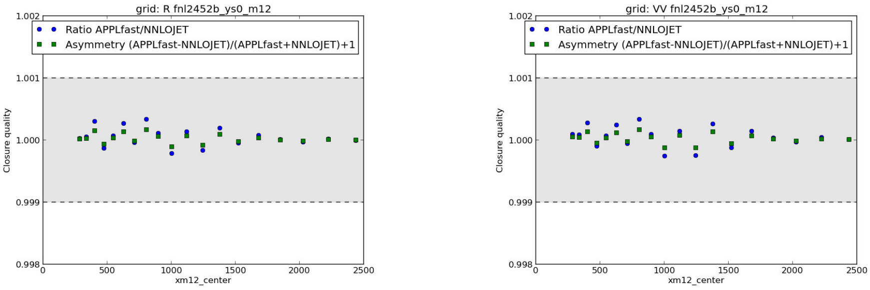

(c) Closure plot for the real channel.

(d) Closure plot for the double virtual channel.

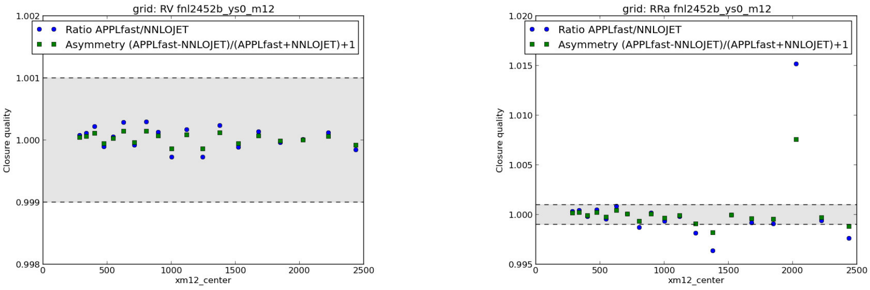

(e) Closure plot for the real virtual channel.

(f) Closure plot for the double real a channel.

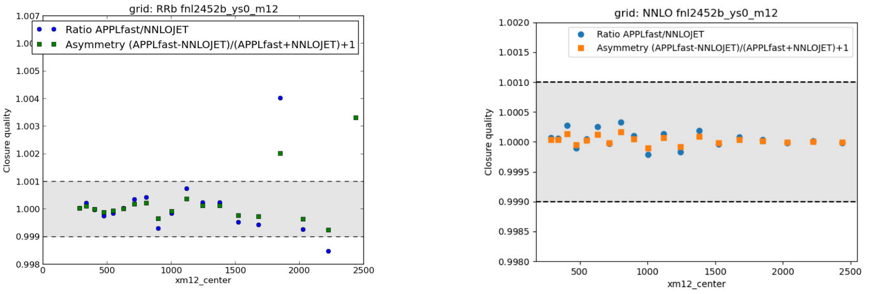

(g) Closure plot for the double real b channel.

(h) Closure plot for all channels at NNLO combined.

Figure 5.8.: Closure plots for ATLAS 7 TeV data, showing the ratio and asymmetry between `APPLfast` and `NNLOJET` results. Despite a few outliers located far offside in the double real channels, the overall agreement is very good. The plots were made by Fazila Ahmadova and Daniel Britzger (MPI Munich) for the `APPLfast` collaboration.

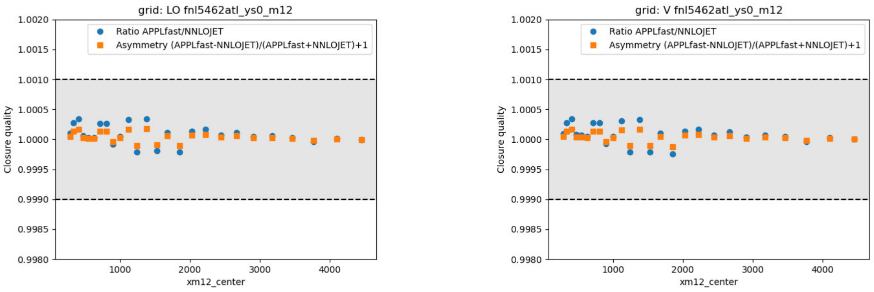

(a) Closure plot for leading order.

(b) Closure plot for the virtual channel.

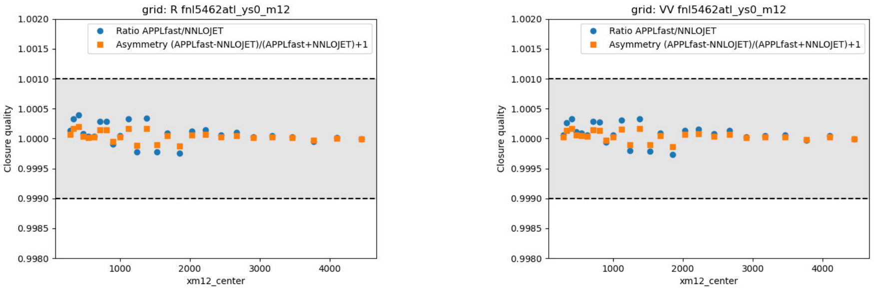

(c) Closure plot for the real channel.

(d) Closure plot for the double virtual channel.

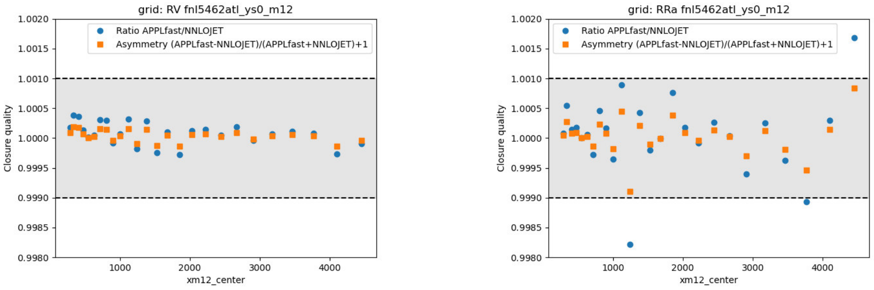

(e) Closure plot for the real virtual channel.

(f) Closure plot for the double real a channel.

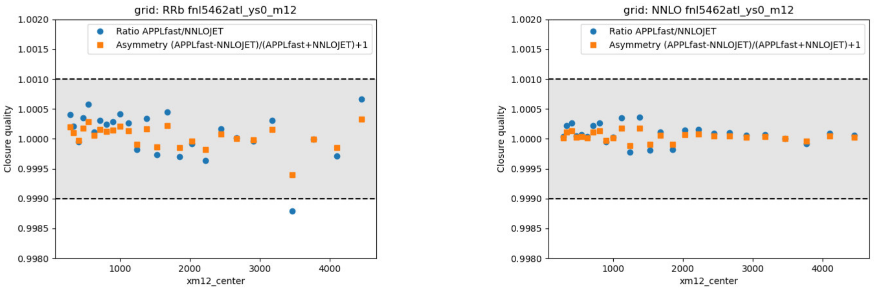

(g) Closure plot for the double real b channel.

(h) Closure plot for all channels at NNLO combined.

Figure 5.9.: Closure plots for ATLAS 13 TeV data, showing the ratio and asymmetry between `APPLfast` and `NNLOJET` results. The double real channels again contain a few tiny outliers, but overall the interpolation reaches the desired precision. The plots were made by Fazila Ahmadova and Daniel Britzger (MPI Munich) for the `APPLfast` collaboration.

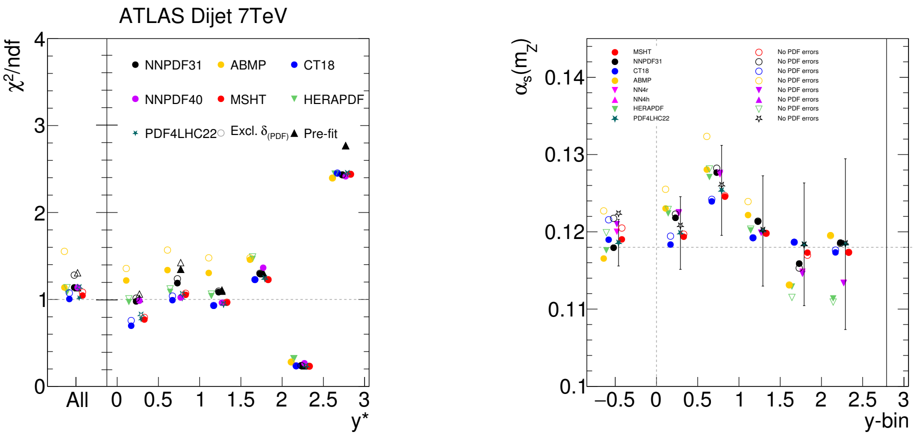

(a) χ^2 per degree of freedom for each rapidity bin separately and the total set.

(b) α_s central values and error margins for each rapidity bin separately and the total set (on the left at -0.5). The results for the last bin are so far off that they cannot be shown in the plot.

Figure 5.10.: Results of the α_s fit to ATLAS 7 TeV data with seven different PDF sets, both including (filled dots) and omitting (empty dots) the PDF error. It can clearly be seen that the outermost rapidity bin yields nonsensical results way off the world average. The fifth bin ($2.0 \leq y^* < 2.5$) shows very good agreement only by chance, while the innermost ones are promising. The plots were made by Daniel Britzger (MPI Munich) for the `APPLfast` collaboration.

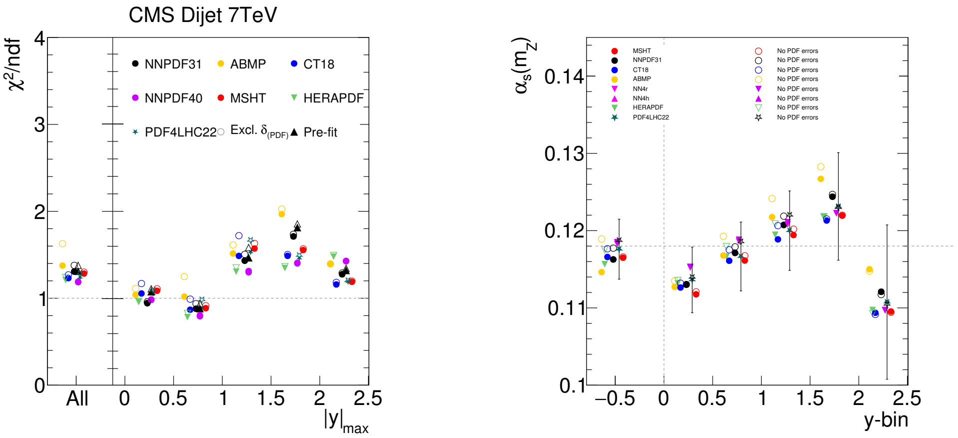

(a) χ^2 per degree of freedom for each rapidity bin separately and the total set.

(b) α_s central values and error margins for each rapidity bin separately and the total set (on the left at -0.5).

Figure 5.11.: Results of the α_s fit to CMS 7 TeV data with seven different PDF sets, both including (filled dots) and omitting (empty dots) the PDF error. Overall we find very good agreement with the expected value. The plots were made by Daniel Britzger (MPI Munich) for the `APPLfast` collaboration.

5.4.3. Cross section results

Since our calculations were parameterized such that they best describe the measured data, i.e. center-of-mass energies, jet algorithms, cone sizes, observables, binning, scales and any other settings were chosen such that they are equal to what the experimentalists used in their analysis, it was to be expected that our results match well with said data. The fact that this match is indeed very strong can on the one hand be interpreted as a validation for our program and on the other hand as another confirmation of the Standard Model, since no new physics effects seem to contribute. Given that the results are qualitatively very similar for all examined data sets, only one of them, namely ATLAS 7 TeV, is discussed here in detail. However, the whole bunch of sets will be used later in section 5.4.4 for the determination of the strong coupling constant at $\mu_R = m_Z$.

Figure 5.12 shows the total cross section separately for every rapidity bin and channel as well as for the combined NNLO. The shape proportional to $\frac{1}{m_{12}}$ is identical to what can be found in figure five in [78], the only difference being that the latter has a logarithmic scale for m_{12}, whereas in figure 5.12 it is linear. The cross sections spans a total of eight orders of magnitude, starting at $\sim 10^6$ pb for low m_{12} and ending at $\sim 10^{-2}$ pb for high m_{12}. This behavior reflects the running of the strong coupling, which is larger at lower scales and thus prefers jets with low momentum over high energetic ones.

In order to disentangle the contributions of every channel, figure 5.13 gives a different picture of the same result. Two interesting features can be seen: First, there seems to be some cancellation between the real and real virtual components on the one side and the virtual and double virtual ones on the other. Second, the higher the rapidity, the larger the size of this cancellation gets, for $y^* \geq 2.0$ the (double) virtual contribution even surpasses the leading order one. The double real part(s) on the other hand only make up around 5% or less of the total result, regardless of the rapidity.

This latter fact is beneficial when looking at figure 5.14: For every rapidity bin and nearly every value of the dijet mass, the total uncertainty of the result is dominated by the contribution from the 'double real a' region. This is a usual and well-known feature, which can be tackled only by investing more CPU time or, equivalently, more MC points. For a double differential result like this with an overall uncertainty of around one percent, computing time of the order of half a million hours is necessary. For the triple differential CMS 8 TeV and 13 TeV sets nearly double this computational effort was required.

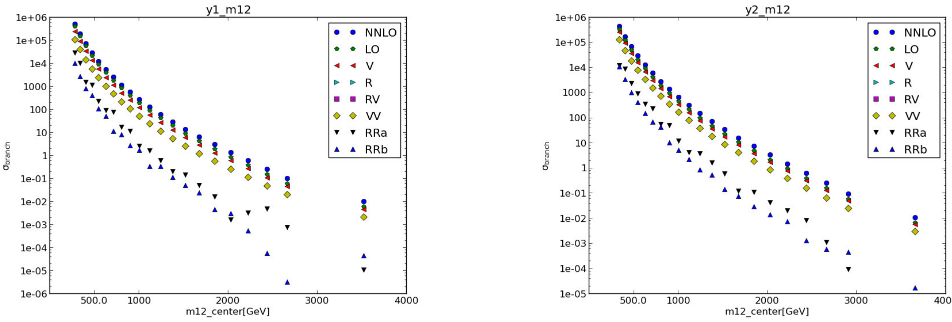

(a) Cross section differential in dijet mass m_{12} for $0.0 \leq y^* < 0.5$.

(b) Cross section differential in dijet mass m_{12} for $0.5 \leq y^* < 1.0$.

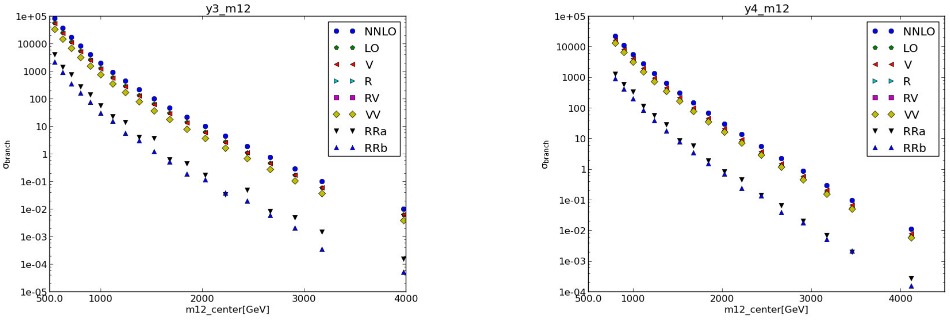

(c) Cross section differential in dijet mass m_{12} for $1.0 \leq y^* < 1.5$.

(d) Cross section differential in dijet mass m_{12} for $1.5 \leq y^* < 2.0$.

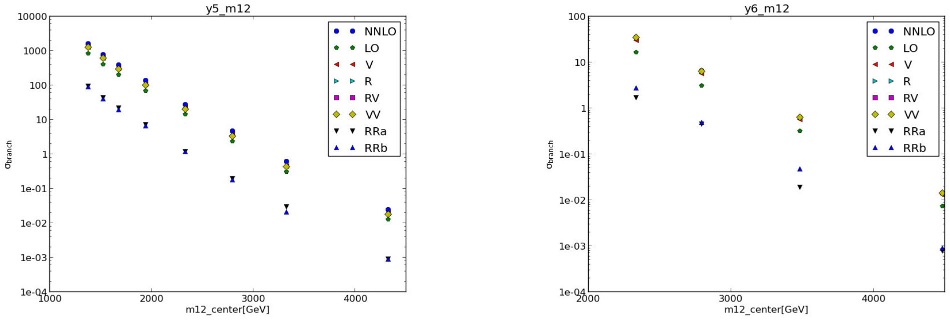

(e) Cross section differential in dijet mass m_{12} for $2.0 \leq y^* < 2.5$.

(f) Cross section differential in dijet mass m_{12} for $2.5 \leq y^* < 3.0$.

Figure 5.12.: Cross section (in pb) results for dijet production at the ATLAS experiment with $\sqrt{s} = 7$ TeV at full color NNLO QCD, double differential in dijet mass and rapidity. The plots were made by Fazila Ahmadova and Daniel Britzger (MPI Munich) for the `APPLfast` collaboration.

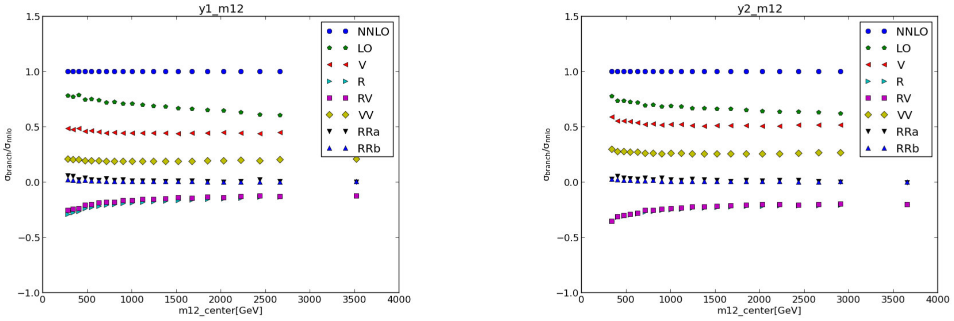

(a) Relative contribution to the cross section per channel, differential in dijet mass m_{12} for $0.0 \leq y^* < 0.5$.

(b) Relative contribution to the cross section per channel, differential in dijet mass m_{12} for $0.5 \leq y^* < 1.0$.

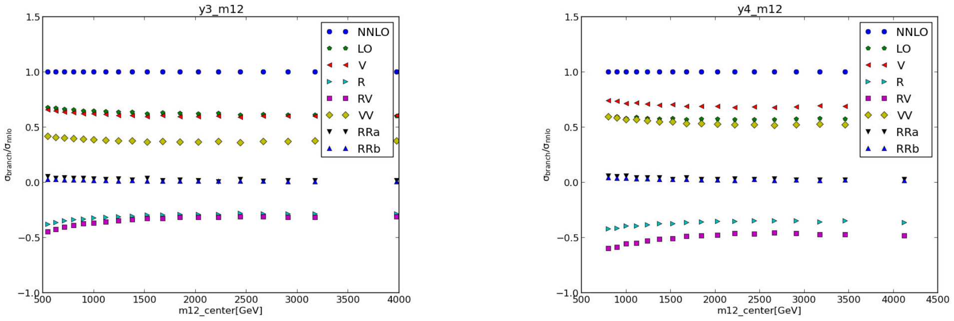

(c) Relative contribution to the cross section per channel, differential in dijet mass m_{12} for $1.0 \leq y^* < 1.5$.

(d) Relative contribution to the cross section per channel, differential in dijet mass m_{12} for $1.5 \leq y^* < 2.0$.

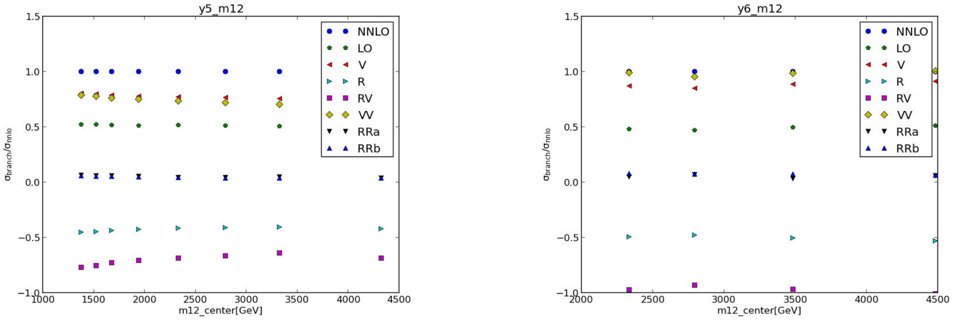

(e) Relative contribution to the cross section per channel, differential in dijet mass m_{12} for $2.0 \leq y^* < 2.5$.

(f) Relative contribution to the cross section per channel, differential in dijet mass m_{12} for $2.5 \leq y^* < 3.0$.

Figure 5.13.: Relative contribution to the cross section per channel for dijet production at the ATLAS experiment with $\sqrt{s} = 7$ TeV at full color NNLO QCD. The plots were made by Fazila Ahmadova and Daniel Britzger (MPI Munich) for the `APPLfast` collaboration.

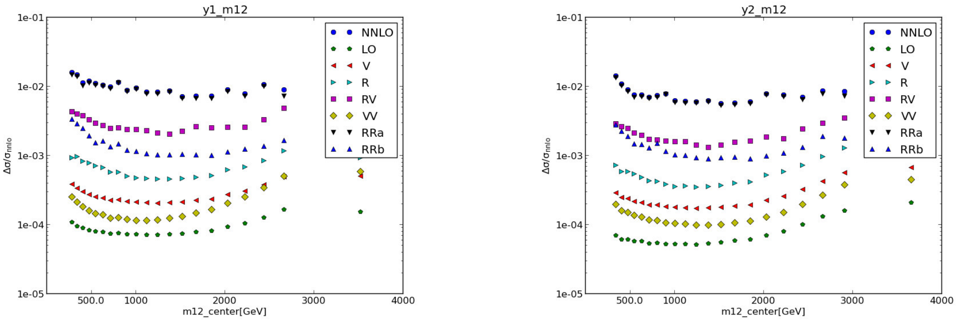

(a) Relative uncertainty per channel, differential in dijet mass m_{12} for $0.0 \leq y^* < 0.5$.

(b) Relative uncertainty per channel, differential in dijet mass m_{12} for $0.5 \leq y^* < 1.0$.

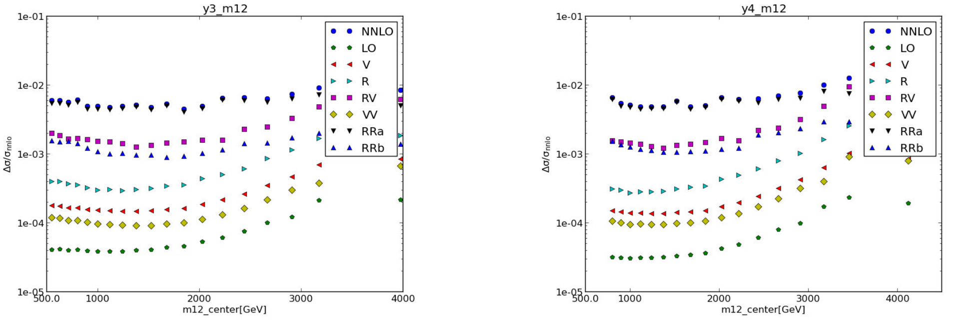

(c) Relative uncertainty per channel, differential in dijet mass m_{12} for $1.0 \leq y^* < 1.5$.

(d) Relative uncertainty per channel, differential in dijet mass m_{12} for $1.5 \leq y^* < 2.0$.

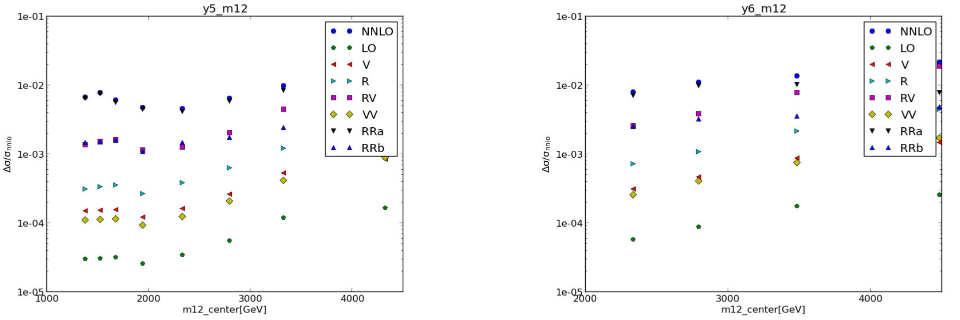

(e) Relative uncertainty per channel, differential in dijet mass m_{12} for $2.0 \leq y^* < 2.5$.

(f) Relative uncertainty per channel, differential in dijet mass m_{12} for $2.5 \leq y^* < 3.0$.

Figure 5.14.: Relative uncertainty contribution per channel for dijet production at the ATLAS experiment with $\sqrt{s} = 7$ TeV at full color NNLO QCD. The plots were made by Fazila Ahmadova and Daniel Britzger (MPI Munich) for the `APPLfast` collaboration.

5.4.4. Fits of the strong coupling constant

As is nicely visible in figure 5.10, the outermost rapidity bins often lead to less precise and more fluctuating fit results than the inner ones. This observation has three main reasons: First, these regions have less and only sparsely distributed MC points, which leads to a larger statistical error. Second, the acceptance of the tracking detector gets worse with high rapidities, meaning that there exists less data in this region to fit. Third and last, highly boosted kinematics (large y_b) correspond to extreme regions of the parton momentum fractions $x_{a,b}$, where one of them is close to zero while the other one is close to one. For such values, the PDFs have the largest uncertainties. In the pursuit of more precise PDF sets, investigations of this boosted sector are worthwhile. However, in a scenario where only the strong coupling shall be determined and no combined fit of the coupling and the PDFs is aimed for, it makes sense to not include such points.

Various choices of rapidity cuts and scenarios were studied, finding that a restriction to only the lowest boosts ($y_b < 1.0$) yields the best outcome. Motivated by the aforementioned reasons, only the results for this variant are shown and further explained here, while others can be found in the appendix, see section A.1. Figure 5.15 shows the χ^2 per degree of freedom (χ^2/ndf) and fitted values of α_s for three different combined data sets and six ways of selecting rapidity bins. In the following, the term 'old data sets' refers to the four first ones listed in the beginning of this section, i.e. CMS 7 TeV and 8 TeV and ATLAS 7 TeV and 13 TeV, which were already part of the discussion in [63], yet back then only at leading color. On the other hand 'new data set' means the CMS 13 TeV data in either its 2D or 3D form. The fits were performed once only for the old sets, once including the new 2D set and once with the new 3D set. Because of this distinction, the rows in table 5.1 are separated the way they are. Said table explains the meaning of the different bins shown in the plots in figure 5.15. The general logic is simple: The upper cut on y^* or $|y|_{\max}$, depending on which of the two is present in each set, is varied between 1.0 and 3.0 (or 2.5 if that is the highest available bin boundary), while y_b is always fixed to be smaller than 1.0. With this choice, the problematic boosted regions with large PDF uncertainties are left out. The results of the fits for each of these bins are summed up in table 5.2.

Among these selection options, the best result is found from the variant with y^* or $|y|_{\max} < 2.0$ and $y_b < 1.0$, including the ATLAS 7 TeV and 13 TeV as well as the CMS 7 TeV, 8 TeV and 13 TeV double differential data sets. This bin is marked orange in table 5.2 and leads to both a small error on the coupling and a low χ^2 of the fit, yielding

$$\alpha_s(m_Z) = 0.1176 \pm 0.0014 \tag{5.24}$$

with χ^2/ndf = 1.03. As a side effect, all results in table 5.2 including this one are in very good agreement with the world average of $\alpha_s(m_Z) = 0.1180 \pm 0.0009$ [90, 91].

Data set	bin 0	bin 1	bin 2	bin 3	bin 4	bin 5
ATLAS 7 TeV (y^*)	< 1.0	< 1.5	< 1.5	< 2.0	< 2.5	< 3.0
CMS 7 TeV ($\lvert y\rvert_{\text{max}}$)	< 1.0	< 1.5	< 1.5	< 2.0	< 2.5	< 2.5
ATLAS 13 TeV (y^*)	< 1.0	< 1.5	< 1.5	< 2.0	< 2.5	< 3.0
CMS 8 TeV (y^*, y_b)	$y^* < 1.0$ $y_b < 1.0$	$y^* < 1.0$ $y_b < 1.0$	$y^* < 2.0$ $y_b < 1.0$	$y^* < 2.0$ $y_b < 1.0$	$y^* < 2.0$ $y_b < 1.0$	$y^* < 3.0$ $y_b < 1.0$
CMS 13 TeV 2D ($\lvert y\rvert_{\text{max}}$)	< 1.0	< 1.5	< 1.5	< 2.0	< 2.5	< 3.0
CMS 13 TeV 3D (y^*, y_b)	$y^* < 1.0$ $y_b < 1.0$	$y^* < 1.5$ $y_b < 1.0$	$y^* < 1.5$ $y_b < 1.0$	$y^* < 2.0$ $y_b < 1.0$	$y^* < 2.5$ $y_b < 1.0$	$y^* < 2.5$ $y_b < 1.0$

Table 5.1.: Table describing the meaning of bins used for the α_s fit. Every next bin relaxes the y^* or $\lvert y\rvert_{\text{max}}$ cut by 0.5, while the y_b cut stays at 1.0. Since the 8 TeV set does not have such fine binning, the steps here are always of size one. The CMS 7 TeV and 13 TeV 3D sets do not contain data for $\lvert y\rvert_{\text{max}} > 2.5$ and $y^* > 2.5$, respectively, so nothing new can be added there in the last bin.

5.5. Conclusion

The need for precise PDF and α_s determinations was explained and a way to provide them based on grid interpolation programs was introduced. The logic and workflow of such programs was described, using `APPLfast` and its interplay with the Monte Carlo event generator `NNLOJET` as an example. The QCD color structure in jet final states was discussed, emphasizing the importance of full color calculations for dijet production.

A new version of `APPLfast` was presented and parts of the validation procedure for it were outlined. Based on ATLAS and CMS measurements of dijet production, full color NNLO QCD calculations have been made and `fastNLO` grids were written; the resulting cross sections were shown for one of the data sets. Finally, these calculations were used for fits of the value of the strong coupling at $\mu_R = m_Z$, giving a nominal fit value of

$$\alpha_s(m_Z) = 0.1176 \pm 0.0014\ . \tag{5.25}$$

This is the first such fit to dijet production data using full color NNLO QCD theory input.

Data set	Bin #	$\alpha_s(m_Z)$		$\Delta\alpha_s(m_Z)$	χ^2/ndf
only old sets	0	0.1170	±	0.0019	0.88
	1	0.1181	±	0.0018	0.89
	2	0.1175	±	0.0018	0.88
	3	0.1170	±	0.0016	0.91
	4	0.1170	±	0.0016	0.90
	5	0.1169	±	0.0016	0.92
with 13 TeV 2D	0	0.1172	±	0.0016	0.95
	1	0.1181	±	0.0015	0.96
	2	0.1178	±	0.0015	0.95
	3	0.1176	±	0.0014	1.03
	4	0.1181	±	0.0013	1.18
	5	0.1180	±	0.0013	1.18
with 13 TeV 3D	0	0.1177	±	0.0015	0.93
	1	0.1178	±	0.0014	0.96
	2	0.1175	±	0.0014	0.95
	3	0.1173	±	0.0013	1.07
	4	0.1179	±	0.0013	1.08
	5	0.1178	±	0.0013	1.09

Table 5.2.: Summary of fit results for the strong coupling constant α_s based on dijet production data from the ATLAS and CMS experiments, combined with full color NNLO QCD calculations performed with `APPLfast`, using the PDF4LHC21 set. The error margin given includes fit, PDF, data and theory uncertainties. As described in the text, different sets of data and cuts on rapidities y^* or $|y|_{\mathrm{max}}$ are shown, whereas highly boosted regions are always excluded, i.e. $y_b < 1.0$ in all bins. For a more detailed explanation of the cuts and content of every bin see table 5.1. The bin chosen as nominal value is highlighted in orange.

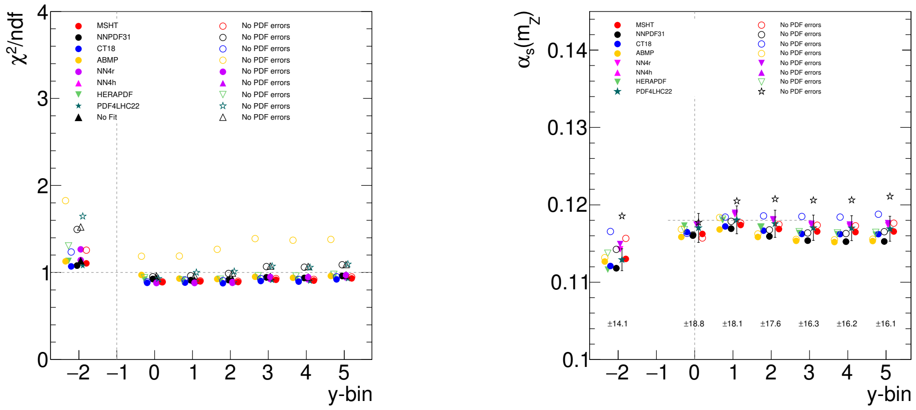

(a) χ^2 per degree of freedom for just the old four data sets.

(b) α_s central values and error margins from fits to only the old four data sets.

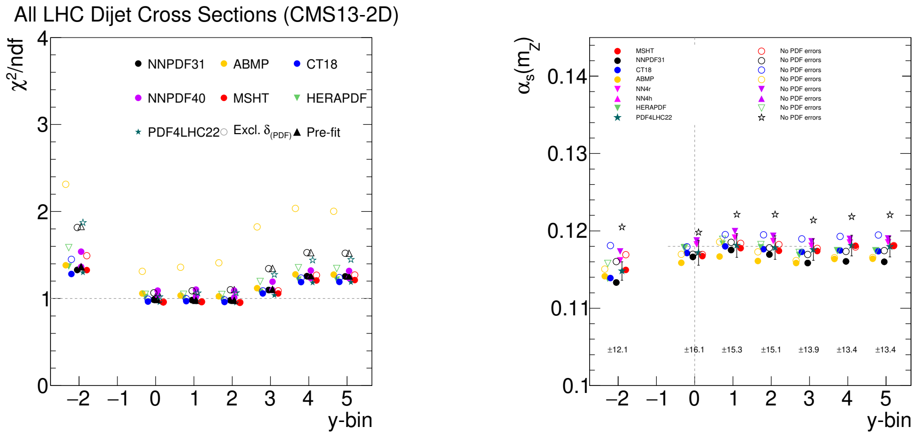

(c) χ^2 per degree of freedom including the CMS 13 TeV 2D data.

(d) α_s central values and error margins including the CMS 13 TeV 2D data.

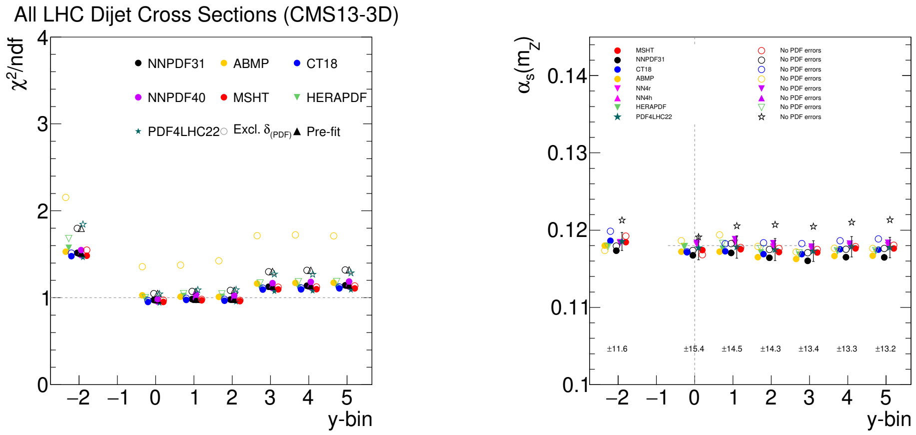

(e) χ^2 per degree of freedom including the CMS 13 TeV 3D data.

(f) α_s central values and error margins including the CMS 13 TeV 3D data.

Figure 5.15.: Fits of the strong coupling using only $y_b < 1.0$ data. The result on the very left in each plot corresponds to the case without any cuts applied, including all y_b values. The definition of the bins is given in table 5.1. The plots were made by Daniel Britzger (MPI Munich) for the `APPLfast` collaboration.

6. Higgs plus Jet Production at NLO QCD in Non-Linear EFT

Since its discovery in 2012 [54, 55], the Higgs boson has been focused on by a plethora of different studies. While many of its properties, like mass [92] and spin [93], are precisely known, other aspects are still unclear or only vaguely estimated. Among those open questions is whether or not the Higgs potential (2.5) is fully SM-like, i.e. whether the mass, VEV, trilinear and quartic couplings have the relation predicted by electroweak symmetry breaking, as described in section 2.3. Other than that remains the question about the precise values of fermion masses and their (Yukawa) couplings to the Higgs boson, the SM approach of which was outlined in section 2.4. Assuming that there might be deviations from said SM description, in this chapter we use non-linear EFT to calculate (differential) cross sections for Higgs plus jet production at next-to-leading order in quantum chromodynamics (QCD). We choose this process for two reasons: First, it is an excellent probe of the top quark Yukawa coupling. From the purely theoretical point of view, $t\bar{t}$ production in association with a Higgs would be a more convenient channel, but is experimentally very challenging due to the high energy threshold of two top and one Higgs masses, $2m_t + m_h \approx 470\,\text{GeV}$, and the large number of final states the tops can decay into. Second, an effective coupling between the Higgs and gluons - a vertex non-existent within the SM - would show sizable effects in this channel. Especially the high transverse momentum region is known to be very interesting in this regard [94–105].

The following study is performed in the framework of non-linear EFT (or EWChL) [34–36, 106–108] as outlined in section 4.2. Given the large mass hierarchy, all quarks except for the top quark are assumed to be massless, such that none of them couple directly to the Higgs. The calculations are mainly done using `POWHEG-BOX-V2` [109–111] in combination with `GoSam` [112, 113], `ninja` [114–116] and `OneLOop` [117], except for the virtual two-loop contributions, which are determined with `Reduze` [118] and `pySecDec` [119–121].

6.1. Chiral Lagrangian for Higgs plus jet production

At the lowest two chiral dimensions, two and four, there is one operator each which contributes to $pp \to hj$. The relevant part of the effective Lagrangian reads

$$\mathcal{L} \supset -m_t c_t \frac{h}{v} \bar{t}t + \frac{\alpha_s}{8\pi} c_g \frac{h}{v} G^a_{\mu\nu} G^{a,\mu\nu} \,. \tag{6.1}$$

The first term comes from $\mathcal{L}_2$, more precisely it is (4.6) with $Y_t^{(1)} = \frac{m_t c_t}{v}$, and can be understood as a rescaling of the top Yukawa coupling. The second term is part of $\mathcal{L}_4$ and results from a loop being integrated out, as depicted in figure 6.1. The case $c_t = 1$

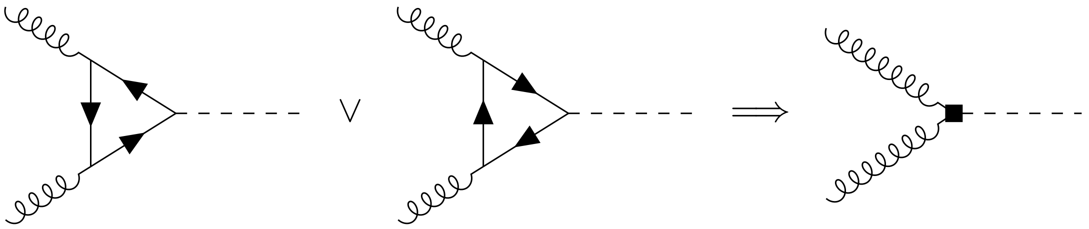

Figure 6.1.: Integrating out a loop particle (in this case a fermion, e.g. the top quark) results in an effective coupling between gluons and a Higgs, indicated by a black square. The case depicted here is the simplest one with only two gluons. Vertices including three or four gluons and a Higgs are also possible, those come from integrated out box or pentagon diagrams. In general the particle in the loop does not have to be from the SM nor must it be fermionic, but could be an arbitrary heavy new resonance.

and $c_g = 0$ corresponds to the SM. In the limit $m_t \to \infty$ the loop process $gg \to h$ can be reduced to a simple tree level diagram with a gluon-gluon-Higgs vertex, exactly as shown in said figure. It can be shown [122] that matching the two coefficients in (6.1) to such a reduction yields $c_t = 0$ and $c_g = \frac{2}{3}$. These are the two opposite extreme cases, all other possible choices lie on or in close vicinity to the straight line between them in parameter space, all approximately fulfilling the condition $c_t + \frac{3}{2}c_g = 1$.

Precise measurements of the inclusive Higgs production cross section [123, 124] suggest that there is no or only a very tiny deviation from the expected SM value. The relation between the EFT and SM values of this observable can be approximated as [97, 125]

$$\sigma_{\text{incl}}^{\text{EFT}} = \left(c_t + \frac{3}{2}c_g\right) \sigma_{\text{incl}}^{\text{SM}} + \mathcal{O}\left(\frac{1}{m_t^2}\right) , \tag{6.2}$$

the experimental constraint thus restricts the bracket on the right hand side to be close to one. Fortunately, even despite this limitation on the EFT parameter space, beyond the SM effects in the high p_T tails of differential distributions can be sizable enough to be experimentally visible [97, 98]. Since LHC experiments have already started to access the high transverse momentum region [126–129] and during the upcoming high luminosity phase of the LHC there will be more data available, precise theory predictions are needed to correctly interpret observations. Previous studies on the matter were either only at leading order [97, 98] or within the heavy top limit [130–132]. This work goes beyond that, aiming for a calculation at NLO QCD accuracy, the outcome of which is discussed in section 6.4. The content of this chapter is a continuation of work presented in [33], the description and results shown here are based on the conventions and logic thereof.

6.2. Higgs production - state of the art

Results for inclusive Higgs boson production are known up to N3LO QCD accuracy within the heavy top limit [133] and at NNLO QCD with the full top mass dependence [56]. Leading order full theory calculations for Higgs plus one jet [134, 135], Higgs plus two jets [136, 137] and Higgs plus three jets [138, 139] have also been published already. Higgs plus one jet fully differential results in the heavy top limit are known at NNLO QCD order [140–143] and are completed by $\frac{1}{m_t}$ expansions for the virtual part [144, 145]. The Higgs plus one jet total cross section and Higgs transverse momentum distribution has been calculated numerically at NLO QCD with full top mass dependence [146]. After all master integrals featuring in the full virtual NLO QCD parts were known [147–150], also an analytic study became available [151]. Electroweak (EW) corrections to Higgs plus one jet are discussed in [148, 152] and studies of mixed QCD-EW effects can be found in [153–155]. SMEFT studies of the Higgs transverse momentum distribution in Higgs plus one jet production including dimension six operators are discussed in [94, 95, 99, 101, 130, 132]. Finally, an investigation of Higgs plus one jet production at NLO QCD in the context of non-linear EFT was started in [33] and is continued in this thesis.

6.3. Next-to-leading order quantum chromodynamics

In order to achieve the precision needed for an experimental search, leading order is not enough, but next-to-leading QCD effects have to be taken into account. We neglect electroweak higher orders because the corresponding coupling is much smaller than g_s and the relevant diagrams are further suppressed by the masses of W and Z bosons appearing in them. The NLO part consists, as introduced in section 3.3, of a virtual component, containing more loops, and a real contribution, describing unresolved additional radiation. `POWHEG` allows to combine these parts and put them together with suitable subtraction and renormalisation terms following the Fixione-Kunszt-Signer (FKS) method [156].

6.3.1. Leading order calculation

At leading order in the EWChL, the process comprises tree level diagrams with an effective gluon-Higgs vertex and one-loop diagrams with a modified top Yukawa coupling. The second of these categories is just the SM amplitude [135] rescaled by c_t, the first can be easily calculated even by hand. As a cross check for these analytical results the same processes have also been generated by `GoSam` using the `UFO` model described in [157], yielding excellent agreement. Up to interchanging of external legs, crossings and inversion of the fermion flow direction in loops there exist six topologies of diagrams, all of which are depicted in figure 6.2. They are arranged such that the rescaled SM diagram and the corresponding pure EFT one are always right above each other.

6.3.2. Real contribution

Just as the leading order part, the real contribution consists of both tree level and one-loop topologies, examples of both of which are shown in figure 6.3. The amplitude squared can thus be expressed as

$$|\mathcal{M}_{\text{real}}|^2 = \left|\mathcal{M}_{\text{one-loop}}\right|^2 + |\mathcal{M}_{\text{tree}}|^2 + 2\,\Re\left(\mathcal{M}^*_{\text{one-loop}}\,\mathcal{M}_{\text{tree}}\right) \; . \tag{6.3}$$

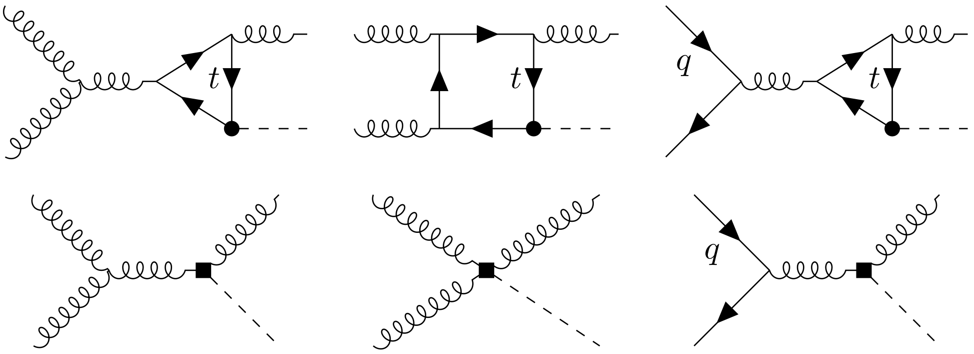

Figure 6.2.: All six topologies of leading order diagrams for Higgs plus one jet production in non-linear EFT at chiral dimension four, which corresponds to one-loop level in the SM. Vertices coming from the first operator in (6.1) are denoted with a black dot, those from the second operator with a black square. In fermion loops only the top quark contributes, since all other quarks are assumed massless. External fermionic states on the other hand are always quarks from the other five generations.

For technical reasons the three components in (6.3) have been generated via two different `GoSam` files, one only containing the modified SM, i.e. $\left|\mathcal{M}_{\text{one-loop}}\right|^2$, and the other one adding the rest. Both results are then combined in `POWHEG`, where also the subtraction of soft and collinear divergences is taken care of. Since for such a $2 \rightarrow 3$ process there exist many problematic phase space regions we had to implement a rescue system to recalculate numerically unstable points at higher (quadruple) precision or discard them if necessary. The numerical quality of a result is checked with respect to its invariance under rotation around the beam axis; if this first check fails, quadruple precision is calculated. For the quadruple result we check whether the $\frac{1}{\varepsilon}$ pole term is zero to good accuracy. Without numerical fluctuations and rounding errors it would be exactly zero since the process is loop-induced in the SM. If this second check also fails the point is discarded.

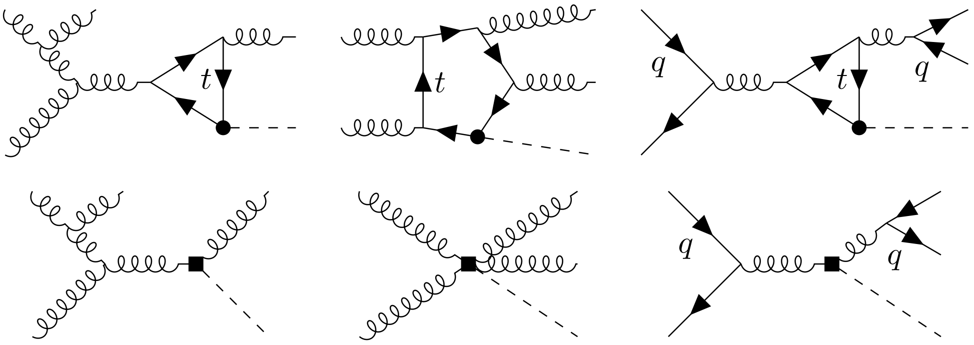

Figure 6.3.: Example diagrams for radiation off an initial state leg (left), off the loop (middle) or off a final state leg (right). Many more topologies are possible: A gluon can be radiated off any - both internal and external - fermion or gluon line and any external gluon can split into a quark-antiquark pair.

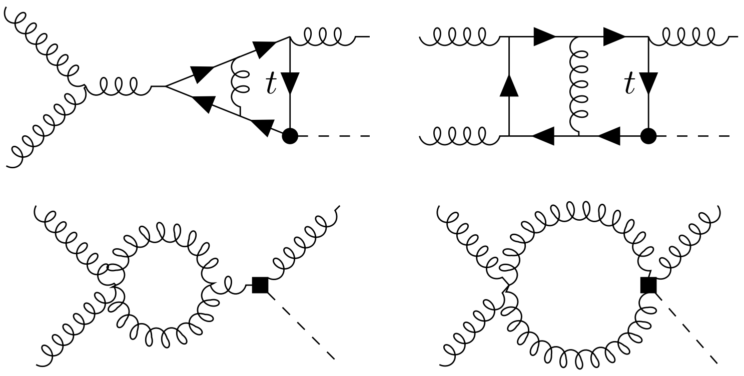

Figure 6.4.: Examples of diagrams contributing to the virtual component, which appear either at one- or two-loop level.

6.3.3. Virtual component

The virtual amplitude consists of the interference of leading order and higher loop diagrams and can be written as

$$\mathcal{M}_{\text{virtual}} = 2\,\mathfrak{R}\left(\mathcal{M}^{*}_{\text{LO}}\,\mathcal{M}_{\text{higher loops}}\right)\ . \tag{6.4}$$

Examples for such higher loop contributions are shown in figure 6.4. There exist two general types: one-loop diagrams with an effective gluon-Higgs coupling and two-loop diagrams with a rescaled top Yukawa. The calculation of the latter part was previously done within the SM [146], using `Reduze` [118] for the reduction to and `pySecDec` [119–121] for the calculation of master integrals. That result can be also used for our EFT, since c_t only appears as a global prefactor and no additional diagrams at two-loop order arise.

The two-loop amplitudes for both the gluonic and fermionic parts can be reduced to scalar form factors. For $g(p_1)g(p_2) \longrightarrow g(p_3)h(p_4)$ this decompisition reads [158]

$$M^{\mu\nu\tau} = F_a T_a^{\mu\nu\tau} + F_b T_b^{\mu\nu\tau} + F_c T_c^{\mu\nu\tau} + F_d T_d^{\mu\nu\tau} \tag{6.5}$$

with the tensor structures

$$\begin{aligned}
T_a^{\mu\nu\tau} &= \left(s_{12} g^{\mu\nu} - 2 p_2^{\mu} p_1^{\nu}\right)\left(s_{23} p_1^{\tau} - s_{13} p_2^{\tau}\right)\frac{1}{2 s_{13}} \\
T_b^{\mu\nu\tau} &= \left(s_{23} g^{\nu\tau} - 2 p_3^{\nu} p_2^{\tau}\right)\left(s_{13} p_2^{\mu} - s_{12} p_3^{\mu}\right)\frac{1}{2 s_{12}} \\
T_c^{\mu\nu\tau} &= \left(s_{13} g^{\tau\mu} - 2 p_1^{\tau} p_3^{\mu}\right)\left(s_{12} p_3^{\nu} - s_{23} p_1^{\nu}\right)\frac{1}{2 s_{23}} \\
T_d^{\mu\nu\tau} &= \left[g^{\mu\nu}\left(s_{23} p_1^{\tau} - s_{13} p_2^{\tau}\right) + g^{\nu\tau}\left(s_{23} p_2^{\mu} - s_{12} p_3^{\mu}\right) + g^{\tau\nu}\left(s_{12} p_3^{\nu} - s_{23} p_1^{\nu}\right)\right. \\
&\qquad \left. + 2\, p_3^{\mu} p_1^{\nu} p_2^{\tau} - 2\, p_2^{\mu} p_3^{\nu} p_1^{\tau}\right]\frac{1}{2}\ ,
\end{aligned} \tag{6.6}$$

where $s_{ij} := \left(p_1 + p_j\right)^2$. The first three of these structures are related to each other by permutations of the gluon momenta. For the quark induced process $q(p_1)\overline{q}(p_2) \longrightarrow g(p_3)h(p_4)$ the decomposition is easier, yielding [159]

$$M^{\rho}\epsilon_{\rho} = F_1 T_1 + F_2 T_2 \tag{6.7}$$

with two tensor structures

$$\begin{aligned} T_1 &= \bar{u}(p_1)\, \not{p}_3\, v(p_2)\ \ (p_2\cdot\epsilon_3) - \bar{u}(p_1)\, \not{\epsilon}_3\, v(p_2)\ \ (p_2\cdot p_3) \\ T_2 &= \bar{u}(p_1)\, \not{p}_3\, v(p_2)\ \ (p_1\cdot\epsilon_3) - \bar{u}(p_1)\, \not{\epsilon}_3\, v(p_2)\ \ (p_1\cdot p_3)\ . \end{aligned} \tag{6.8}$$

The form factors can be calculated applying suitable projectors. For the gluon case these are

$$\begin{aligned} P_a^{\mu\nu\tau} &= \frac{1}{(D-3)\, s_{23}}\left(-\frac{D s_{13}}{s_{12}^2 s_{23}}\, T_a^{\mu\nu\tau} + \frac{D-4}{s_{23}^2}\, T_b^{\mu\nu\tau} + \frac{D-4}{s_{12}s_{13}}\, T_c^{\mu\nu\tau} + \frac{D-2}{s_{12}s_{23}}\, T_d^{\mu\nu\tau}\right) \\ P_b^{\mu\nu\tau} &= \frac{1}{(D-3)\, s_{12}}\left(\frac{D-4}{s_{12}s_{23}}\, T_a^{\mu\nu\tau} - \frac{D s_{12}}{s_{13}s_{23}^2}\, T_b^{\mu\nu\tau} + \frac{D-4}{s_{13}^2}\, T_c^{\mu\nu\tau} + \frac{D-2}{s_{13}s_{23}}\, T_d^{\mu\nu\tau}\right) \\ P_c^{\mu\nu\tau} &= \frac{1}{(D-3)\, s_{13}}\left(\frac{D-4}{s_{12}^2}\, T_a^{\mu\nu\tau} + \frac{D-4}{s_{13}s_{23}}\, T_b^{\mu\nu\tau} - \frac{D s_{23}}{s_{12}s_{13}^2}\, T_c^{\mu\nu\tau} + \frac{D-2}{s_{12}s_{13}}\, T_d^{\mu\nu\tau}\right) \\ P_d^{\mu\nu\tau} &= \frac{D-2}{(D-3)\, s_{12}\, s_{13}\, s_{23}}\left(\frac{s_{13}}{s_{12}}\, T_a^{\mu\nu\tau} + \frac{s_{12}}{s_{23}}\, T_b^{\mu\nu\tau} + \frac{s_{23}}{s_{13}}\, T_c^{\mu\nu\tau} + \frac{D}{D-2}\, T_d^{\mu\nu\tau}\right)\ , \end{aligned}$$

fulfilling $P_{k,\,\mu\nu\tau}\, M^{\mu\nu\tau} = F_k$. For the quark case we use

$$\begin{aligned} P_1 &= \frac{D-2}{2(D-3)s_{12}s_{13}^2} T_1^\dagger - \frac{D-4}{2(D-3)s_{12}s_{13}s_{23}} T_2^\dagger \\ P_2 &= -\frac{D-4}{2(D-3)s_{12}s_{13}s_{23}} T_1^\dagger + \frac{D-2}{2(D-3)s_{12}s_{23}^2} T_2^\dagger\ , \end{aligned}$$

obeying $\sum_{\text{spins}} P_i\, M^\rho \epsilon_\rho = F_i$. The integrals appearing in the two-loop amplitude are calculated numerically, fixing the Higgs mass as $m_h = 125\,\text{GeV}$ and the top mass as $m_t = 173.055\,\text{GeV}$, such that $\frac{m_h^2}{m_t^2} = \frac{12}{23}$, a nice rational number, to very good approximation.

The one-loop diagrams and their interference with leading order can be evaluated with `GoSam` [112, 113], `ninja` [114–116] and `OneLOop` [117], similar to the real radiation.

6.4. Phenomenology

In this section, results for Higgs plus one jet production are shown. The calculation of these were performed within the non-linear EFT framework, using the setup previously described. Based on measurements of the top Yukawa coupling by both the ATLAS and CMS experiments yielding $c_t \approx 0.96 \pm 0.08$ [160] and $c_t \approx 1.01 \pm 0.11$ [161], respectively, and a bound of $c_g \in [-0.301, 0.116]$ from marginalized SMEFT fits [162], a benchmark point ($c_t = 0.9$, $c_g = \frac{2}{30}$) for the EFT scenario was chosen. This point also fulfills the previously mentioned requirement that $c_t + \frac{3}{2}c_g = 1$; the results obtained for it are compared to the Standard Model ($c_t = 1$, $c_g = 0$). As mentioned earlier, the masses are set to $m_t = 173.055\,\text{GeV}$ and $m_h = 125\,\text{GeV}$, while the widths of both particles are assumed to be zero. The PDF set PDF4LHC15_nlo_30_pdfas [163–166] is linked via `LHAPDF` [167, 168], the jets are clustered with the anti-k_T algorithm [74], choosing a cone size of $R = 0.4$.

$p_{T,h}$ cut [GeV]	$\sigma_{\text{cut}}^{\text{EFT}}$ [fb]		$\sigma_{\text{cut}}^{\text{SM}}$ [fb]	
	LO	NLO	LO	NLO
50	$(4.6^{+0.2}_{-0.1}) \cdot 10^3$	$(9.3^{+0.2}_{-1.7}) \cdot 10^3$	$(4.6^{+0.2}_{-0.1}) \cdot 10^3$	$(9.3^{+0.0}_{-1.7}) \cdot 10^3$
100	$(1.4^{+0.6}_{-0.4}) \cdot 10^3$	$(2.84^{+0.04}_{-0.5}) \cdot 10^3$	$(1.4^{+0.6}_{-0.3}) \cdot 10^3$	$(2.88^{+0}_{-0.5}) \cdot 10^3$
200	$(2.2^{+1.0}_{-0.6}) \cdot 10^2$	$(4.6^{+0.2}_{-0.9}) \cdot 10^2$	$(2.2^{+0.9}_{-0.6}) \cdot 10^2$	$(4.6^{+0.1}_{-0.9}) \cdot 10^2$
400	13^{+6}_{-4}	28^{+2}_{-6}	12^{+5}_{-3}	$25^{+1.5}_{-5}$
600	$1.6^{\,0.7}_{-0.5}$	$3.3^{+0.4}_{-0.7}$	$1.3^{+0.6}_{-0.4}$	$2.7^{+0.2}_{-0.5}$
800	$0.28^{+0.13}_{-0.08}$	$0.57^{+0.07}_{-0.11}$	$0.20^{+0.10}_{-0.06}$	$0.41^{+0.04}_{-0.08}$

Table 6.1.: LO and NLO cross sections of the SM ($c_t = 1$, $c_g = 0$) and EFT benchmark point ($c_t = 0.9$, $c_g = \frac{2}{30}$) for various lower cuts on $p_{T,h}$. The uncertainties are obtained from a three-point scale variation. The numbers given in this table can also be found in [169], to which the author of this thesis is one of the contributors.

The central scales are set dynamically to

$$\mu_R = \mu_F = \frac{H_T}{2} = \frac{1}{2}\left(\sqrt{m_h^2 + p_{T,h}^2} + \sum_i p_{T,i}\right) , \tag{6.9}$$

where the sum runs over final state partons, which is just one in the leading order and virtual cases and two for the real radiation. Results for the total cross sections for various lower cuts on the Higgs transverse momentum $p_{T,h}$ are displayed in table 6.1.

The analysis shows that, as expected, there are only very tiny differences between the SM and EFT scenarios at low $p_{T,h}$. However, if the lower cut on this variable is pushed further up and only the tails of the distributions are compared, sizeable differences appear. This effect is even better observed in the ratio of the two results, $\sigma_{\text{cut}}^{\text{EFT}}$ / $\sigma_{\text{cut}}^{\text{SM}}$, which is shown in table 6.2. For $p_{T,h} > 400$ GeV the ratio of cross sections deviates more than 10% from one, which could render it experimentally visible at the HL-LHC or future colliders, even though the absolute values of σ_{cut} in both the SM and EFT are small.

A similar effect can be seen in the differential distribution with respect to $p_{T,h}$, as plotted in figure 6.5. For $p_{T,h} \geq 200$ GeV the two curves diverge from each other, reaching relative differences of 1.2 around 600 GeV and over 1.4 in the outermost bins near 1 TeV. This sizable effect again highlights the importance of studying the high $p_{T,h}$ regime.

$p_{T,h}$ cut [GeV]	$\sigma^{\mathrm{EFT}}_{\mathrm{cut}}$ / $\sigma^{\mathrm{SM}}_{\mathrm{cut}}$	
	LO	NLO
50	0.9966 ± 0.0006	0.99 ± 0.03
100	1.0001 ± 0.0010	0.99 ± 0.04
200	1.021 ± 0.002	1.02 ± 0.02
400	1.118 ± 0.007	1.11 ± 0.01
600	1.251 ± 0.012	1.23 ± 0.01
800	1.407 ± 0.016	1.37 ± 0.02

Table 6.2.: Ratio $\sigma^{\mathrm{EFT}}_{\mathrm{cut}}$ / $\sigma^{\mathrm{SM}}_{\mathrm{cut}}$ of the cross sections for the SM ($c_t = 1$, $c_g = 0$) and an EFT benchmark point ($c_t = 0.9$, $c_g = \frac{2}{30}$) for various lower cuts on the Higgs transverse momentum $p_{T,h}$. The scale uncertainties are correlated between the EFT and SM scenarios and mostly cancel, thus only the numerical uncertainties are shown. The numbers given in this table can also be found in [169], to which the author of this thesis is one of the contributors.

6.5. Conclusion

A calculation of Higgs plus one jet production at chiral dimension four ($d_\chi = 4$) of non-linear EFT with full top mass dependence was presented. The amplitude for this process depends on two effective couplings c_t and c_g, which were chosen such that they fulfill the condition $c_t + \frac{3}{2}c_g = 1$. This choice assures that the cross section for inclusive Higgs production stays within the region allowed by experimental data [123, 124].

The Higgs plus one jet production cross section for both the SM ($c_t = 1$, $c_g = 0$) and a beyond SM benchmark point ($c_t = 0.9$, $c_g = \frac{2}{30}$) was calculated at NLO QCD for various lower cuts on the Higgs transverse momentum. It was shown that, as expected, the results of the two scenarios are very similar at low $p_{T,h}$, but the high $p_{T,h}$ regime allows to spot differences. The EFT cross sections for $p_{T,h} > 400$ GeV show sizable deviations of more than 10% from the Standard Model result not only at LO, but also at NLO. The absolute values of the cross sections in this kinematic region are of the order of a few femtobarn.

Also differential distributions yield interesting results for large values of $p_{T,h}$. In the Higgs transverse momentum spectrum the differences between the EFT benchmark point and the SM reach up to 40% at the upper edge of the studied kinematic range, i.e. at 1 TeV. The divergence between the two graphs is visible already from $p_{T,h} \sim 200$ GeV on. However, there are two caveats: First, the comparably large scale uncertainty bands overlap in most of the calculated histogram bins. Second, these effects will be hard to detect experimentally, since the cross section in each of these bins is less than a femtobarn. The chances to pinpoint new physics in such a differential measurement are therefore comparably small, but nevertheless existent and thus worth the effort.

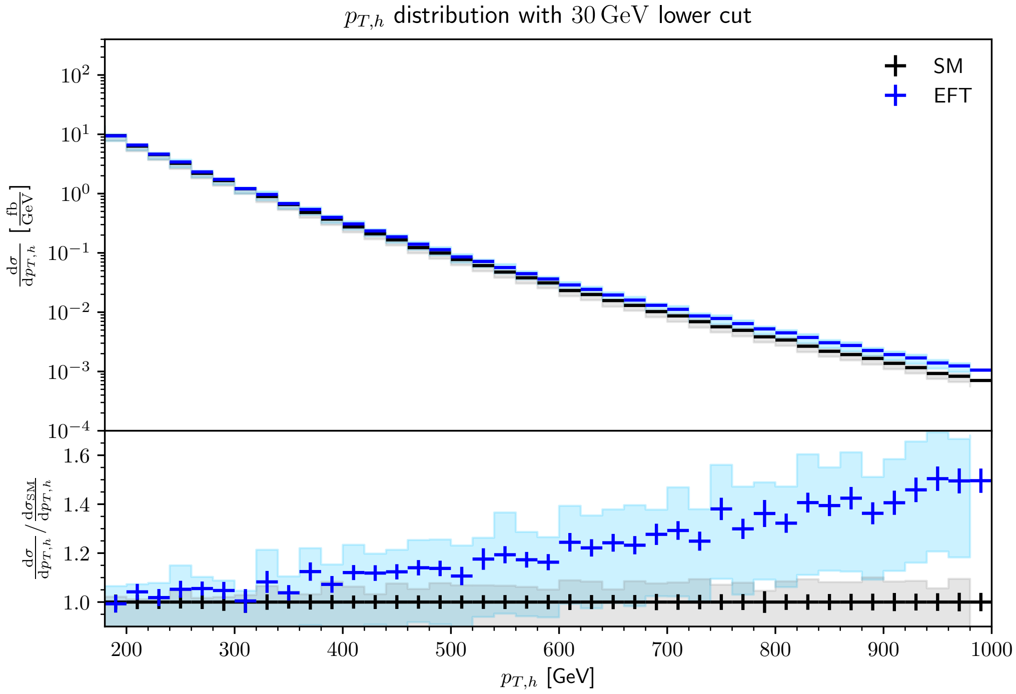

Figure 6.5.: Next-to-leading order cross section differential in Higgs transverse momentum for both the SM ($c_t = 1$, $c_g = 0$) and an EFT benchmark point ($c_t = 0.9$, $c_g = \frac{2}{30}$), including uncertainty bands based on a 3-point scale variation. In the high $p_{T,h}$ regime the difference between the two values becomes large, in the most extreme cases yielding EFT/SM ratios of over 1.4.

7. Conclusion and Outlook

Within the scope of this thesis, two on the first glance disjoint projects have been combined. On the one hand, a new interface between Monte Carlo event generators and grid libraries was developed with the goal to produce more precise and reliable fits of the strong coupling constant. The NNLO QCD dijet production calculations at full color necessary for that were presented in chapter 5 and performed purely within the Standard Model. On the other hand, predictions for Higgs plus one jet production at NLO QCD with full top mass dependence in the context of non-linear Effective Field Theory were calculated in chapter 6, describing effects strictly beyond the Standard Model (BSM). Despite being disconnected, both sides are relevant contributions in the quest for a more complete and profound understanding of nature.

Over the last decades, the Standard Model has been tested to utmost precision by all sorts of experiments. The vast majority of them greatly supports its validity, rendering it widely accepted among particle physicists around the globe. For a plethora of collider observables it gives the most reliable, precise and correct results. For this reason it is important to continue the exploration of its interactions and parameters. Since any process happening at hadron colliders relies on factorisation if it is calculated perturbatively, optimising the ingredients of the factorisation theorem (3.1) is an optimal point to start. To this end, we used the grid interpolation technique to restructure the calculational logic such that it allows for an a posteriori choice of PDF sets and input value of the strong coupling α_s. To be more precise, a new version of the `APPLfast` interface was developed, allowing to use the latest version of `NNLOJET` and thus calculate dijet production at NNLO QCD including the full color structure. Theory predictions matching six distinct LHC (ATLAS and CMS) measurements of the process at different center of mass energies, scale and rapidity choices were produced in the `fastNLO` grid format. As part of this thesis, the grids were used for a determination of the strong coupling at the Z mass, $\alpha_s(m_Z)$, to 1% accuracy. For future work it is planned to make them publicly available, such that they can be used for PDF fits not only by the `APPLfast` collaboration itself, but by any interested PDF fitter working group. Other than that, the newly developed `APPLfast` version will allow for grid production for a large variety of processes with unprecedented efficiency.

Despite being highly accurate and well-tested for some phenomena, there also exist experimental observations lacking explanations within the Standard Model. Very prominent examples for such findings are neutrino masses, the existence of dark matter and dark energy or the abundance of matter over anti-matter. For many of those and other anomalies there exist alternative models which try to analyze and quantify their effects. Often these models introduce new heavy particles beyond the reach of current and previous experiments and search for signs pointing at their existence. Since among all Standard Model particles the Higgs boson was discovered the latest and is the least explored, it is often part of or the portal to new physics models. Another reason the Higgs sector is so popular among model builders is because it is easy to expand and very versatile, due to the scalar nature of the fields involved. A more model independent way to parameterize BSM effects is by the means of effective field theory, which allows to study low energy signatures of high energy new physics without knowing the precise form of the full theory. However, the possibilities of SMEFT are limited by the standard symmetry breaking mechanism of the $SU(2)_L$ gauge group of the SM. On the contrary, the Electroweak Chiral Lagrangian provides exhaustive freedom in the description of the Higgs sector and thus is optimally suited for BSM studies thereof. In this thesis, we performed calculations of Higgs plus one jet production in the EWChL framework at NLO QCD, including the full top mass dependence. For a benchmark point satisfying experimental constraints, cross section values for various cuts on the Higgs transverse momentum were determined and compared to the SM. At leading order it was already known that in the high $p_{T,h}$ region differences between EFT and SM points become comparably large. For our benchmark point with $c_t = 0.9$ and $c_g = \frac{2}{30}$ the same is true at next-to-leading order, which highlights the necessity of more detailed experimental studies of this sector. More precise measurements of the tail of the Higgs transverse momentum distribution could open a window to explore the signatures of possible yet undiscovered heavy color-charged particles. In this regard the high luminosity phase of the LHC will be both enlightening and exiting.

To conclude this work let us recall the statement it started with: "There is nothing new to be discovered in physics now. All that remains is more and more precise measurement." Now that after the Higgs discovery the Standard Model is complete, some might say a similar thing. But as much as the striving for more precise measurements and calculations is necessary and important, it is once again not the only research direction remaining. In the era of not only the HL-LHC and future colliders like the FCC or CLIC, but also new neutrino and dark matter experiments, many interesting and puzzling observations are to be expected. We hope that the work done, the results achieved and the code developed within the scope of this thesis will help to better interpret and understand them.

List of Figures

List of Tables

Bibliography

1. Edelhäuser, L. & Knochel, A. *Tutorium Quantenfeldtheorie* ISBN: 978-3-642-37676-4 (Springer Spektrum, 2016).
2. Schwartz, M. D. *Quantum Field Theory and the Standard Model* ISBN: 978-1-107-03473-0 (Cambridge University Press, Mar. 2014).
3. Peskin, M. E. & Schroeder, D. V. *An Introduction to quantum field theory* ISBN: 978-0-201-50397-5 (Addison-Wesley, Reading, USA, 1995).
4. Romao, J. C. & Silva, J. P. A resource for signs and Feynman diagrams of the Standard Model. *Int. J. Mod. Phys. A* **27,** 1230025. arXiv: `1209.6213 [hep-ph]` (2012).
5. Lubej, M. *Standard Model* Apr. 2015. `https://www.physik.uzh.ch/groups/serra/StandardModel.html`.
6. Englert, F. & Brout, R. Broken Symmetry and the Mass of Gauge Vector Mesons. *Phys. Rev. Lett.* **13** (ed Taylor, J. C.) 321–323 (1964).
7. Higgs, P. W. Broken symmetries, massless particles and gauge fields. *Phys. Lett.* **12,** 132–133 (1964).
8. Higgs, P. W. Broken Symmetries and the Masses of Gauge Bosons. *Phys. Rev. Lett.* **13** (ed Taylor, J. C.) 508–509 (1964).
9. Higgs, P. W. Spontaneous Symmetry Breakdown without Massless Bosons. *Phys. Rev.* **145,** 1156–1163 (1966).
10. Goldstone, J., Salam, A. & Weinberg, S. Broken Symmetries. *Phys. Rev.* **127,** 965–970 (1962).
11. Higgs, P. W. Broken Symmetries and the Masses of Gauge Bosons. *Phys. Rev. Lett.* **13** (ed Taylor, J. C.) 508–509 (1964).
12. Higgs, P. W. Broken symmetries, massless particles and gauge fields. *Phys. Lett.* **12,** 132–133 (1964).
13. Kibble, T. W. B. Symmetry breaking in nonAbelian gauge theories. *Phys. Rev.* **155** (ed Taylor, J. C.) 1554–1561 (1967).
14. Kibble, T. W. B. The goldstone theorem. *Conf. Proc. C* **670828,** 277–304 (1967).
15. Salam, A. & Ward, J. C. Weak and electromagnetic interactions. *Nuovo Cim.* **11,** 568–577 (1959).
16. Glashow, S. L. Partial Symmetries of Weak Interactions. *Nucl. Phys.* **22,** 579–588 (1961).
17. Gribov, V. N. & Lipatov, L. N. e+ e- pair annihilation and deep inelastic e p scattering in perturbation theory. *Sov. J. Nucl. Phys.* **15,** 675–684 (1972).

18. Dokshitzer, Y. L. Calculation of the Structure Functions for Deep Inelastic Scattering and e+ e- Annihilation by Perturbation Theory in Quantum Chromodynamics. *Sov. Phys. JETP* **46,** 641–653 (1977).
19. Altarelli, G. & Parisi, G. Asymptotic Freedom in Parton Language. *Nucl. Phys. B* **126,** 298–318 (1977).
20. 't Hooft, G. & Veltman, M. J. G. Regularization and Renormalization of Gauge Fields. *Nucl. Phys. B* **44,** 189–213 (1972).
21. 't Hooft, G. & Veltman, M. J. G. Scalar One Loop Integrals. *Nucl. Phys. B* **153,** 365–401 (1979).
22. Kinoshita, T. Mass singularities of Feynman amplitudes. *J. Math. Phys.* **3,** 650–677 (1962).
23. Lee, T. D. & Nauenberg, M. Degenerate Systems and Mass Singularities. *Phys. Rev.* **133** (ed Feinberg, G.) B1549–B1562 (1964).
24. Politzer, H. D. Reliable Perturbative Results for Strong Interactions? *Phys. Rev. Lett.* **30** (ed Taylor, J. C.) 1346–1349 (1973).
25. Gross, D. J. & Wilczek, F. Asymptotically Free Gauge Theories - I. *Phys. Rev. D* **8,** 3633–3652 (1973).
26. Patrignani, C. Review of Particle Physics. *Chinese Physics C* **40,** 100001. `https://dx.doi.org/10.1088/1674-1137/40/10/100001` (Oct. 2016).
27. Deur, A., Brodsky, S. J. & de Téramond, G. F. The QCD running coupling. *Progress in Particle and Nuclear Physics* **90,** 1–74. ISSN: 0146-6410. `https://www.sciencedirect.com/science/article/pii/S0146641016300035` (2016).
28. Berthier, L. & Trott, M. Towards consistent Electroweak Precision Data constraints in the SMEFT. *Journal of High Energy Physics* **2015.** ISSN: 1029-8479. `http://dx.doi.org/10.1007/JHEP05(2015)024` (May 2015).
29. Ellis, J., Murphy, C. W., Sanz, V. & You, T. Updated global SMEFT fit to Higgs, diboson and electroweak data. *Journal of High Energy Physics* **2018.** ISSN: 1029-8479. `http://dx.doi.org/10.1007/JHEP06(2018)146` (June 2018).
30. Weinberg, S. Baryon and Lepton Nonconserving Processes. *Phys. Rev. Lett.* **43,** 1566–1570 (1979).
31. De Gouvêa, A., Herrero-García, J. & Kobach, A. Neutrino masses, grand unification, and baryon number violation. *Physical Review D* **90.** ISSN: 1550-2368. `http://dx.doi.org/10.1103/PhysRevD.90.016011` (July 2014).
32. Grzadkowski, B., Iskrzynski, M., Misiak, M. & Rosiek, J. Dimension-Six Terms in the Standard Model Lagrangian. *JHEP* **10,** 085. arXiv: `1008.4884 [hep-ph]` (2010).
33. Capozi, M. *Precision calculations in the Higgs sector within and beyond the Standard Model* (Mar. 2020). `http://nbn-resolving.de/urn:nbn:de:bvb:19-268260`.
34. FERUGLIO, F. THE CHIRAL APPROACH TO THE ELECTROWEAK INTERACTIONS. *International Journal of Modern Physics A* **08,** 4937–4972. ISSN: 1793-656X. `http://dx.doi.org/10.1142/S0217751X93001946` (Nov. 1993).

35. Alonso, R., Gavela, M., Merlo, L., Rigolin, S. & Yepes, J. The effective chiral Lagrangian for a light dynamical "Higgs particle". *Physics Letters B* **722,** 330–335. ISSN: 0370-2693. `http://dx.doi.org/10.1016/j.physletb.2013.04.037` (May 2013).

36. Buchalla, G., Catà, O. & Krause, C. Complete electroweak chiral Lagrangian with a light Higgs at NLO. *Nuclear Physics B* **880,** 552–573. ISSN: 0550-3213. `http://dx.doi.org/10.1016/j.nuclphysb.2014.01.018` (Mar. 2014).

37. Buchalla, G., Catà, O., Celis, A., Knecht, M. & Krause, C. Complete one-loop renormalization of the Higgs-electroweak chiral Lagrangian. *Nuclear Physics B* **928,** 93–106. ISSN: 0550-3213. `http://dx.doi.org/10.1016/j.nuclphysb.2018.01.009` (Mar. 2018).

38. Buchalla, G., Catà, O., Celis, A. & Krause, C. Fitting Higgs data with nonlinear effective theory. *The European Physical Journal C* **76.** ISSN: 1434-6052. `http://dx.doi.org/10.1140/epjc/s10052-016-4086-9` (Apr. 2016).

39. De Blas, J., Eberhardt, O. & Krause, C. Current and future constraints on Higgs couplings in the nonlinear Effective Theory. *Journal of High Energy Physics* **2018.** ISSN: 1029-8479. `http://dx.doi.org/10.1007/JHEP07(2018)048` (July 2018).

40. Buchalla, G., Catà, O., Celis, A. & Krause, C. Note on anomalous Higgs-boson couplings in effective field theory. *Physics Letters B* **750,** 298–301. ISSN: 0370-2693. `http://dx.doi.org/10.1016/j.physletb.2015.09.027` (Nov. 2015).

41. Buchalla, G., Catà, O. & Krause, C. On the power counting in effective field theories. *Physics Letters B* **731,** 80–86. ISSN: 0370-2693. `http://dx.doi.org/10.1016/j.physletb.2014.02.015` (Apr. 2014).

42. Harrison, M., Ludlam, T. & Ozaki, S. RHIC project overview. *Nucl. Instrum. Meth. A* **499,** 235–244 (2003).

43. Adcox, K. *et al.* Formation of dense partonic matter in relativistic nucleus-nucleus collisions at RHIC: Experimental evaluation by the PHENIX collaboration. *Nucl. Phys. A* **757,** 184–283. arXiv: `nucl-ex/0410003` (2005).

44. Adams, J. *et al.* Experimental and theoretical challenges in the search for the quark gluon plasma: The STAR Collaboration's critical assessment of the evidence from RHIC collisions. *Nucl. Phys. A* **757,** 102–183. arXiv: `nucl-ex/0501009` (2005).

45. Gyulassy, M. & McLerran, L. New forms of QCD matter discovered at RHIC. *Nucl. Phys. A* **750** (eds Rischke, D. & Levin, G.) 30–63. arXiv: `nucl-th/0405013` (2005).

46. Abe, T. *et al. Belle II Technical Design Report* 2010. arXiv: `1011.0352 [physics.ins-det]`.

47. Bevan, A. J. *et al.* The Physics of the B Factories. *The European Physical Journal C* **74.** ISSN: 1434-6052. `http://dx.doi.org/10.1140/epjc/s10052-014-3026-9` (Nov. 2014).

48. LHC Machine. *JINST* **3** (eds Evans, L. & Bryant, P.) S08001 (2008).

49. Myers, S. & Picasso, E. The design, construction and commissioning of the CERN large Electron–Positron collider. *Contemporary Physics* **31,** 387–403 (1990).

50. Aamodt, K. *et al.* The ALICE experiment at the CERN LHC. *JINST* **3,** S08002 (2008).

51. Aad, G. *et al.* The ATLAS Experiment at the CERN Large Hadron Collider. *JINST* **3,** S08003 (2008).
52. Chatrchyan, S. *et al.* The CMS Experiment at the CERN LHC. *JINST* **3,** S08004 (2008).
53. Alves Jr., A. A. *et al.* The LHCb Detector at the LHC. *JINST* **3,** S08005 (2008).
54. Aad, G. *et al.* Observation of a new particle in the search for the Standard Model Higgs boson with the ATLAS detector at the LHC. *Phys. Lett. B* **716,** 1–29. arXiv: `1207.7214 [hep-ex]` (2012).
55. Chatrchyan, S. *et al.* Observation of a New Boson at a Mass of 125 GeV with the CMS Experiment at the LHC. *Phys. Lett. B* **716,** 30–61. arXiv: `1207.7235 [hep-ex]` (2012).
56. Czakon, M., Harlander, R. V., Klappert, J. & Niggetiedt, M. Exact Top-Quark Mass Dependence in Hadronic Higgs Production. *Phys. Rev. Lett.* **127.** [Erratum: Phys.Rev.Lett. 131, 179901 (2023)], 162002. arXiv: `2105.04436 [hep-ph]` (2021).
57. Dulat, F., Lazopoulos, A. & Mistlberger, B. iHixs 2 — Inclusive Higgs cross sections. *Comput. Phys. Commun.* **233,** 243–260. arXiv: `1802.00827 [hep-ph]` (2018).
58. Cepeda, M. *et al.* Report from Working Group 2: Higgs Physics at the HL-LHC and HE-LHC. *CERN Yellow Rep. Monogr.* **7** (eds Dainese, A. *et al.*) 221–584. arXiv: `1902.00134 [hep-ph]` (2019).
59. Carli, T. *et al.* A posteriori inclusion of parton density functions in NLO QCD final-state calculations at hadron colliders: The APPLGRID Project. *Eur. Phys. J. C* **66,** 503–524. arXiv: `0911.2985 [hep-ph]` (2010).
60. Kluge, T., Rabbertz, K. & Wobisch, M. *FastNLO: Fast pQCD calculations for PDF fits* in *14th International Workshop on Deep Inelastic Scattering* (Sept. 2006), 483–486. arXiv: `hep-ph/0609285`.
61. Britzger, D., Rabbertz, K., Stober, F. & Wobisch, M. *New features in version 2 of the fastNLO project* in *20th International Workshop on Deep-Inelastic Scattering and Related Subjects* (2012), 217–221. arXiv: `1208.3641 [hep-ph]`.
62. Britzger, D. *et al.* Calculations for deep inelastic scattering using fast interpolation grid techniques at NNLO in QCD and the extraction of α_s from HERA data. *Eur. Phys. J. C* **79.** [Erratum: Eur.Phys.J.C 81, 957 (2021)], 845. arXiv: `1906.05303 [hep-ph]` (2019).
63. Britzger, D. *et al.* NNLO interpolation grids for jet production at the LHC. *Eur. Phys. J. C* **82,** 930. arXiv: `2207.13735 [hep-ph]` (2022).
64. Bierlich, C. *et al. A comprehensive guide to the physics and usage of PYTHIA 8.3* 2022. arXiv: `2203.11601 [hep-ph]`. `https://arxiv.org/abs/2203.11601`.
65. Bähr, M. *et al.* Herwig++ physics and manual. *The European Physical Journal C* **58,** 639–707. ISSN: 1434-6052. `http://dx.doi.org/10.1140/epjc/s10052-008-0798-9` (Nov. 2008).
66. Bellm, J. *et al.* Herwig 7.0/Herwig++ 3.0 release note. *Eur. Phys. J. C* **76,** 196. arXiv: `1512.01178 [hep-ph]` (2016).

67. Gehrmann, T. *et al.* Jet cross sections and transverse momentum distributions with NNLOJET. *PoS* **RADCOR2017** (eds Hoang, A. & Schneider, C.) 074. arXiv: `1801.06415 [hep-ph]` (2018).
68. Gauld, R., Glover, N., Huss, A., Majer, I. & Gehrmann-De Ridder, A. LHC observables with NNLOJET. *PoS* **RADCOR2019,** 002 (2019).
69. *The Large Hadron Collider: Harvest of Run 1* (ed Schörner-Sadenius, T.) (Springer, Berlin, 2015).
70. Rabbertz, K. *Jet Physics at the LHC: The Strong Force beyond the TeV Scale* (Springer, Berlin, 2017).
71. Ellis, S. D. & Soper, D. E. Successive combination jet algorithm for hadron collisions. *Physical Review D* **48,** 3160–3166. ISSN: 0556-2821. `http://dx.doi.org/10.1103/PhysRevD.48.3160` (Oct. 1993).
72. Dokshitzer, Y., Leder, G., Moretti, S. & Webber, B. Better jet clustering algorithms. *Journal of High Energy Physics* **1997,** 001–001. ISSN: 1029-8479. `http://dx.doi.org/10.1088/1126-6708/1997/08/001` (Aug. 1997).
73. Wobisch, M. & Wengler, T. *Hadronization Corrections to Jet Cross Sections in Deep-Inelastic Scattering* 1999. arXiv: `hep-ph/9907280 [hep-ph]`.
74. Cacciari, M., Salam, G. P. & Soyez, G. The anti-ktjet clustering algorithm. *Journal of High Energy Physics* **2008,** 063–063. ISSN: 1029-8479. `http://dx.doi.org/10.1088/1126-6708/2008/04/063` (Apr. 2008).
75. CMS Collaboration. Measurement of the triple-differential dijet cross section in proton-proton collisions at $\sqrt{s} = 8\,\mathrm{TeV}$ and constraints on parton distribution functions. *The European Physical Journal C* **77.** ISSN: 1434-6052. `http://dx.doi.org/10.1140/epjc/s10052-017-5286-7` (Nov. 2017).
76. CMS Collaboration. Measurements of Differential Jet Cross Sections in Proton-Proton Collisions at $\sqrt{s}$ = 7 TeV with the CMS Detector. *Phys. Rev. D* **87.** [Erratum: Phys.Rev.D 87, 119902 (2013)], 112002. arXiv: `1212.6660 [hep-ex]` (2013).
77. CMS Collaboration. Measurement of the triple-differential dijet cross section in proton-proton collisions at $\sqrt{s} = 8\,\mathrm{TeV}$ and constraints on parton distribution functions. *Eur. Phys. J. C* **77,** 746. arXiv: `1705.02628 [hep-ex]` (2017).
78. ATLAS Collaboration. Measurement of dijet cross-sections in pp collisions at 7 TeV centre-of-mass energy using the ATLAS detector. *Journal of High Energy Physics* **2014.** ISSN: 1029-8479. `http://dx.doi.org/10.1007/JHEP05(2014)059` (May 2014).
79. ATLAS Collaboration. Measurement of inclusive jet and dijet cross-sections in proton-proton collisions at $\sqrt{s}$ = 13 TeV with the ATLAS detector. *JHEP* **05,** 195. arXiv: `1711.02692 [hep-ex]` (2018).
80. Ellis, S. D., Kunszt, Z. & Soper, D. E. Two jet production in hadron collisions at order α_s^3 in QCD. *Phys. Rev. Lett.* **69,** 1496–1499 (1992).
81. Hayrapetyan, Aram and others. Measurement of multidifferential cross sections for dijet production in proton-proton collisions at $\sqrt{s}$ = 13 TeV. arXiv: `2312.16669 [hep-ex]` (Dec. 2023).

82. Currie, J., Glover, E. W. N. & Pires, J. Next-to-Next-to Leading Order QCD Predictions for Single Jet Inclusive Production at the LHC. *Physical Review Letters* **118.** ISSN: 1079-7114. `http://dx.doi.org/10.1103/PhysRevLett.118.072002` (Feb. 2017).

83. Currie, J. *et al.* Precise Predictions for Dijet Production at the LHC. *Physical Review Letters* **119.** ISSN: 1079-7114. `http://dx.doi.org/10.1103/PhysRevLett.119.152001` (Oct. 2017).

84. Currie, J. *et al. Jet cross sections at the LHC with NNLOJET* 2018. arXiv: `1807.06057 [hep-ph]`.

85. Ridder, A. G.-D., Gehrmann, T., Glover, E. W. N., Huss, A. & Pires, J. Triple Differential Dijet Cross Section at the LHC. *Physical Review Letters* **123.** ISSN: 1079-7114. `http://dx.doi.org/10.1103/PhysRevLett.123.102001` (Sept. 2019).

86. Czakon, M., van Hameren, A., Mitov, A. & Poncelet, R. Single-jet inclusive rates with exact color at $O(\alpha_s^4)$. *JHEP* **10,** 262. arXiv: `1907.12911 [hep-ph]` (2019).

87. Chen, X. and Gehrmann, T. and Glover, E. W. N. and Mo, J. Antenna subtraction for jet production observables in full colour at NNLO. *JHEP* **10,** 040. arXiv: `2208.02115 [hep-ph]` (2022).

88. Chen, X., Gehrmann, T., Glover, E. W. N., Huss, A. & Marcoli, M. Automation of antenna subtraction in colour space: gluonic processes. *JHEP* **10,** 099. arXiv: `2203.13531 [hep-ph]` (2022).

89. Chen, X., Gehrmann, T., Glover, E. W. N., Huss, A. & Mo, J. NNLO QCD corrections in full colour for jet production observables at the LHC. *JHEP* **09,** 025. arXiv: `2204.10173 [hep-ph]` (2022).

90. Workman, R. L. *et al.* Review of Particle Physics. *PTEP* **2022,** 083C01 (2022).

91. Huston, J., Rabbertz, K. & Zanderighi, G. Quantum Chromodynamics. arXiv: `2312.14015 [hep-ph]` (Dec. 2023).

92. Chatrchyan, S. *et al.* Observation of a New Boson with Mass Near 125 GeV in pp Collisions at $\sqrt{s} = 7$ and 8 TeV. *JHEP* **06,** 081. arXiv: `1303.4571 [hep-ex]` (2013).

93. Properties of the Higgs-like boson in the decay H to ZZ to 4l in pp collisions at sqrt s =7 and 8 TeV (Mar. 2013).

94. Harlander, R. V. & Neumann, T. Probing the nature of the Higgs-gluon coupling. *Physical Review D* **88.** ISSN: 1550-2368. `http://dx.doi.org/10.1103/PhysRevD.88.074015` (Oct. 2013).

95. Azatov, A. & Paul, A. Probing Higgs couplings with high p_T Higgs production. *Journal of High Energy Physics* **2014.** ISSN: 1029-8479. `http://dx.doi.org/10.1007/JHEP01(2014)014` (Jan. 2014).

96. Banfi, A., Martin, A. & Sanz, V. Probing top-partners in Higgs+jets. *JHEP* **08,** 053. arXiv: `1308.4771 [hep-ph]` (2014).

97. Grojean, C., Salvioni, E., Schlaffer, M. & Weiler, A. Very boosted Higgs in gluon fusion. *Journal of High Energy Physics* **2014.** ISSN: 1029-8479. `http://dx.doi.org/10.1007/JHEP05(2014)022` (May 2014).

98. Schlaffer, M., Spannowsky, M., Takeuchi, M., Weiler, A. & Wymant, C. Boosted Higgs shapes. *The European Physical Journal C* **74.** ISSN: 1434-6052. `http://dx.doi.org/10.1140/epjc/s10052-014-3120-z` (Oct. 2014).
99. Dawson, S., Lewis, I. M. & Zeng, M. Effective field theory for Higgs boson plus jet production. *Physical Review D* **90.** ISSN: 1550-2368. `http://dx.doi.org/10.1103/PhysRevD.90.093007` (Nov. 2014).
100. Buschmann, M. *et al.* Mass Effects in the Higgs-Gluon Coupling: Boosted vs Off-Shell Production. *JHEP* **02,** 038. arXiv: `1410.5806 [hep-ph]` (2015).
101. Langenegger, U., Spira, M. & Strebel, I. *Testing the Higgs Boson Coupling to Gluons* 2015. arXiv: `1507.01373 [hep-ph]`.
102. Azatov, A., Grojean, C., Paul, A. & Salvioni, E. Resolving gluon fusion loops at current and future hadron colliders. *JHEP* **09,** 123. arXiv: `1608.00977 [hep-ph]` (2016).
103. Lindert, J. M., Kudashkin, K., Melnikov, K. & Wever, C. Higgs bosons with large transverse momentum at the LHC. *Phys. Lett.* **B782,** 210–214. arXiv: `1801.08226 [hep-ph]` (2018).
104. Sirunyan, A. M. *et al.* Measurement and interpretation of differential cross sections for Higgs boson production at $\sqrt{s} = 13$ TeV. *Phys. Lett.* **B792,** 369–396. arXiv: `1812.06504 [hep-ex]` (2019).
105. Aaboud, M. *et al.* Measurements of Higgs boson properties in the diphoton decay channel with 36 fb^{-1} of pp collision data at $\sqrt{s} = 13$ TeV with the ATLAS detector. *Phys. Rev.* **D98,** 052005. arXiv: `1802.04146 [hep-ex]` (2018).
106. Burgess, C. P., Matias, J. & Pospelov, M. A Higgs or not a Higgs? What to do if you discover a new scalar particle. *Int. J. Mod. Phys. A* **17,** 1841–1918. arXiv: `hep-ph/9912459` (2002).
107. Grinstein, B. & Trott, M. A Higgs-Higgs bound state due to new physics at a TeV. *Phys. Rev. D* **76,** 073002. arXiv: `0704.1505 [hep-ph]` (2007).
108. Contino, R., Grojean, C., Moretti, M., Piccinini, F. & Rattazzi, R. Strong Double Higgs Production at the LHC. *JHEP* **05,** 089. arXiv: `1002.1011 [hep-ph]` (2010).
109. Nason, P. A New method for combining NLO QCD with shower Monte Carlo algorithms. *JHEP* **11,** 040. arXiv: `hep-ph/0409146` (2004).
110. Frixione, S., Nason, P. & Oleari, C. Matching NLO QCD computations with Parton Shower simulations: the POWHEG method. *JHEP* **11,** 070. arXiv: `0709.2092 [hep-ph]` (2007).
111. Alioli, S., Nason, P., Oleari, C. & Re, E. A general framework for implementing NLO calculations in shower Monte Carlo programs: the POWHEG BOX. *JHEP* **06,** 043. arXiv: `1002.2581 [hep-ph]` (2010).
112. Cullen, G. *et al.* Automated one-loop calculations with GoSam. *The European Physical Journal C* **72.** ISSN: 1434-6052. `http://dx.doi.org/10.1140/epjc/s10052-012-1889-1` (Mar. 2012).

113. Cullen, G. *et al.* GoSam-2.0: a tool for automated one-loop calculations within the Standard Model and beyond. *The European Physical Journal C* **74.** ISSN: 1434-6052. `http://dx.doi.org/10.1140/epjc/s10052-014-3001-5` (Aug. 2014).

114. Mastrolia, P., Mirabella, E. & Peraro, T. Integrand reduction of one-loop scattering amplitudes through Laurent series expansion. *Journal of High Energy Physics* **2012.** ISSN: 1029-8479. `http://dx.doi.org/10.1007/JHEP06(2012)095` (June 2012).

115. Van Deurzen, H. *et al.* Multi-leg one-loop massive amplitudes from integrand reduction via Laurent expansion. *Journal of High Energy Physics* **2014.** ISSN: 1029-8479. `http://dx.doi.org/10.1007/JHEP03(2014)115` (Mar. 2014).

116. Peraro, T. Ninja: Automated integrand reduction via Laurent expansion for one-loop amplitudes. *Computer Physics Communications* **185,** 2771–2797. ISSN: 0010-4655. `http://dx.doi.org/10.1016/j.cpc.2014.06.017` (Oct. 2014).

117. Van Hameren, A. OneLOop: For the evaluation of one-loop scalar functions. *Computer Physics Communications* **182,** 2427–2438. ISSN: 0010-4655. `http://dx.doi.org/10.1016/j.cpc.2011.06.011` (Nov. 2011).

118. Von Manteuffel, A. & Studerus, C. Reduze 2 - Distributed Feynman Integral Reduction. arXiv: `1201.4330 [hep-ph]` (2012).

119. Borowka, S. *et al.* pySecDec: a toolbox for the numerical evaluation of multi-scale integrals. *Comput. Phys. Commun.* **222,** 313–326. arXiv: `1703.09692 [hep-ph]` (2018).

120. Heinrich, G. *et al.* Expansion by regions with pySecDec. *Comput. Phys. Commun.* **273,** 108267. arXiv: `2108.10807 [hep-ph]` (2022).

121. Heinrich, G. *et al.* Numerical scattering amplitudes with pySecDec. *Comput. Phys. Commun.* **295,** 108956. arXiv: `2305.19768 [hep-ph]` (2024).

122. Heinrich, G. *Precision Phenomenology at Colliders and Computational Methods* July 2021.

123. Sirunyan, A. M. *et al.* Measurement of inclusive and differential Higgs boson production cross sections in the diphoton decay channel in proton-proton collisions at $\sqrt{s}$ = 13 TeV. *JHEP* **01,** 183. arXiv: `1807.03825 [hep-ex]` (2019).

124. Aad, G. *et al.* Combined measurements of Higgs boson production and decay using up to 80 fb^{-1} of proton-proton collision data at $\sqrt{s}$ = 13 TeV collected with the ATLAS experiment. *Phys. Rev. D* **101,** 012002. arXiv: `1909.02845 [hep-ex]` (2020).

125. Shifman, M. A., Vainshtein, A. I., Voloshin, M. B. & Zakharov, V. I. Low-Energy Theorems for Higgs Boson Couplings to Photons. *Sov. J. Nucl. Phys.* **30,** 711–716 (1979).

126. Hayrapetyan, A. *et al.* Measurement of the Production Cross Section of a Higgs Boson with Large Transverse Momentum in Its Decays to a Pair of τ Leptons in Proton-Proton Collisions at $\sqrt{s}$ = 13 TeV. arXiv: `2403.20201 [hep-ex]` (Mar. 2024).

127. Sirunyan, A. M. *et al.* Inclusive search for highly boosted Higgs bosons decaying to bottom quark-antiquark pairs in proton-proton collisions at $\sqrt{s}$ = 13 TeV. *JHEP* **12,** 085. arXiv: `2006.13251 [hep-ex]` (2020).

128. Aad, G. *et al.* Identification of boosted Higgs bosons decaying into *b*-quark pairs with the ATLAS detector at 13 TeV. *Eur. Phys. J. C* **79,** 836. arXiv: `1906.11005 [hep-ex]` (2019).

129. Aad, G. *et al.* Study of High-Transverse-Momentum Higgs Boson Production in Association with a Vector Boson in the qqbb Final State with the ATLAS Detector. *Phys. Rev. Lett.* **132,** 131802. arXiv: `2312.07605 [hep-ex]` (2024).

130. Grazzini, M., Ilnicka, A., Spira, M. & Wiesemann, M. Modeling BSM effects on the Higgs transverse-momentum spectrum in an EFT approach. *Journal of High Energy Physics* **2017.** ISSN: 1029-8479. `http://dx.doi.org/10.1007/JHEP03(2017)115` (Mar. 2017).

131. Maltoni, F., Vryonidou, E. & Zhang, C. Higgs production in association with a top-antitop pair in the Standard Model Effective Field Theory at NLO in QCD. *JHEP* **10,** 123. arXiv: `1607.05330 [hep-ph]` (2016).

132. Grazzini, M., Ilnicka, A. & Spira, M. Higgs boson production at large transverse momentum within the SMEFT: analytical results. *The European Physical Journal C* **78.** ISSN: 1434-6052. `http://dx.doi.org/10.1140/epjc/s10052-018-6261-7` (Oct. 2018).

133. Anastasiou, C. *et al. High precision determination of the gluon fusion Higgs boson cross-section at the LHC* 2016. arXiv: `1602.00695 [hep-ph]`.

134. Ellis, R. Keith and Hinchliffe, I. and Soldate, M. and van der Bij, J. J. Higgs Decay to $\tau^+ \tau^-$: A Possible Signature of Intermediate Mass Higgs Bosons at high energy hadron colliders. *Nucl. Phys. B* **297,** 221–243 (1988).

135. Baur, U. & Glover, E. W. N. Higgs Boson Production at Large Transverse Momentum in Hadronic Collisions. *Nucl. Phys. B* **339,** 38–66 (1990).

136. Del Duca, V., Kilgore, W., Oleari, C., Schmidt, C. & Zeppenfeld, D. Production of a Higgs Boson Accompanied by Two Jets Via Gluon Fusion. *Physical Review Letters* **87.** ISSN: 1079-7114. `http://dx.doi.org/10.1103/PhysRevLett.87.122001` (Aug. 2001).

137. Del Duca, V., Kilgore, W., Oleari, C., Schmidt, C. & Zeppenfeld, D. Gluon-fusion contributions to H+2 jet production. *Nuclear Physics B* **616,** 367–399. ISSN: 0550-3213. `http://dx.doi.org/10.1016/S0550-3213(01)00446-1` (Nov. 2001).

138. Campanario, F. & Kubocz, M. Higgs-boson production in association with three jets via gluon fusion at the LHC: Gluonic contributions. *Physical Review D* **88.** ISSN: 1550-2368. `http://dx.doi.org/10.1103/PhysRevD.88.054021` (Sept. 2013).

139. Greiner, N., Höche, S., Luisoni, G., Schönherr, M. & Winter, J.-C. Full mass dependence in Higgs boson production in association with jets at the LHC and FCC. *Journal of High Energy Physics* **2017.** ISSN: 1029-8479. `http://dx.doi.org/10.1007/JHEP01(2017)091` (Jan. 2017).

140. Boughezal, R., Caola, F., Melnikov, K., Petriello, F. & Schulze, M. Higgs boson production in association with a jet at next-to-next-to-leading order in perturbative QCD. *Journal of High Energy Physics* **2013.** ISSN: 1029-8479. `http://dx.doi.org/10.1007/JHEP06(2013)072` (June 2013).

141. Chen, X., Gehrmann, T., Glover, E. & Jaquier, M. Precise QCD predictions for the production of Higgs + jet final states. *Physics Letters B* **740,** 147–150. ISSN: 0370-2693. `http://dx.doi.org/10.1016/j.physletb.2014.11.021` (Jan. 2015).

142. Boughezal, R., Caola, F., Melnikov, K., Petriello, F. & Schulze, M. Higgs Boson Production in Association with a Jet at Next-to-Next-to-Leading Order. *Physical Review Letters* **115.** ISSN: 1079-7114. `http://dx.doi.org/10.1103/PhysRevLett.115.082003` (Aug. 2015).

143. Boughezal, R., Focke, C., Giele, W., Liu, X. & Petriello, F. *Higgs boson production in association with a jet at NNLO using jettiness subtraction* 2015. arXiv: `1505.03893 [hep-ph]`.

144. Harlander, R. V., Neumann, T., Ozeren, K. J. & Wiesemann, M. Top-mass effects in differential Higgs production through gluon fusion at $O\left(\alpha_s^4\right)$. *Journal of High Energy Physics* **2012.** ISSN: 1029-8479. `http://dx.doi.org/10.1007/JHEP08(2012)139` (Aug. 2012).

145. Neumann, T. & Wiesemann, M. Finite top-mass effects in gluon-induced Higgs production with a jet-veto at NNLO. *Journal of High Energy Physics* **2014.** ISSN: 1029-8479. `http://dx.doi.org/10.1007/JHEP11(2014)150` (Nov. 2014).

146. Jones, S. P., Kerner, M. & Luisoni, G. Next-to-Leading-Order QCD Corrections to Higgs Boson Plus Jet Production with Full Top-Quark Mass Dependence. *Physical Review Letters* **120.** ISSN: 1079-7114. `http://dx.doi.org/10.1103/PhysRevLett.120.162001` (Apr. 2018).

147. Bonciani, R. *et al.* Two-loop planar master integrals for Higgs $\to$ 3 partons with full heavy-quark mass dependence. *Journal of High Energy Physics* **2016.** ISSN: 1029-8479. `http://dx.doi.org/10.1007/JHEP12(2016)096` (Dec. 2016).

148. Becchetti, M., Bonciani, R., Casconi, V., Del Duca, V. & Moriello, F. Planar master integrals for the two-loop light-fermion electroweak corrections to Higgs plus jet production. *Journal of High Energy Physics* **2018.** ISSN: 1029-8479. `http://dx.doi.org/10.1007/JHEP12(2018)019` (Dec. 2018).

149. Bonciani, R. *et al.* Evaluating a family of two-loop non-planar master integrals for Higgs + jet production with full heavy-quark mass dependence. *Journal of High Energy Physics* **2020.** ISSN: 1029-8479. `http://dx.doi.org/10.1007/JHEP01(2020)132` (Jan. 2020).

150. Frellesvig, H., Hidding, M., Maestri, L., Moriello, F. & Salvatori, G. The complete set of two-loop master integrals for Higgs + jet production in QCD. *JHEP* **06,** 093. arXiv: `1911.06308 [hep-ph]` (2020).

151. Bonciani, R. *et al.* Next-to-leading-order QCD corrections to Higgs production in association with a jet. *Phys. Lett. B* **843,** 137995. arXiv: `2206.10490 [hep-ph]` (2023).

152. Davies, J., Schönwald, K., Steinhauser, M. & Zhang, H. Next-to-leading order electroweak corrections to $gg \to HH$ and $gg \to gH$ in the large-m_t limit. *JHEP* **10,** 033. arXiv: `2308.01355 [hep-ph]` (2023).

153. Bonetti, M., Panzer, E., Smirnov, V. A. & Tancredi, L. Two-loop mixed QCD-EW corrections to $gg \to Hg$. *JHEP* **11,** 045. arXiv: `2007.09813 [hep-ph]` (2020).

154. Becchetti, M., Moriello, F. & Schweitzer, A. Two-loop amplitude for mixed QCD-EW corrections to $gg \to Hg$. *JHEP* **04,** 139. arXiv: `2112.07578 [hep-ph]` (2022).

155. Bonetti, M., Panzer, E. & Tancredi, L. Two-loop mixed QCD-EW corrections to $q\overline{q} \to Hg, qg \to Hq$, and $\overline{q}g \to H\overline{q}$. *JHEP* **06,** 115. arXiv: `2203.17202 [hep-ph]` (2022).

156. Frixione, S., Kunszt, Z. & Signer, A. Three-jet cross sections to next-to-leading order. *Nuclear Physics B* **467,** 399–442. ISSN: 0550-3213. `http://dx.doi.org/10.1016/0550-3213(96)00110-1` (May 1996).

157. Buchalla, G., Capozi, M., Celis, A., Heinrich, G. & Scyboz, L. Higgs boson pair production in non-linear Effective Field Theory with full mt-dependence at NLO QCD. *Journal of High Energy Physics* **2018.** ISSN: 1029-8479. `http://dx.doi.org/10.1007/JHEP09(2018)057` (Sept. 2018).

158. Boggia, M. *et al. The HiggsTools Handbook: Concepts and observables for deciphering the Nature of the Higgs Sector* 2017. arXiv: `1711.09875 [hep-ph]`.

159. Gehrmann, T., Jaquier, M., Glover, E. W. N. & Koukoutsakis, A. Two-loop QCD corrections to the helicity amplitudes for H→3 partons. *Journal of High Energy Physics* **2012.** ISSN: 1029-8479. `http://dx.doi.org/10.1007/JHEP02(2012)056` (Feb. 2012).

160. A combination of measurements of Higgs boson production and decay using up to 139 fb^{-1} of proton–proton collision data at $\sqrt{s} = 13$ TeV collected with the ATLAS experiment (Aug. 2020).

161. Combined Higgs boson production and decay measurements with up to 137 fb^{-1} of proton-proton collision data at $\sqrt{s} = 13$ TeV (2020).

162. Celada, E. *et al. Mapping the SMEFT at High-Energy Colliders: from LEP and the (HL-)LHC to the FCC-ee* 2024. arXiv: `2404.12809 [hep-ph]`. `https://arxiv.org/abs/2404.12809`.

163. Butterworth, J. *et al.* PDF4LHC recommendations for LHC Run II. arXiv: `1510.03865 [hep-ph]` (2015).

164. Dulat, S. *et al.* New parton distribution functions from a global analysis of quantum chromodynamics. *Phys. Rev.* **D93,** 033006. arXiv: `1506.07443 [hep-ph]` (2016).

165. Harland-Lang, L. A., Martin, A. D., Motylinski, P. & Thorne, R. S. Parton distributions in the LHC era: MMHT 2014 PDFs. *Eur. Phys. J.* **C75,** 204. arXiv: `1412.3989 [hep-ph]` (2015).

166. Ball, R. D. *et al.* Parton distributions for the LHC Run II. *JHEP* **04,** 040. arXiv: `1410.8849 [hep-ph]` (2015).

167. Buckley, A. *et al.* LHAPDF6: parton density access in the LHC precision era. *The European Physical Journal C* **75.** ISSN: 1434-6052. `http://dx.doi.org/10.1140/epjc/s10052-015-3318-8` (Mar. 2015).
168. Andersen, J. R. *et al.* Les Houches 2013: Physics at TeV Colliders: Standard Model Working Group Report. arXiv: `1405.1067 [hep-ph]` (May 2014).
169. Aveleira, B. C., Heinrich, G., Kerner, M. & Kunz, L. Probing anomalous Higgs boson couplings in Higgs plus jet production at NLO QCD with full m_t-dependence. arXiv: `2409.05728 [hep-ph]`. `https://arxiv.org/abs/2409.05728` (2024).

A. Appendix

A.1. Fits with different rapidity cuts

As described in section 5.4.4, multiple ways of cutting the rapidity ($|y|_{\mathrm{max}}$, y^*, y_b) were studied and only one of them (version six) was used for the nominal fit. The results of two other variants, versions five and seven, are shown here.

As this numbering scheme implies, four more variants exist. These, however, produce less beautiful results and are therefore not included in this thesis.

Data set	bin 0	bin 1	bin 2	bin 3	bin 4	bin 5
ATLAS 7 TeV (y^*)	< 1.0	< 1.5	< 1.5	< 2.0	< 2.0	< 2.5
CMS 7 TeV ($\|y\|_{\mathrm{max}}$)	< 1.0	< 1.5	< 1.5	< 2.0	< 2.0	< 2.5
ATLAS 13 TeV (y^*)	< 1.0	< 1.5	< 1.5	< 2.0	< 2.0	< 2.5
CMS 8 TeV (y^*, y_b)	$y^* < 1.0$ $y_b < 1.0$	$y^* < 1.0$ $y_b < 1.0$	$y^* < 2.0$ $y_b < 1.0$	$y^* < 2.0$ $y_b < 1.0$	$y^* < 2.0$ $y_b < 1.0$	$y^* < 2.0$ $y_b < 1.0$
CMS 13 TeV 2D ($\|y\|_{\mathrm{max}}$)	< 1.0	< 1.5	< 1.5	< 2.0	< 2.0	< 2.5
CMS 13 TeV 3D (y^*, y_b)	$y^* < 1.0$ $y_b < 1.0$	$y^* < 1.5$ $y_b < 1.0$	$y^* < 1.5$ $y_b < 1.0$	$y^* < 2.0$ $y_b < 1.0$	$y^* < 2.0$ $y_b < 1.5$	$y^* < 2.5$ $y_b < 1.5$

Table A.1.: Table describing the meaning of bins for rapidity cut version five. Differences to version six used in section 5.4.4 are marked in orange.

Data set	bin 0	bin 1	bin 2	bin 3	bin 4	bin 5
ATLAS 7 TeV (y^*)	< 1.0	< 1.5	< 1.5	< 2.0	< 2.5	< 3.0
CMS 7 TeV ($\|y\|_{\mathrm{max}}$)	< 1.0	< 1.5	< 1.5	< 2.0	< 2.5	< 2.5
ATLAS 13 TeV (y^*)	< 1.0	< 1.5	< 1.5	< 2.0	< 2.5	< 3.0
CMS 8 TeV (y^*, y_b)	$y^* < 1.0$ $y_b < 1.0$	$y^* < 1.0$ $y_b < 1.0$	$y^* < 2.0$ $y_b < 1.0$	$y^* < 2.0$ $y_b < 2.0$	$y^* < 2.0$ $y_b < 2.0$	$y^* < 3.0$ $y_b < 2.0$
CMS 13 TeV 2D ($\|y\|_{\mathrm{max}}$)	< 1.0	< 1.5	< 1.5	< 2.0	< 2.5	< 3.0
CMS 13 TeV 3D (y^*, y_b)	$y^* < 1.0$ $y_b < 1.0$	$y^* < 1.5$ $y_b < 1.0$	$y^* < 1.5$ $y_b < 1.0$	$y^* < 2.0$ $y_b < 2.0$	$y^* < 2.5$ $y_b < 2.0$	$y^* < 2.5$ $y_b < 2.0$

Table A.2.: Table describing the meaning of bins for rapidity cut version seven. Differences to version six used in section 5.4.4 are marked in orange.

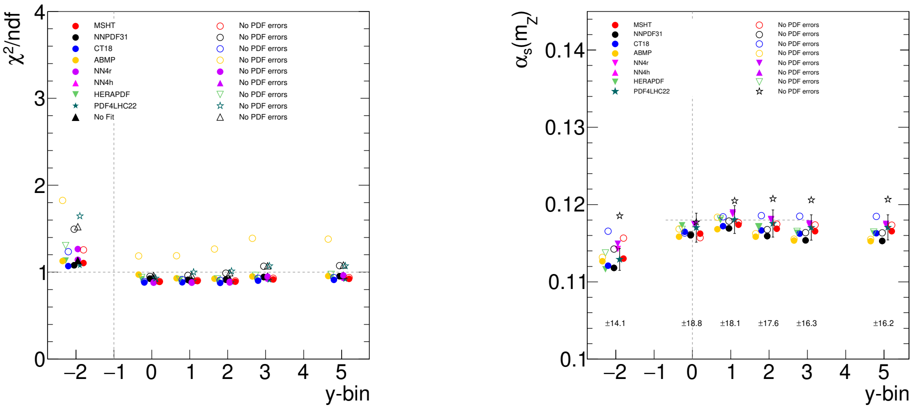

(a) χ^2 per degree of freedom for just the old four data sets.

(b) α_s central values and error margins from fits to only the old four data sets.

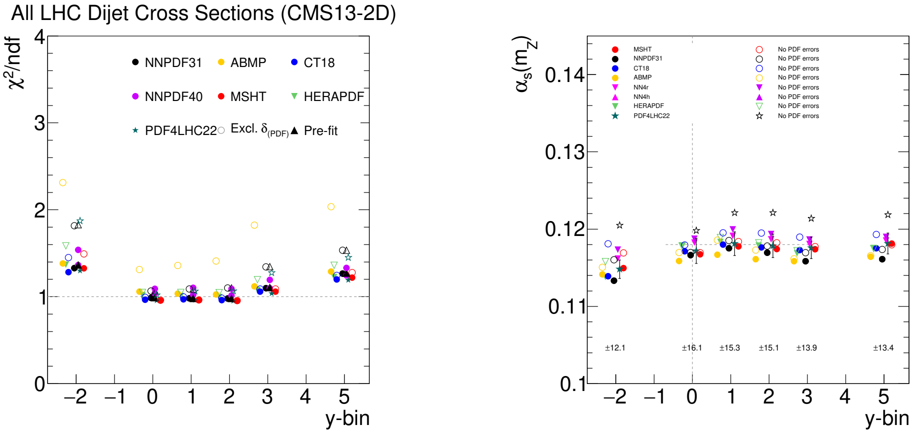

(c) χ^2 per degree of freedom including the CMS 13 TeV 2D data.

(d) α_s central values and error margins including the CMS 13 TeV 2D data.

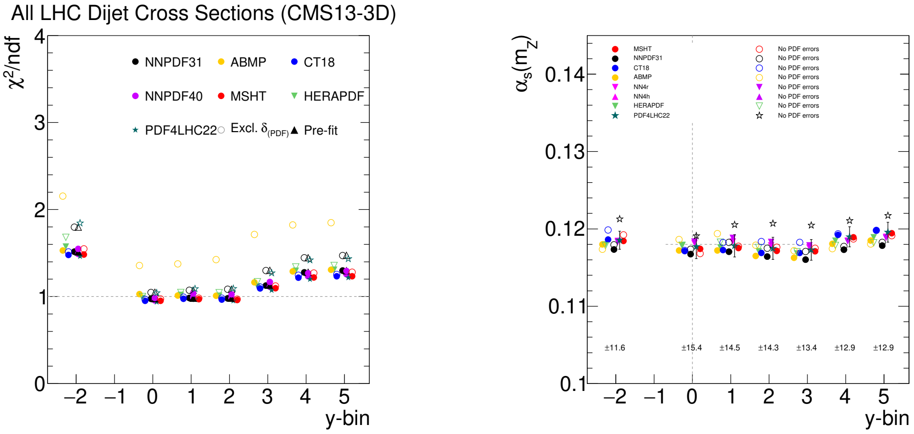

(e) χ^2 per degree of freedom including the CMS 13 TeV 3D data.

(f) α_s central values and error margins including the CMS 13 TeV 3D data.

Figure A.1.: Fits for rapidity cut version five. The result on the very left in each plot corresponds to the case without any cuts applied, including all rapidity values. The definition of the bins is given in table A.1. The plots were made by Daniel Britzger (MPI Munich) for the `APPLfast` collaboration.

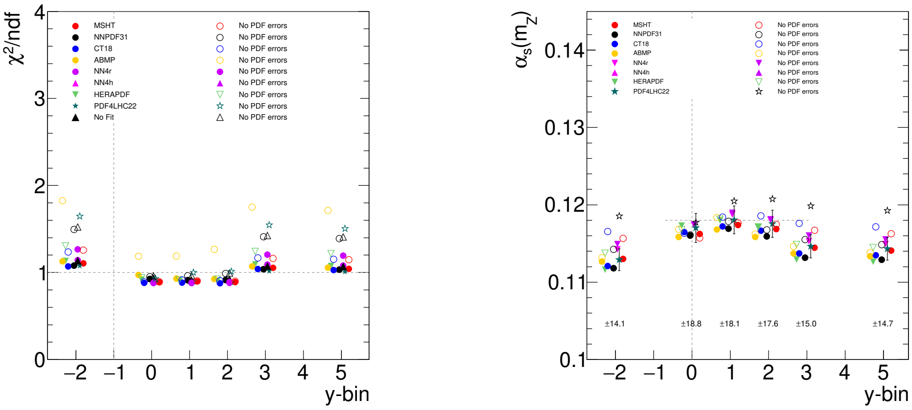

(a) χ^2 per degree of freedom for just the old four data sets.

(b) α_s central values and error margins from fits to only the old four data sets.

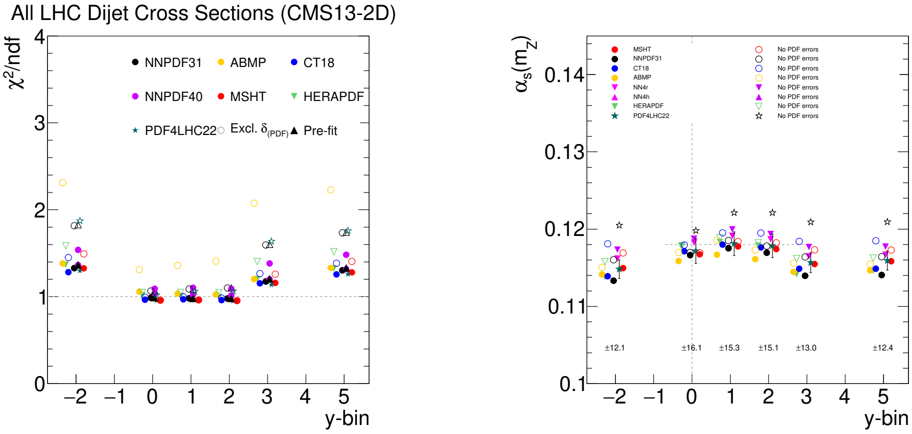

(c) χ^2 per degree of freedom including the CMS 13 TeV 2D data.

(d) α_s central values and error margins including the CMS 13 TeV 2D data.

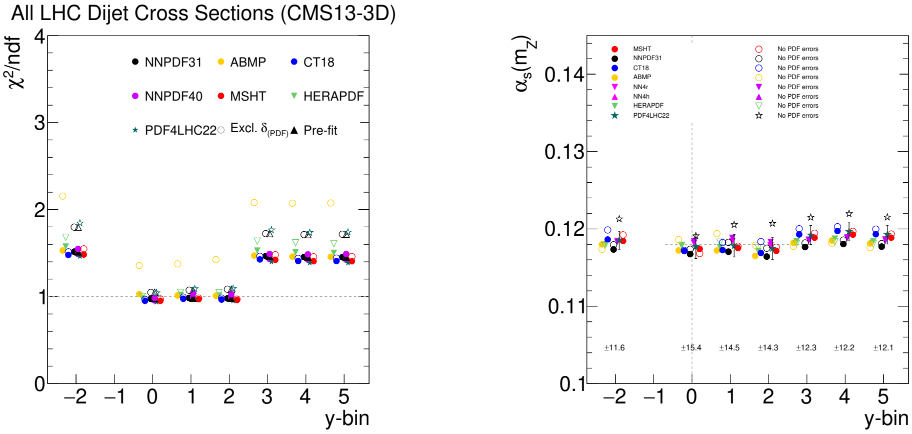

(e) χ^2 per degree of freedom including the CMS 13 TeV 3D data.

(f) α_s central values and error margins including the CMS 13 TeV 3D data.

Figure A.2.: Fits for rapidity cut version seven. The result on the very left in each plot corresponds to the case without any cuts applied, including all rapidity values. The definition of the bins is given in table A.2. The plots were made by Daniel Britzger (MPI Munich) for the `APPLfast` collaboration.

Acknowledgements / Danksagung

Zunächst möchte ich **Gudrun Heinrich** danken, die mir diese Promotion ermöglicht hat. Ganz banal zunächst durch das Angebot einer Anstellung, viel mehr aber noch durch ihre Betreuung, sowohl während der wöchentlichen Meetings als auch darüber hinaus mit immerwährender Erreichbarkeit und schnellen Antworten auf alle Fragen, die mir begegneten. Nicht nur in meinem Forschungsprojekt an sich, sondern auch im Bezug auf Reisen zu Workshops, Konferenzen und Summer Schools konnte ich immer auf Unterstützung zählen, was mir diese letzten drei Jahre sehr angenehm gestaltet hat.

Ebenso gilt mein Dank natürlich auch **Klaus Rabbertz**, der zu dieser Promotion weit mehr beigetragen hat als Zweitbetreuer es in den meisten Fällen tun. Seine Hilfe und Expertise haben meine Arbeit wesentlich erleichtert und dadurch maßgeblich zu ihrem Erfolg geführt. Trotz der Entfernung zwischen Genf und Karlsruhe konnte ich mich immer auf engmaschigen Austausch verlassen.

Selbiges gilt natürlich auch für die weiteren Personen, mit denen ich zusammengearbeitet habe, in besonderem Maße **Daniel Britzger** und **Matthias Kerner**, ohne deren Einsatz ich vielmals an technischen Details verzweifelt oder gar gescheitert wäre.
Auch **Xuan Chen** ist hier zu nennen, für seine insbesondere in der Anfangsphase äußerst wertvollen Beiträge und Anregungen. In der Endphase trifft selbiges auf **Benjamin Campillo** zu, welchem ich hier ebenso meinen herzlichen Dank aussprechen möchte.
Zu guter Letzt, was die Forschung an sich betrifft, möchte ich **Alexander Huss** und **João Pires** danken, deren Beiträge immer sehr hilfreich und wertvoll waren.

Darüber hinaus gilt mein Dank natürlich all jenen, die meinen Alltag am Institut (bzw. den Instituten) durch den sowohl fachlichen als auch außerfachlichen Austausch so interessant, abwechslungsreich und lebenswert gemacht haben. Am ITP gilt dies in besonderem Maße für meine Büro-Kollegen **Sauro Carlotti**, **Stefan Kiebacher** und **Anton Olsson** sowie für **Jannis Lang**, der durch sein ähnliches Forschungsthema ein äußerst hilfreicher Ansprechpartner war. Auf Seiten des ETP sind **Nils Faltermann**, **Alexander Heidelbach** und **Robin Hofsaess** hervorzuheben, die mich mit ihrem technischen Sachverstand und Ratschlägen zur Nutzung von Computing-Ressourcen äußerst bereichern konnten.

Auch der Graduiertenschule KSETA und ihren Verantwortlichen **Katrin Link**, **Raquel Lujan Miravet** und **Ulrich Nierste** bin ich sehr dankbar für die gemeinsame Arbeit in meiner Rolle als Doktorandenvertreter. Gleiches gilt für meine Kollegen aus dem Doktorandenkonvent der Physik und dem Promovierendenbeirat des KIT, dem KIT-Konvent, dem KIT-Senat sowie dem Fakultätsrat Physik, mit denen ich die Welt der Hochschulpolitik erkunden durfte.

Herzlicher Dank ergeht an dieser Stelle auch an all meine Freunde, die mich auf dem Weg bis zur Promotion begleitet haben. So erfüllend die Physik auch ist, ohne euch wäre diese Reise nicht einmal halb so schön gewesen. Dazu zähle ich auch die Fachschaft Physik, in welcher ich eine nicht unerhebliche Zeit meines Studiums verbracht habe und bei deren Veranstaltungen und insbesondere O-Phasen ich immer gerne beteiligt war.

Ganz besonders möchte ich schließlich meinen Eltern danken, ohne deren immerwährende Unterstützung und Hilfsbereitschaft nicht nur diese Promotion, sondern mein ganzes Studium sicher nicht so gut, so angenehm, so unbeschwert und so erfolgreich funktioniert hätte wie ich das Glück hatte es erleben zu dürfen.

Zu guter Letzt möchte ich dem allerwichtigsten Menschen in meinem Leben ein riesiges Dankeschön aussprechen: Die Ruhe und Ausgeglichenheit, die du in mir auslöst, die Energie und Kraft, die du mir gibst, das Glück und die Freude, die du wieder und wieder in mein Leben bringst, sind für mich unvergleichbar wertvoll und unverzichtbar geworden. Amelie, ich liebe dich!